

AD-A268 352

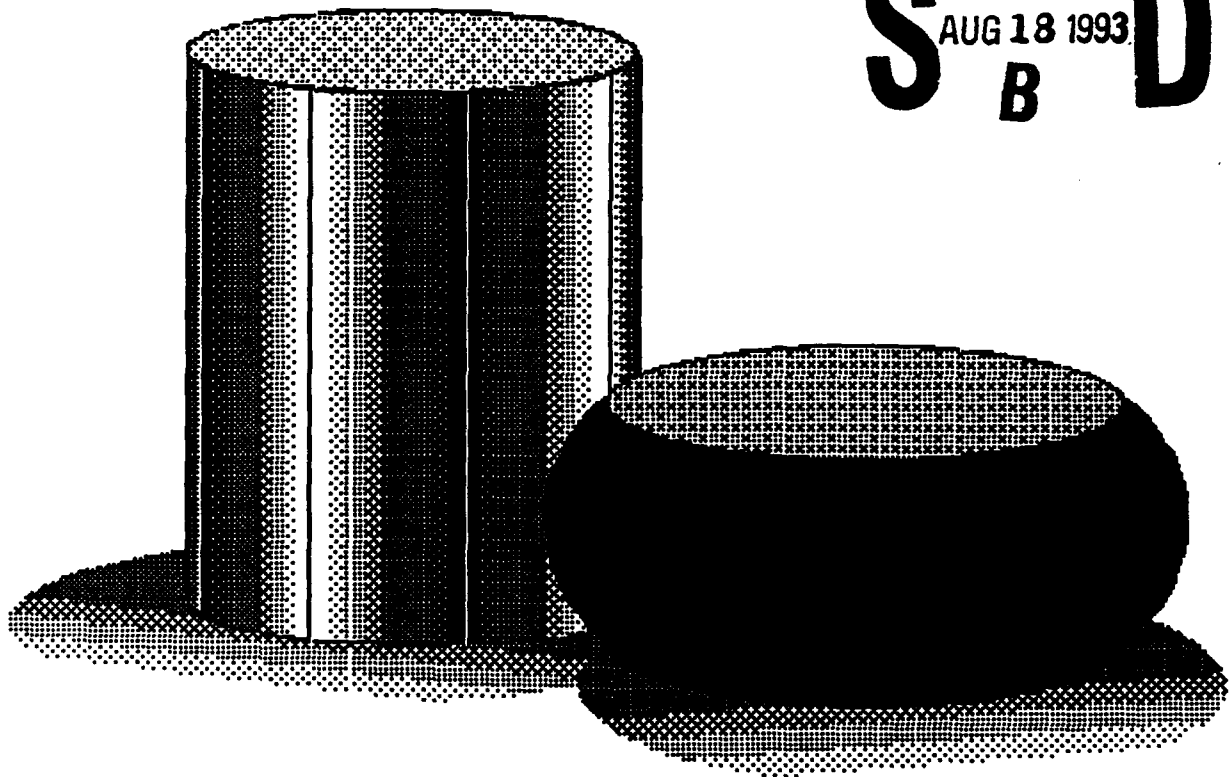


8000185



Atlas of Formability

Ultimet



DTIC
ELECTE
AUG 18 1993
S B D

DISTRIBUTION STATEMENT A
Approved for public release
Distribution Unlimited

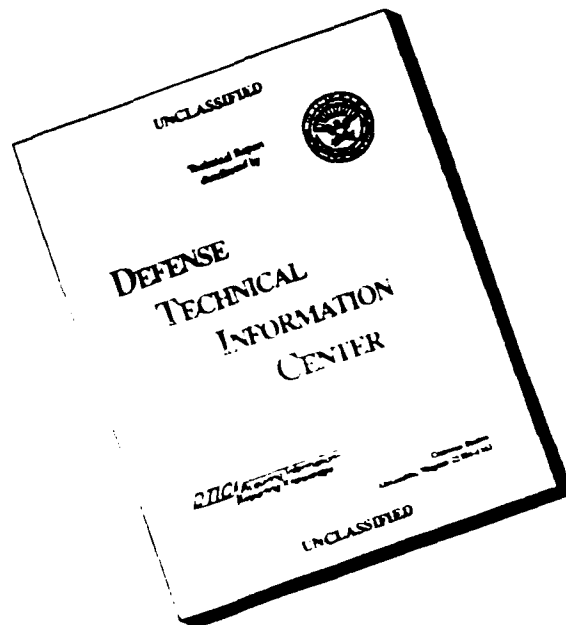
93-18984



NCEM

93 16 053

DISCLAIMER NOTICE



THIS DOCUMENT IS BEST
QUALITY AVAILABLE. THE COPY
FURNISHED TO DTIC CONTAINED
A SIGNIFICANT NUMBER OF
PAGES WHICH DO NOT
REPRODUCE LEGIBLY.

REPORT DOCUMENTATION PAGE			Form Approved OMB No. 0704-0188	
Public reporting burden for this collection of information is estimated to average 1 hour per response, including the time for reviewing instructions, searching existing data sources, gathering and maintaining the data needed, and completing and reviewing the collection of information. Send comments regarding this burden estimate or any other aspect of this collection of information, including suggestions for reducing this burden, to Washington Headquarters Services, Directorate for Information Operations and Reports, 1215 Jefferson Davis Highway, Suite 1204, Arlington, VA 22202-4302 and to the Office of Management and Budget, Paperwork Reduction Project (0704-0188), Washington, DC 20503				
1. AGENCY USE ONLY (Leave blank)	2. REPORT DATE March 24, 1993	3. REPORT TYPE AND DATES COVERED Final, Dec. 28, 1992 - Mar. 24, 1993		
4. TITLE AND SUBTITLE ATLAS OF FORMABILITY Ultimet Alloy		5. FUNDING NUMBERS C-N00140-88-C-RC21		
6. AUTHOR(S)				
7. PERFORMING ORGANIZATION NAME(S) AND ADDRESS(ES) National Center for Excellence in Metalworking Technology (NCEMT) 1450 Scalp Avenue Johnstown, PA 15904		8. PERFORMING ORGANIZATION REPORT NUMBER		
9. SPONSORING / MONITORING AGENCY NAME(S) AND ADDRESS(ES) Naval Industrial Resources Support Activity Building 75-2, Naval Base Philadelphia, PA 19112-5078		10. SPONSORING / MONITORING AGENCY REPORT NUMBER		
11. SUPPLEMENTARY NOTES				
12a. DISTRIBUTION / AVAILABILITY STATEMENT			12b. DISTRIBUTION CODE	
13. ABSTRACT (Maximum 200 words) In this investigation, flow behavior of Ultimet alloy was studied by conducting compression tests over a wide range of temperatures (950-1200 C) and strain rates (0.001-20 s ⁻¹). The true stress-true strain flow curves are presented for each test condition. Constitutive relations were determined from the flow behavior, and a dynamic material modeling was performed on this material. Thus, the optimum processing condition in terms of temperature and strain rate was identified as 1012 C and 0.001 s ⁻¹ for this alloy. Workability of the material as a function of strain rate and temperature was also determined. Microstructural changes during high temperature deformation were characterized, and selective micrographs are presented together with corresponding flow curves. Dynamic recrystallization and grain growth occurred during high temperature deformation in some test conditions. This report supplies ample mechanical and microstructural data on Ultimet alloy for engineers in the field of metalworking process design.				
14. SUBJECT TERMS Ultimet Alloy, Deformation Processing, High Temperature Deformation, Processing Map, Metalworking, Deformed Microstructure			15. NUMBER OF PAGES 64	
			16. PRICE CODE	
17. SECURITY CLASSIFICATION OF REPORT Unclassified	18. SECURITY CLASSIFICATION OF THIS PAGE Unclassified	19. SECURITY CLASSIFICATION OF ABSTRACT Unclassified	20. LIMITATION OF ABSTRACT	

**ATLAS OF FORMABILITY
ULTIMET**

by

**National Center for Excellence in Metalworking Technology
1450 Scalp Avenue
Johnstown, PA 15904**

for

**Naval Industrial Resource Support Activity
Building 75-2, Naval Base
Philadelphia, PA 19112-5078**

March 24, 1993

This work was conducted by the National Center for Excellence in Metalworking Technology (NCEMT), operated by Concurrent Technologies Corporation (CTC), under contract to the U.S. Navy as part of the U.S. Navy Manufacturing Technology Program.

The views, opinions, and/or findings contained in this report should not be construed as an official Department of the Navy position, policy, or decision, unless so designated by other documentation.

ATLAS OF FORMABILITY

Process design and modeling engineers typically rely on materials suppliers to provide the data needed to successfully design metalforming processes. However, this information is often not sufficient or appropriate for increasingly sophisticated industrial processes and applications. In some cases, there is a total lack of mechanical and microstructural data at forming temperatures and speeds. Without proper data, engineers rely on trial-and-error methods of process development and optimization.

The National center for Excellence in Metalworking Technology (NCEMT) has begun developing an Atlas of Formability to address this problem. The objective of the Atlas is to provide the mechanical and microstructural data required to develop accurate and realistic metalforming simulations. These simulations can reduce or eliminate the need for trial-and-error approaches, thereby streamlining process development and optimization. To achieve its objective, the NCEMT uses state-of-the-art materials testing and characterization methodologies to develop workability data for advanced alloy systems. This effort is sponsored by the U.S. Navy Manufacturing Technology Program, which selects materials for the Atlas based on priorities set by the Navy. The NCEMT publishes Atlas Bulletins on a continuing basis.

ULTIMET

ABSTRACT

In this bulletin, flow behavior of Ultimet alloy has been determined by conducting compression tests over a wide range of temperatures (950-1200 C) and strain rates (10^{-3} - 20 s^{-1}). The true stress-true strain flow curves are presented for each test condition. Constitutive relations were determined from the flow behavior, and dynamic material modeling was performed. Thus, the optimum processing condition in terms of temperature and strain rate was identified as 1012 C and 10^{-3} s^{-1} . Microstructural changes during high temperature deformation were also characterized, and selected micrographs are presented together with corresponding flow curves. Dynamic recrystallization and grain growth occurred during high temperature deformation over the range of temperatures tested. This report supplies ample mechanical and microstructural data on Ultimet alloy for engineers in the field of metalforming process design.

TABLE OF CONTENTS

Introduction	1
Experimental Procedure	1
Results	1
Summary	64
Implementation of Data Provided by the Atlas of Formability	64

LIST OF TABLES

Table 1. Chemical composition of Ultimet alloy	1
Table 2. List of figures, testing conditions and microstructural observations for Ultimet alloy	2

DTIC QUALITY INSPECTED **3**

ST #A, AUTH USNAVIRSA (MR PLONSKY 8/443-6684)
PER TELECON, 17 AUG 93 CB

Accession For		6
NTIS GRA&I		<input checked="" type="checkbox"/>
DTIC TAB		<input type="checkbox"/>
Unannounced		<input type="checkbox"/>
Justification		
By <i>per telecon</i>		
Distribution/		
Availability Codes		
Dist	Avail and/or Special	
<i>A-1</i>		

Ultimet

Introduction

Ultimet alloy possesses both the wear-resistant characteristics of cobalt-based Stellite alloys and the corrosion-resistant properties of nickel-based Hastelloy alloys. The alloy also has good forming and welding characteristics, but work hardening involves mechanical twinning. The understanding of mechanical and microstructural behavior during high temperature deformation is very important in forming this material. In this investigation, flow behavior of Ultimet alloy was studied by conducting compression tests over a wide range of temperatures and strain rates. Constitutive relations were determined from the flow behavior and subsequently, a dynamic material modeling for this alloy was performed. Thus, the optimum processing condition in terms of temperature and strain rate was determined. Microstructural changes during high temperature deformation were also characterized to help process design engineers select processing conditions for the desired microstructures.

Experimental Procedure

Commercially available Ultimet wrought bars in annealed condition were used in this investigation. The bars were approximately 19 mm in diameter. The typical microstructure of the as-received material is shown in Figure 1. The chemical composition of the alloy is shown in Table 1.

Table 1. Chemical composition of Ultimet alloy.

Element	Co	Ni	Fe	Cr	Mo	W	C	N	Si	Mn	B	S	P
Wt%	bal.	8.81	3.22	26.2	5.08	2.47	.07	.092	.37	.69	.002	<.002	<.005

Cylindrical compression test specimens with a diameter of 12.7 mm and a height of 15.9 mm were machined from the bars. Isothermal compression tests were conducted in vacuum on an MTS testing machine. The test matrix was as follows:

Temperature, C (F): 950 (1742), 1000 (1832), 1050 (1922), 1100 (2012), 1125 (2057), 1150 (2102), and 1200 (2192);

Strain rate, s^{-1} : 0.001, 0.01, 0.05, 0.1, 0.5, 1, 5 and 20.

Load and stroke data were acquired during the tests by a computer and later converted to true stress-true strain curves. Immediately after the compression test, the specimens were quenched with forced helium gas in order to retain the deformed microstructure. Longitudinal sections of the specimens were examined by optical microscopy. The photomicrographs presented are electronic images and were taken from the center of the longitudinal section of the specimens.

Results

Table 2 is a list of the figures, test conditions, and the observed microstructures. True stress-true strain flow curves with selected corresponding deformed microstructure are shown from Figure 2 to Figure 57. True stress vs. strain rate was plotted in log-log scale in Figure 58 at a true strain of 0.5. The slope of the plot gives the strain rate sensitivity m , which is not constant over the ranges of temperatures and strain rates tested. Log stress vs. $1/T$ at the same true strain is shown in Figure 59. A processing map at this strain was developed, Figure 60. The optimum processing condition is obtained by selecting the temperature and strain rate combination which provides the maximum efficiency in the stable region. This condition is 1012 C and $10^{-3} s^{-1}$ for this material.

Table 2. List of figures, testing conditions and microstructural observations for Ultimet alloy.

Figure No	Temperature C (F)	Strain Rate s ⁻¹	Microstructure Optical Microscopy	Page No
1	As received		Equiaxed grains with an average size of 51.6 μm , large cuboidal-like precipitates (ppt) and extensive twinning, some inclusions.	4
2	950 (1742)	0.001	60% dynamically recrystallized (DRX) grains with deformed (elongated) original grain boundaries still visible, necklacing at large original grain boundaries.	5
3	950 (1742)	0.01	Same as above, 50% DRX.	6
4	950 (1742)	0.05		7
5	950 (1742)	0.1	Same as above.	8
6	950 (1742)	0.5		9
7	950 (1742)	1	Same as above.	10
8	950 (1742)	5	Same as above.	11
9	950 (1742)	20	60% DRX, the new recrystallized grains have an average size of 5 μm , less elongation of the original grains.	12
10	1000 (1832)	0.001	95% DRX equiaxed grains with an average size of 10 μm , prior deformed grain boundaries are still visible, some ppt. and inclusions.	13
11	1000 (1832)	0.01		14
12	1000 (1832)	0.05	Same as above, but 90% DRX (prior deformed grains are well defined).	15
13	1000 (1832)	0.1		16
14	1000 (1832)	0.5	Same as above.	17
15	1000 (1832)	1	80% DRX grains with an average size of 8 μm , prior deformed grains are still visible.	18
16	1000 (1832)	5		19
17	1000 (1832)	20	Same as above, but ~95% DRX.	20
18	1050 (1922)	0.001	100% DRX equiaxed grains with an average size of 16 μm , some grain growth and twinning.	21
19	1050 (1922)	0.01	Same as above except smaller grains and some prior grain boundaries.	22
20	1050 (1922)	0.05		23
21	1050 (1922)	0.1	80% DRX equiaxed grains with an average size of 10 μm , deformed prior grain boundaries visible.	24
22	1050 (1922)	0.5		25
23	1050 (1922)	1	100% DRX equiaxed grains with an average size of 10 μm in size, some deformed prior grain boundaries visible.	26
24	1050 (1922)	5	Same as above, but with some twinning.	27
25	1050 (1922)	20	Same as above.	28
26	1100 (2012)	0.001	100% DRX equiaxed grains with an average size of 34 μm , extensive twinning.	29
27	1100 (2012)	0.01		30
28	1100 (2012)	0.05	Same as above, except that the average grain size is 25 μm .	31
29	1100 (2012)	0.1	Same as above, except that the average grain size is 21 μm .	32

30	1100 (2012)	0.5	Same as above, except that the average grain size is 20 μ m.	
31	1100 (2012)	1	Same as above, except slightly smaller grains.	34
32	1100 (2012)	5		35
33	1100 (2012)	20	Same as above, except that the average grain size is 17 μ m.	36
34	1125 (2057)	0.001	100% DRX equiaxed grains with an average grain size of 45 μ m, much twinning.	37
35	1125 (2057)	0.01	Same as above, except smaller grains.	38
36	1125 (2057)	0.05		39
37	1125 (2057)	0.1	Same as above, except even smaller grains.	40
38	1125 (2057)	0.5		41
39	1125 (2057)	1	Same as above.	42
40	1125 (2057)	5	Same as above.	43
41	1125 (2057)	20	Same as above, except that the grain size is ~25 μ m.	44
42	1150 (2102)	0.001	100% DRX equiaxed grains with an average grain size of 65 μ m, extensive twinning.	45
43	1150 (2102)	0.01		46
44	1150 (2102)	0.05	Same as above, except that the grains are smaller.	47
45	1150 (2102)	0.1		48
46	1150 (2102)	0.5	Same as above.	49
47	1150 (2102)	1	Same as above, but the average grain size is 40 μ m.	50
48	1150 (2102)	5		51
49	1150 (2102)	20	Same as above, except that the average grain size is 30 μ m.	52
50	1200 (2192)	0.001	100 % DRX with extensive grain growth, with an average size of 79 μ m, much twinning.	53
51	1200 (2192)	0.01	Same as above, except that the grains are smaller.	54
52	1200 (2192)	0.05		55
53	1200 (2192)	0.1	Same as above, except that the average grain size is 40 μ m.	56
54	1200 (2192)	0.5		57
55	1200 (2192)	1	Same as above, but smaller grain size.	58
56	1200 (2192)	5		59
57	1200 (2192)	20	Same as above, except that the grains are smaller with an average size of 35 μ m.	60

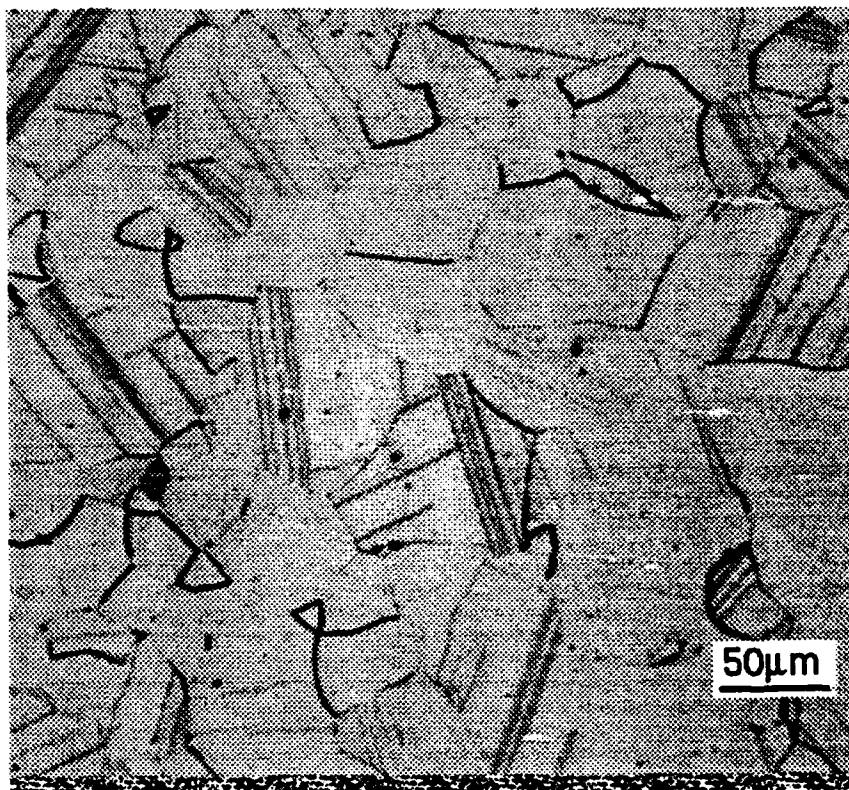


Figure 1. As-received microstructure of Ultimec.

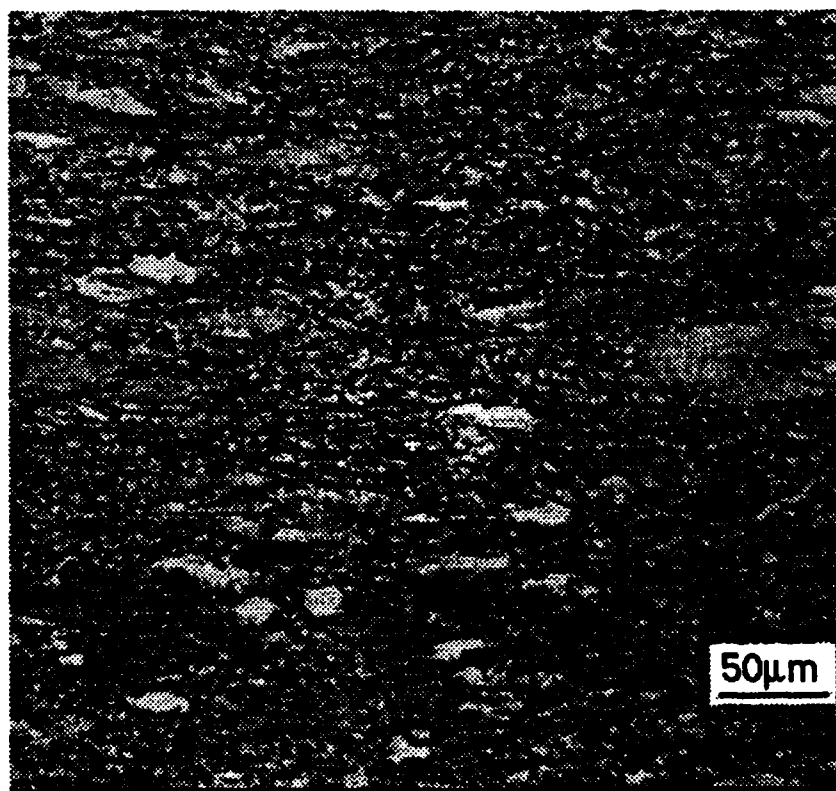
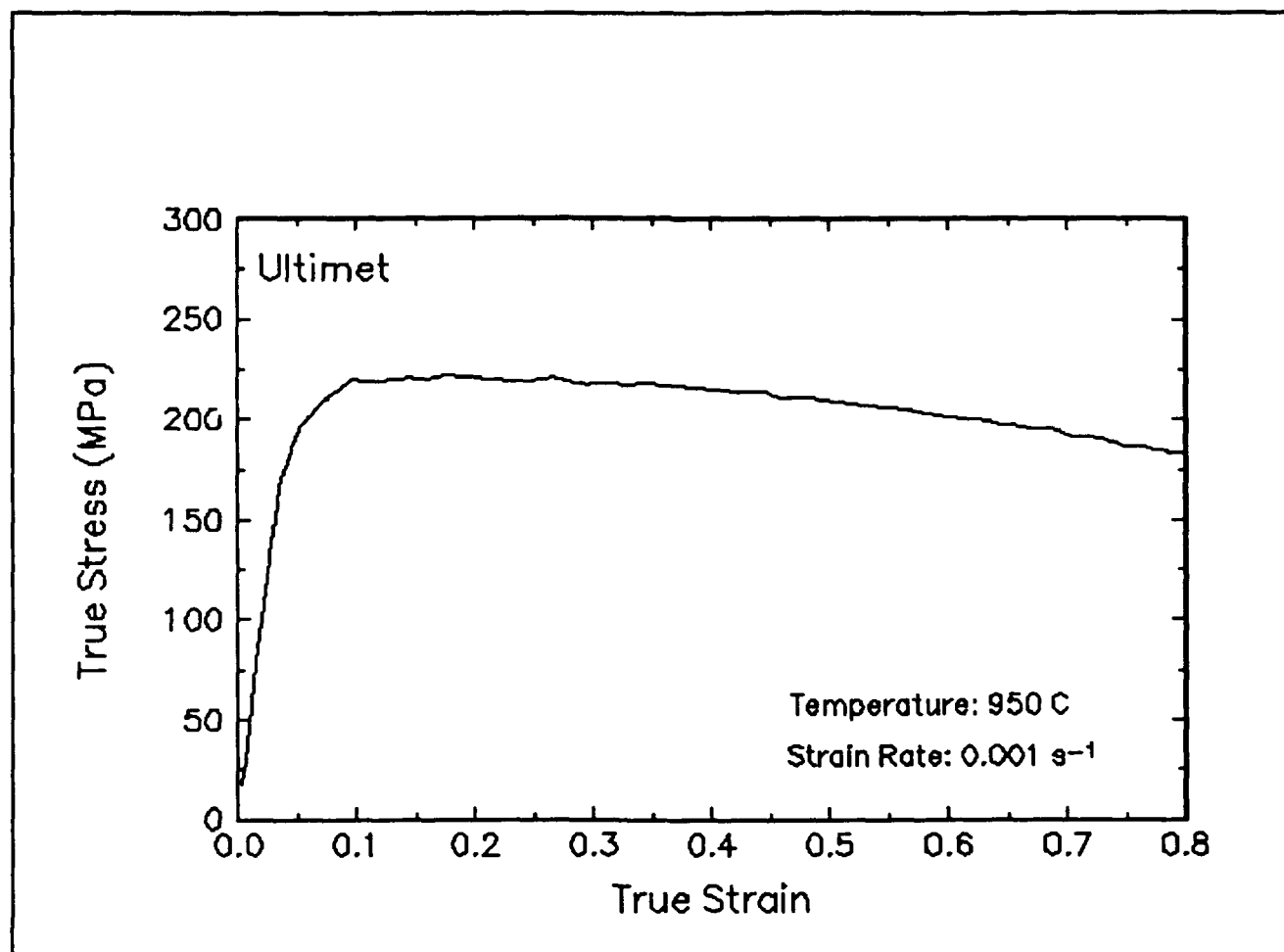


Figure 2. True stress-true strain curve and an optical micrograph from the center of the compressed sample cut through the compression axis, 950 C and 0.001 s⁻¹.

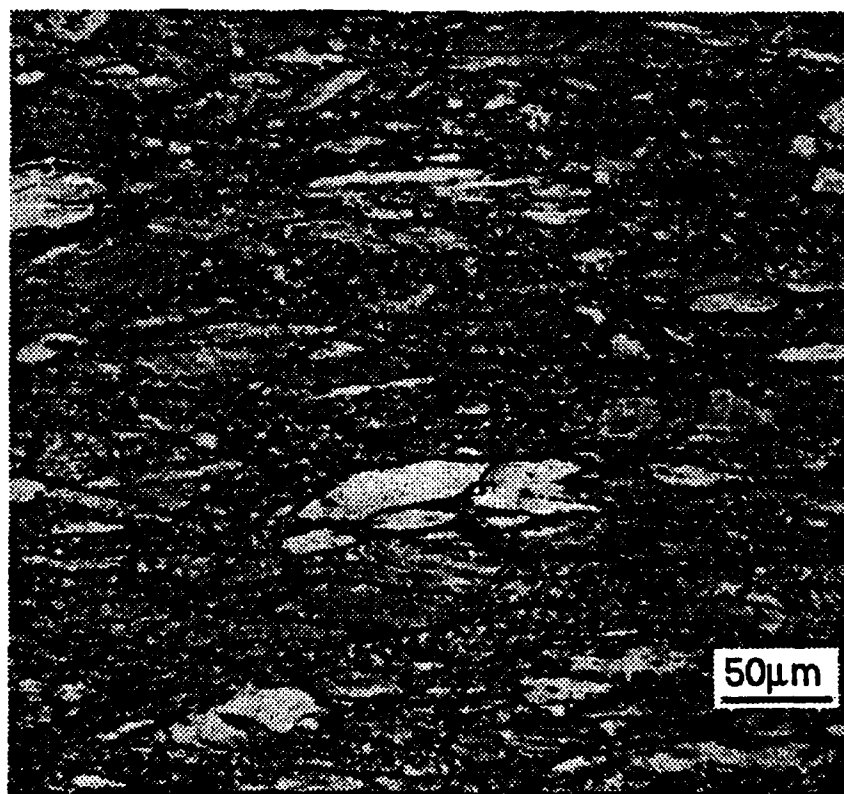
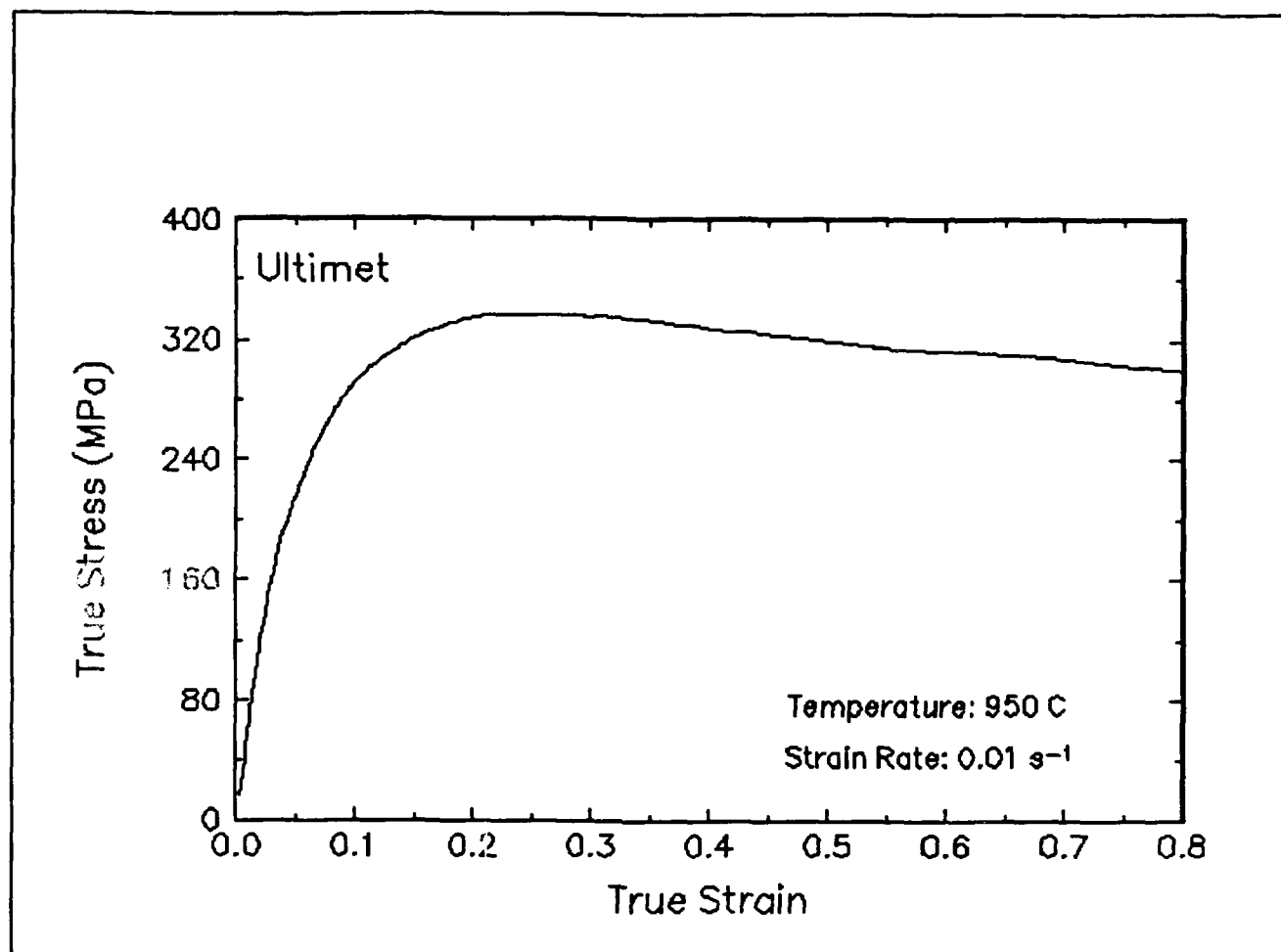


Figure 3. True stress-true strain curve and an optical micrograph from the center of the compressed sample cut through the compression axis, 950 C and 0.01 s⁻¹.

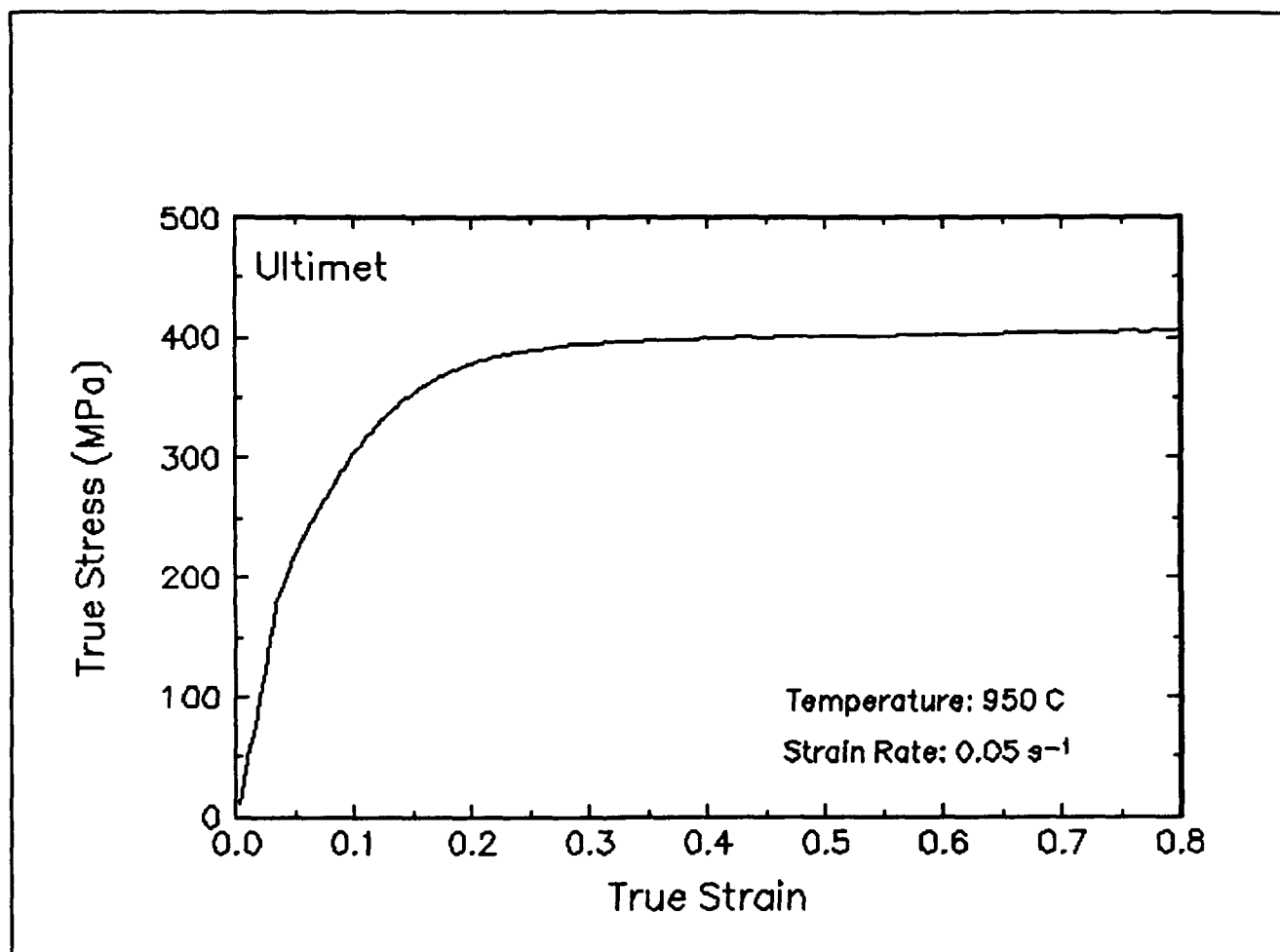


Figure 4. True stress-true strain curve, 950 C and 0.05 s⁻¹.

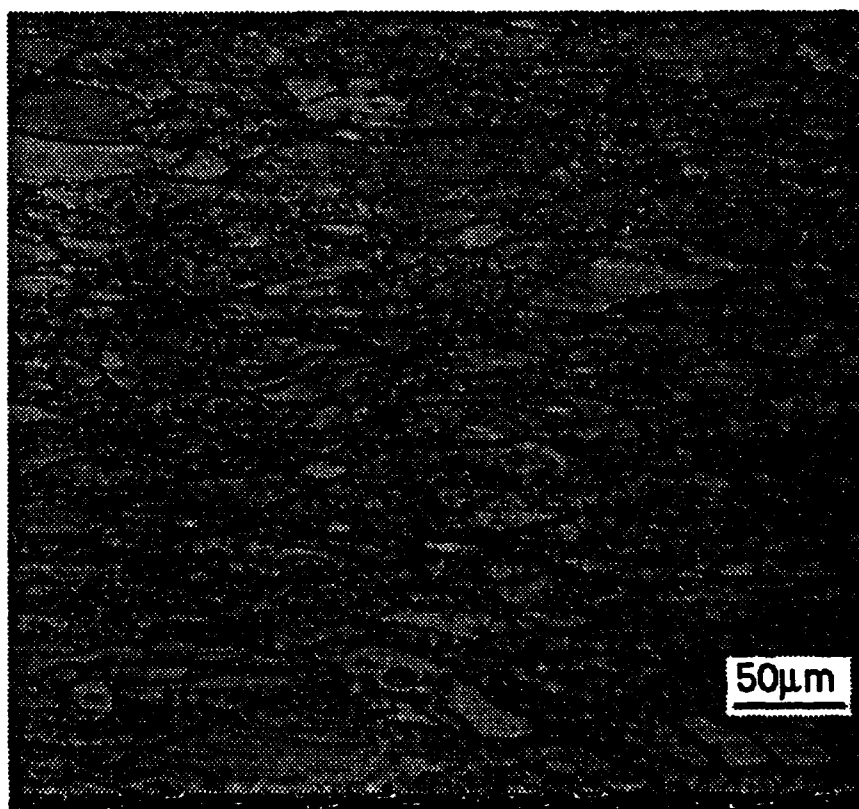
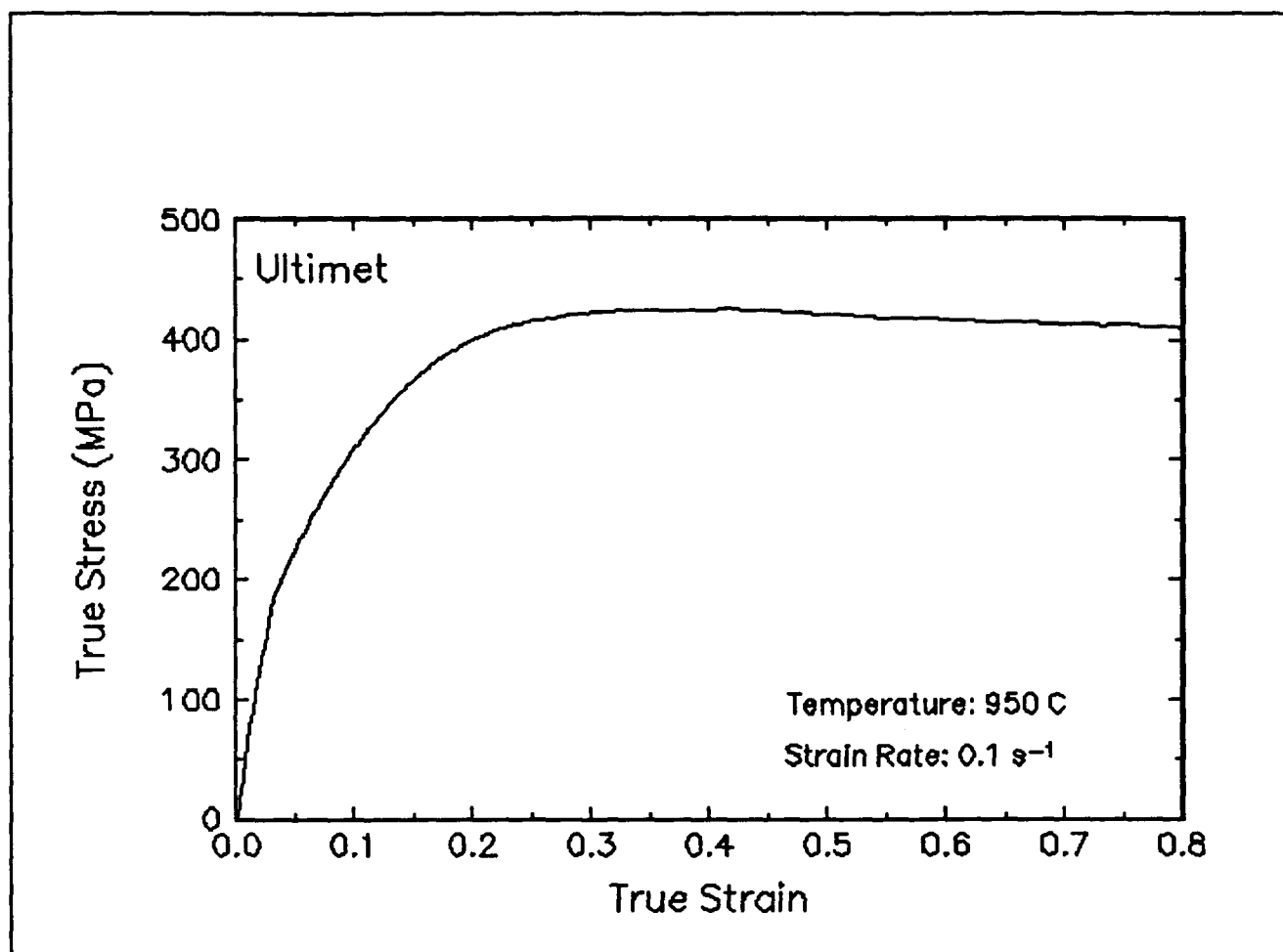


Figure 5. True stress-true strain curve and an optical micrograph from the center of the compressed sample cut through the compression axis, 950 C and 0.1 s⁻¹.

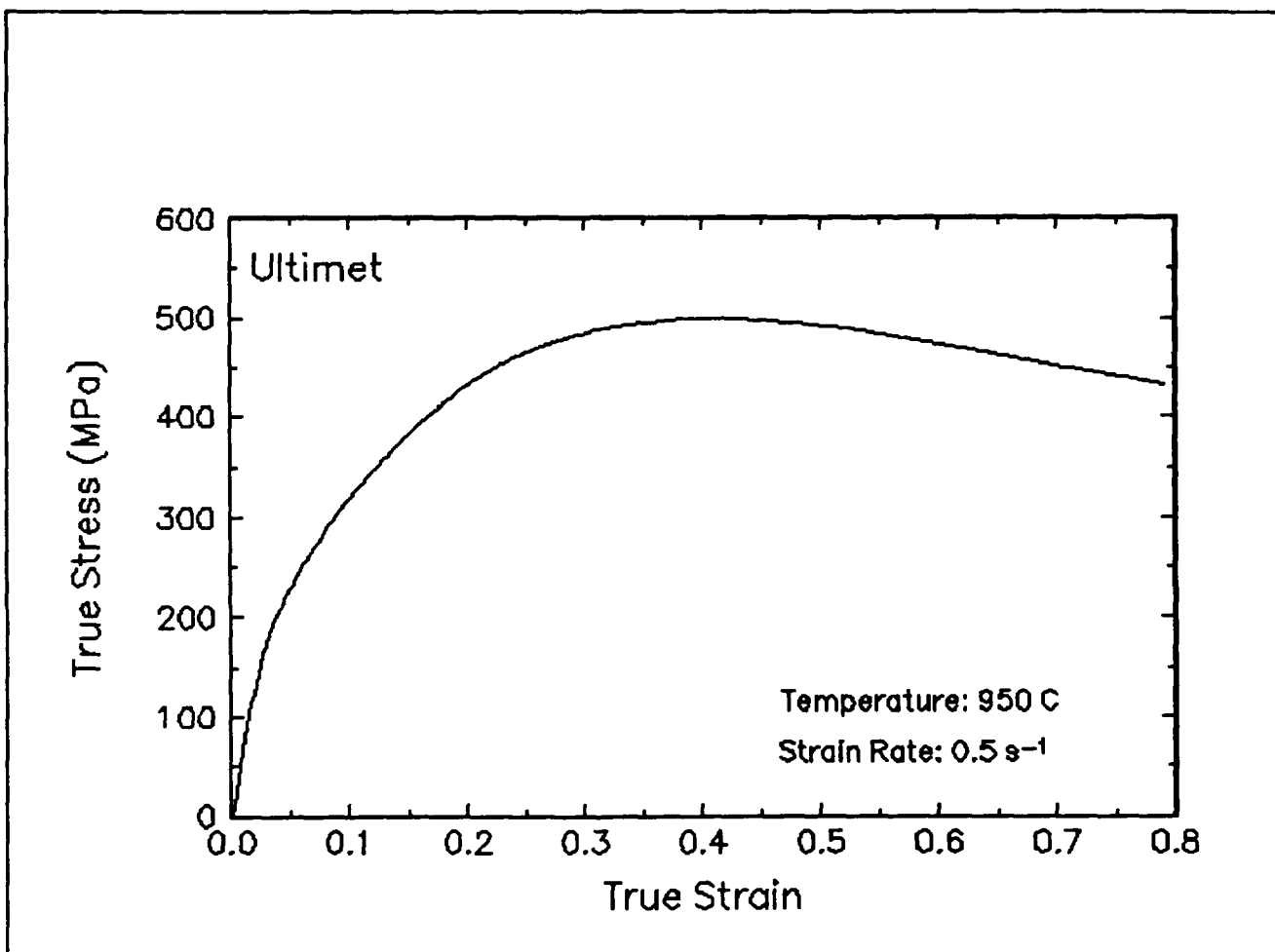


Figure 6. True stress-true strain curve, 950 C and 0.5 s⁻¹.

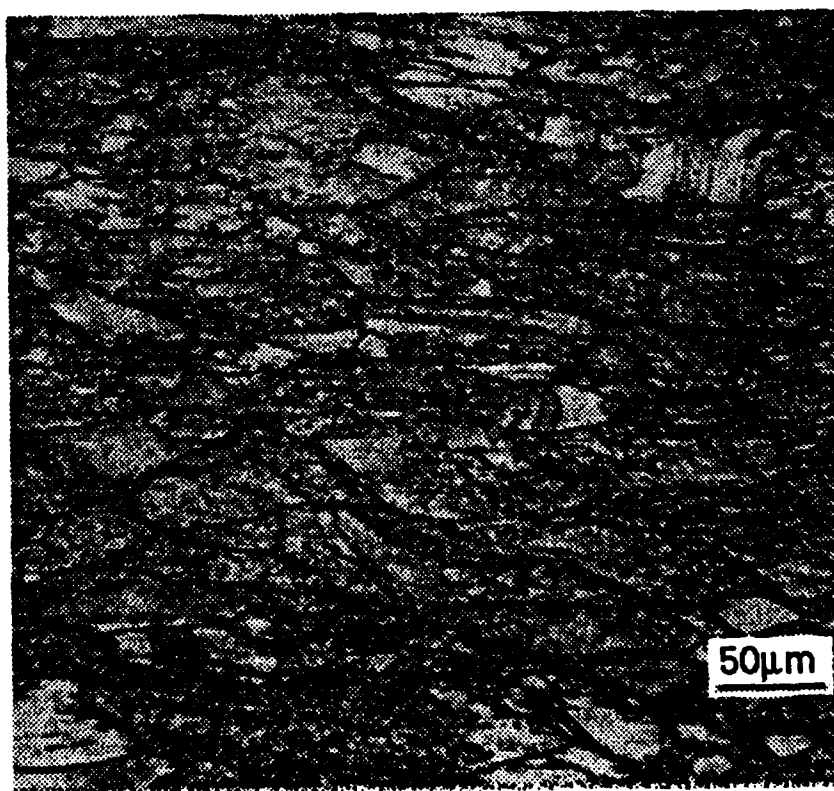
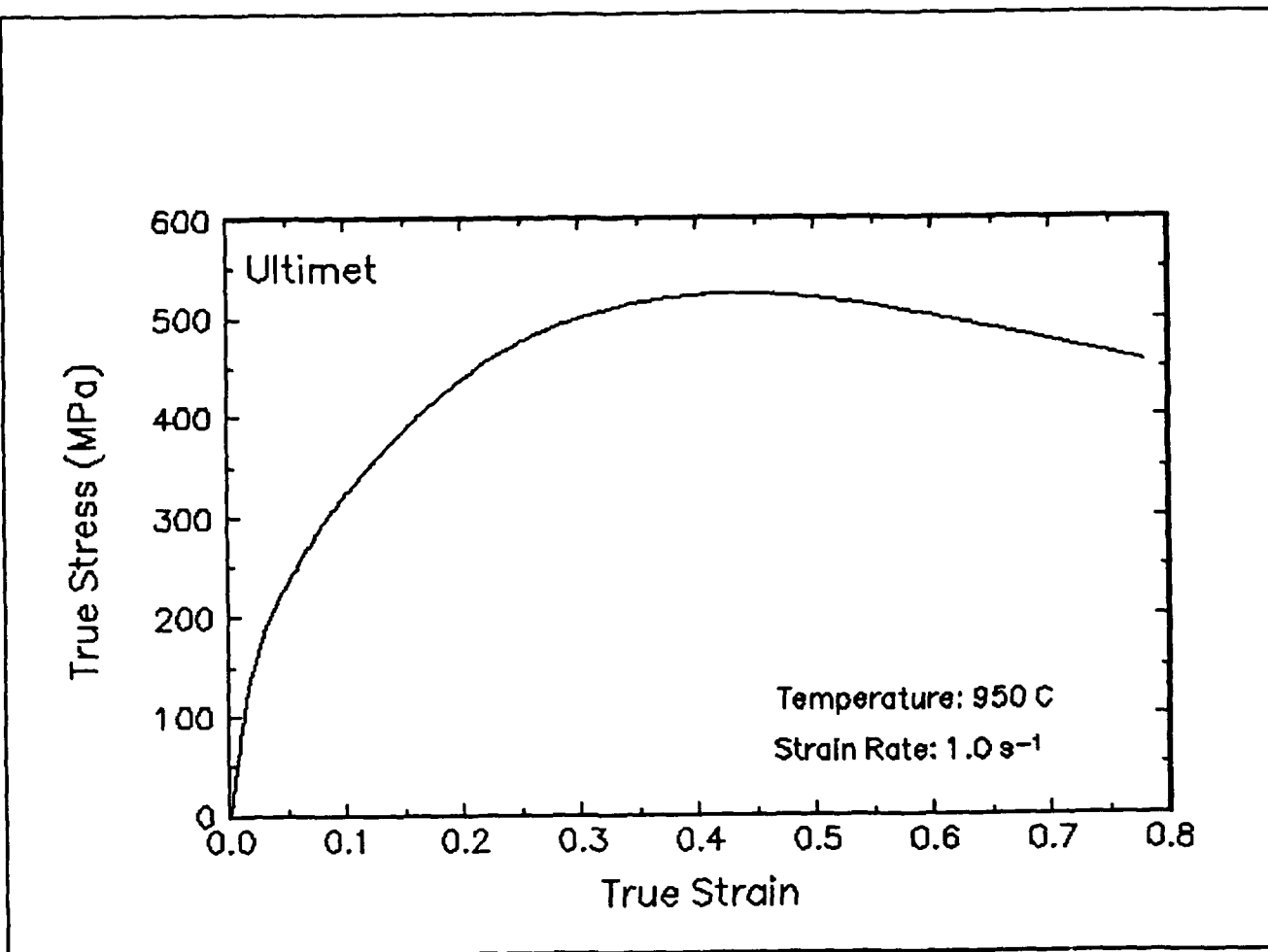


Figure 7. True stress-true strain curve and an optical micrograph from the center of the compressed sample cut through the compression axis, 950 C and 1 s⁻¹.

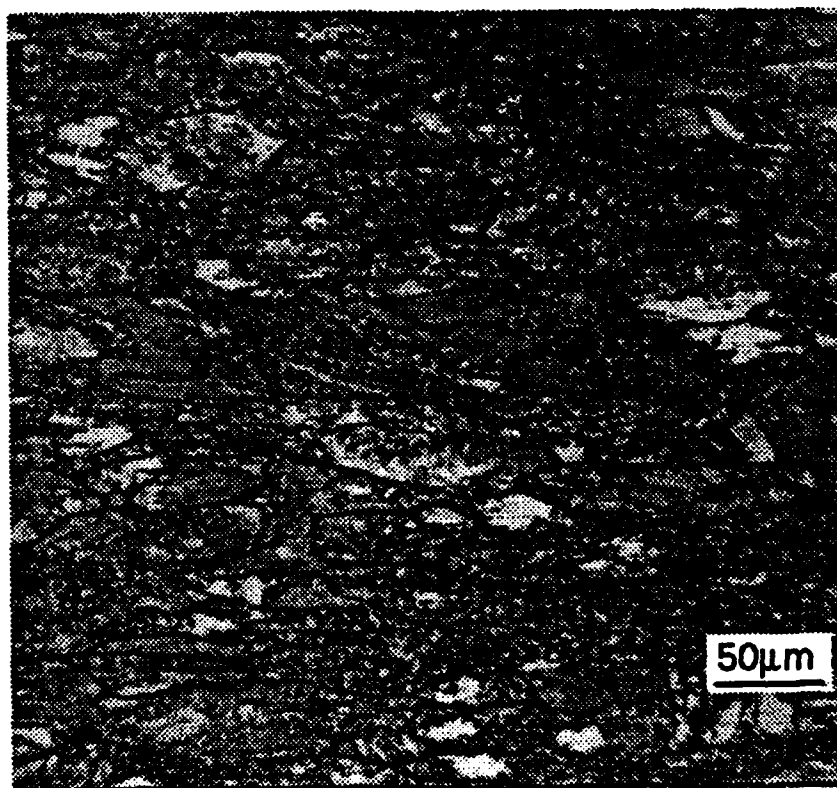
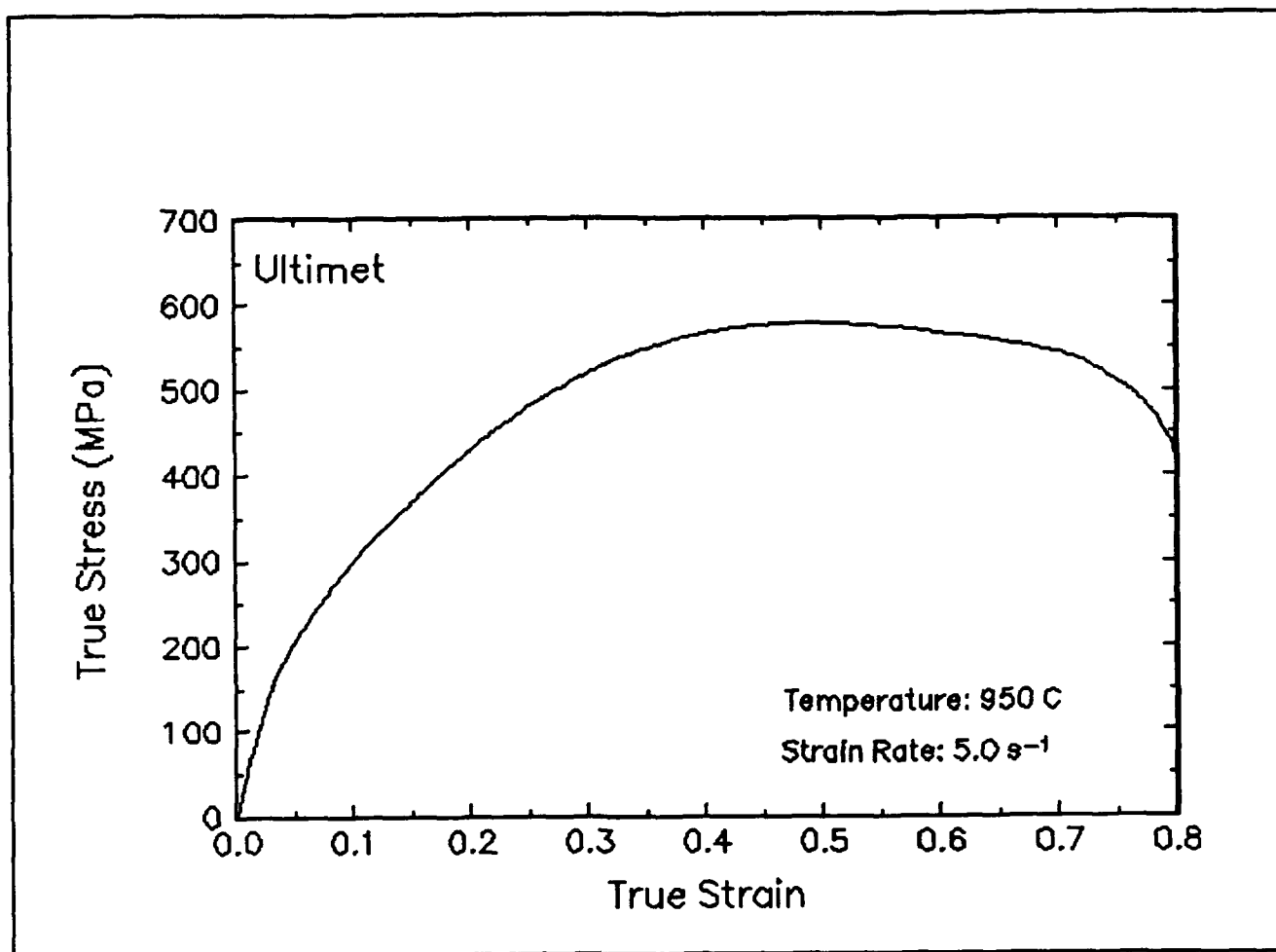


Figure 8. True stress-true strain curve and an optical micrograph from the center of the compressed sample cut through the compression axis, 950 C and 5 s⁻¹.

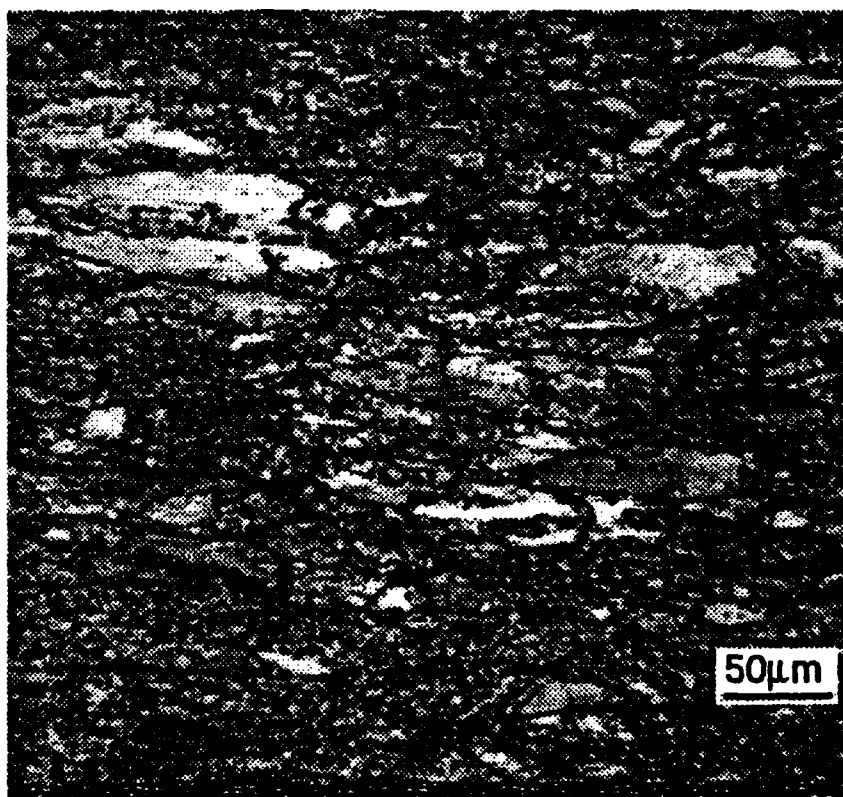
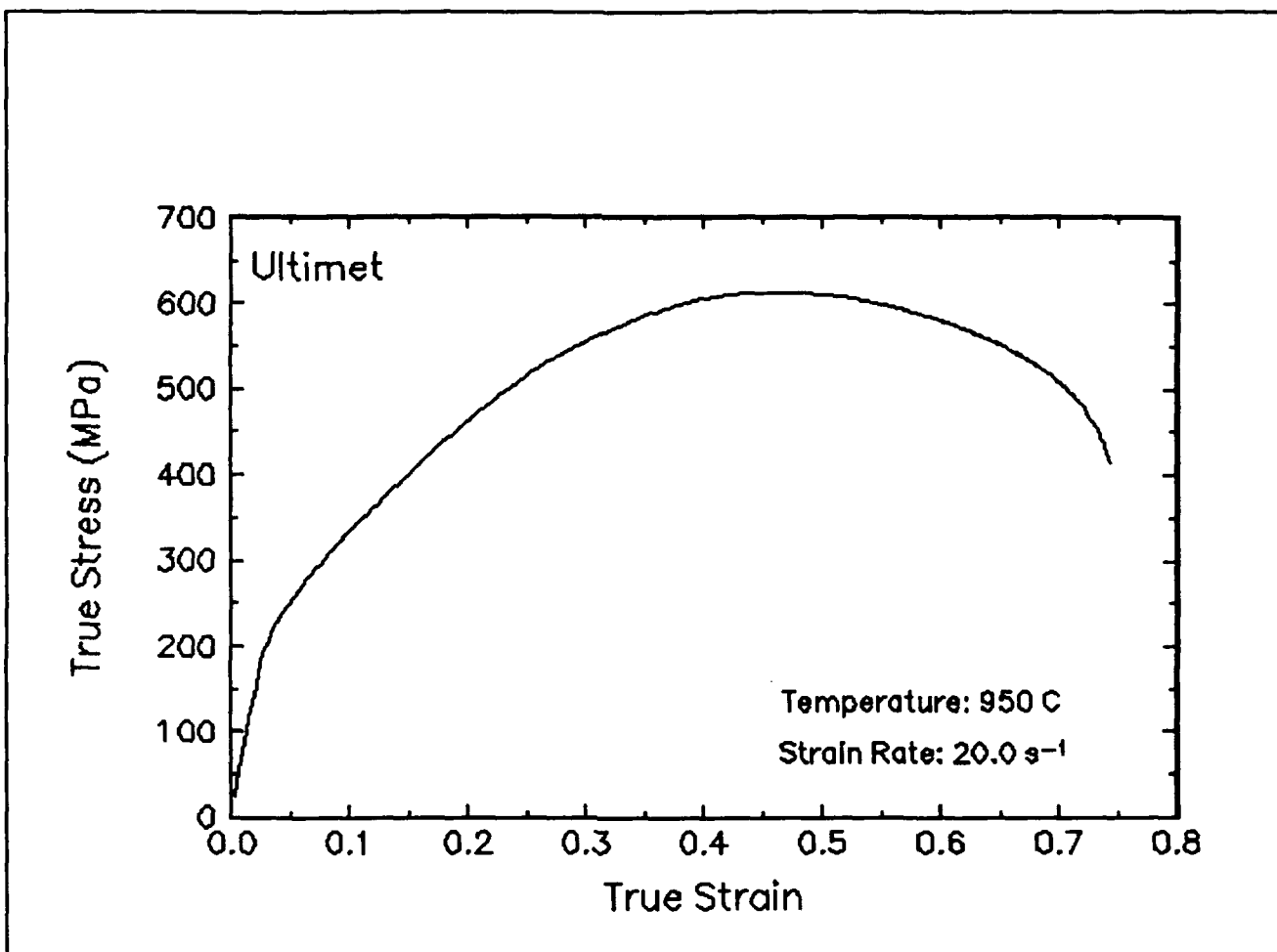


Figure 9. True stress-true strain curve and an optical micrograph from the center of the compressed sample cut through the compression axis, 950 C and 20 s⁻¹.

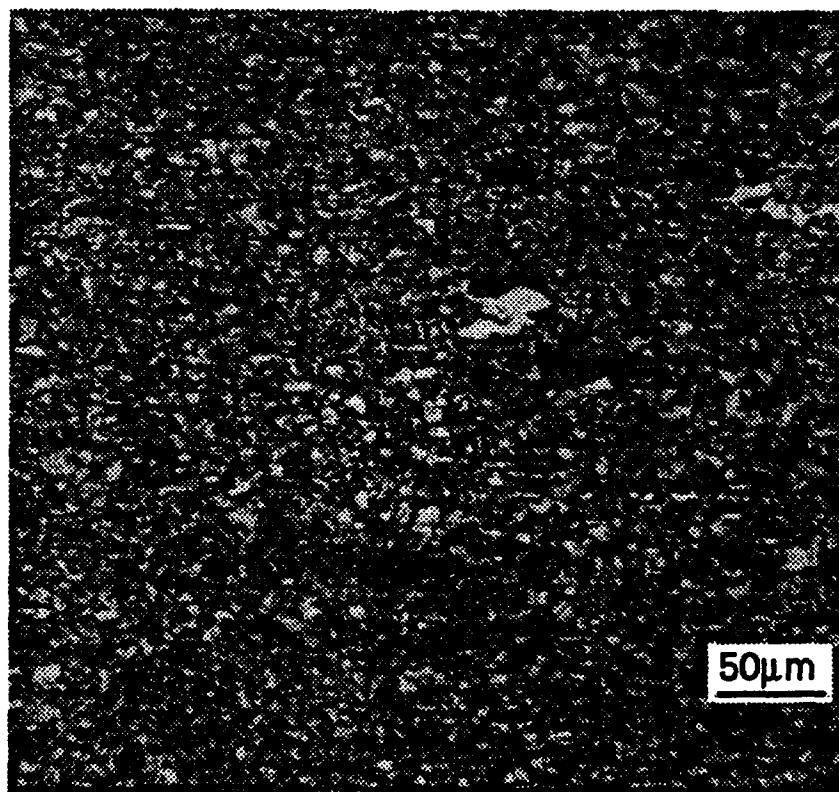
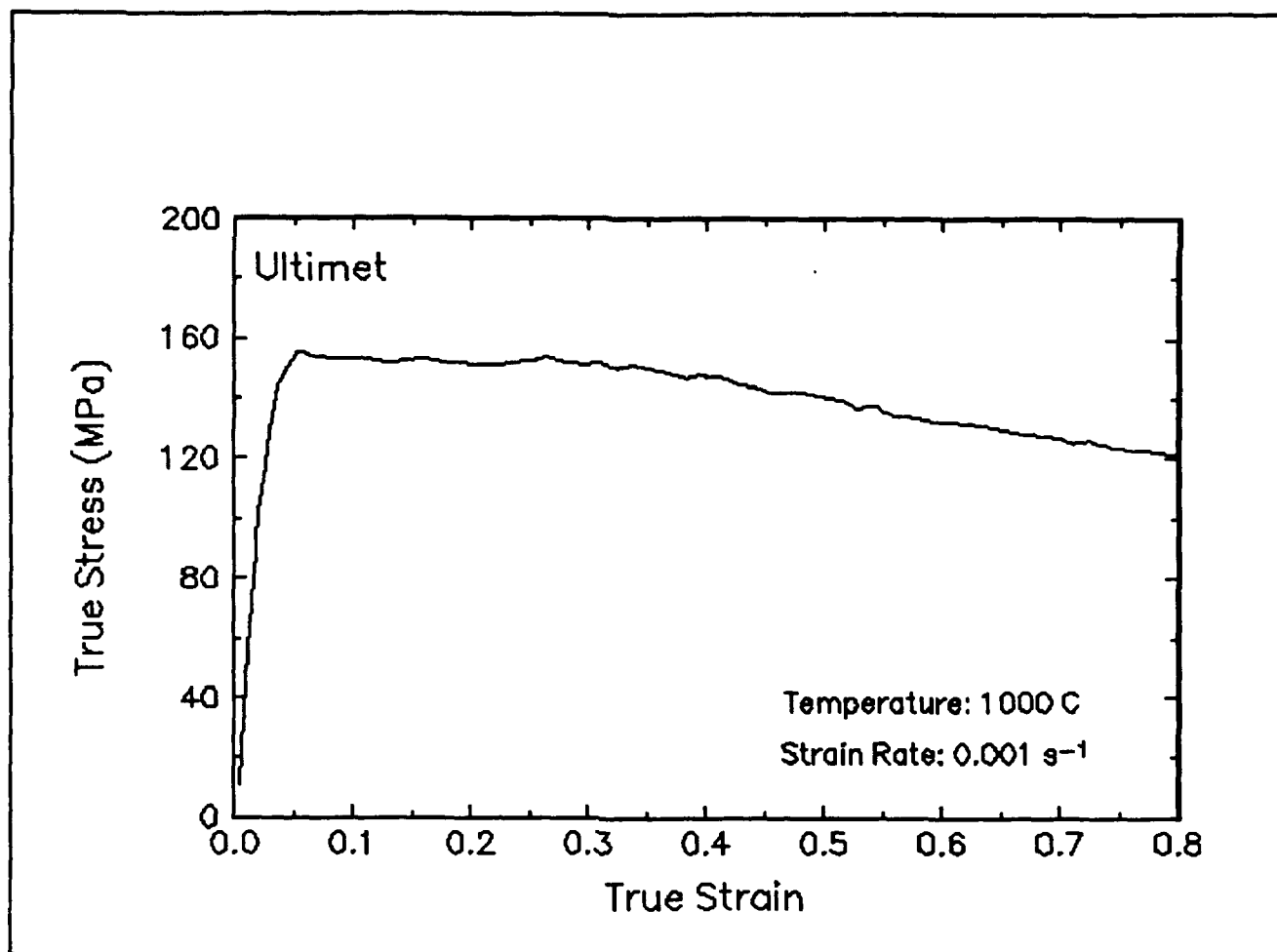


Figure 10. True stress-true strain curve and an optical micrograph from the center of the compressed sample cut through the compression axis, 1000 C and 0.001 s⁻¹.

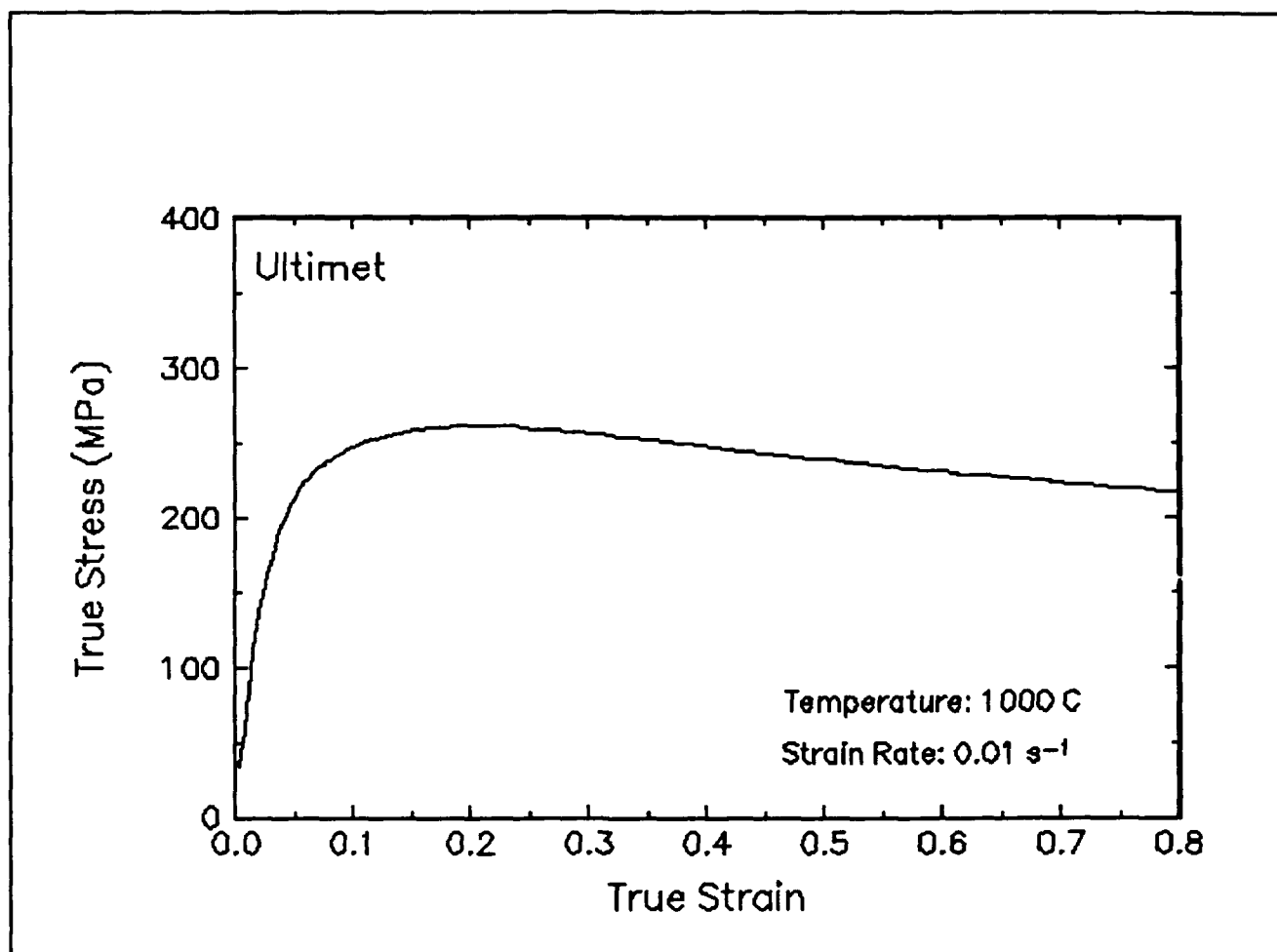


Figure 11. True stress-true strain curve, 1000 C and 0.01 s⁻¹.

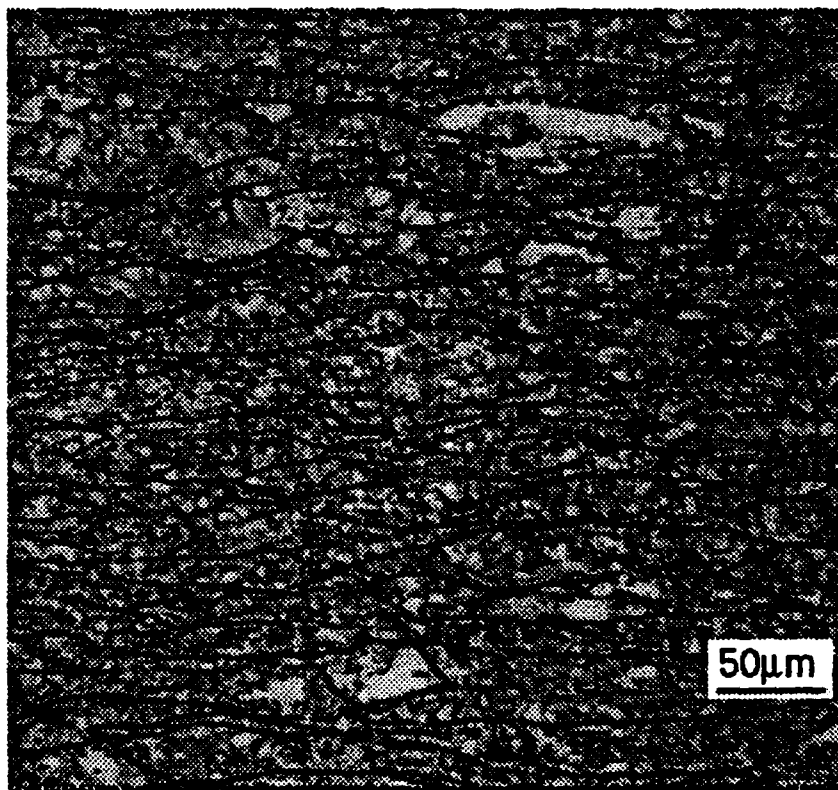
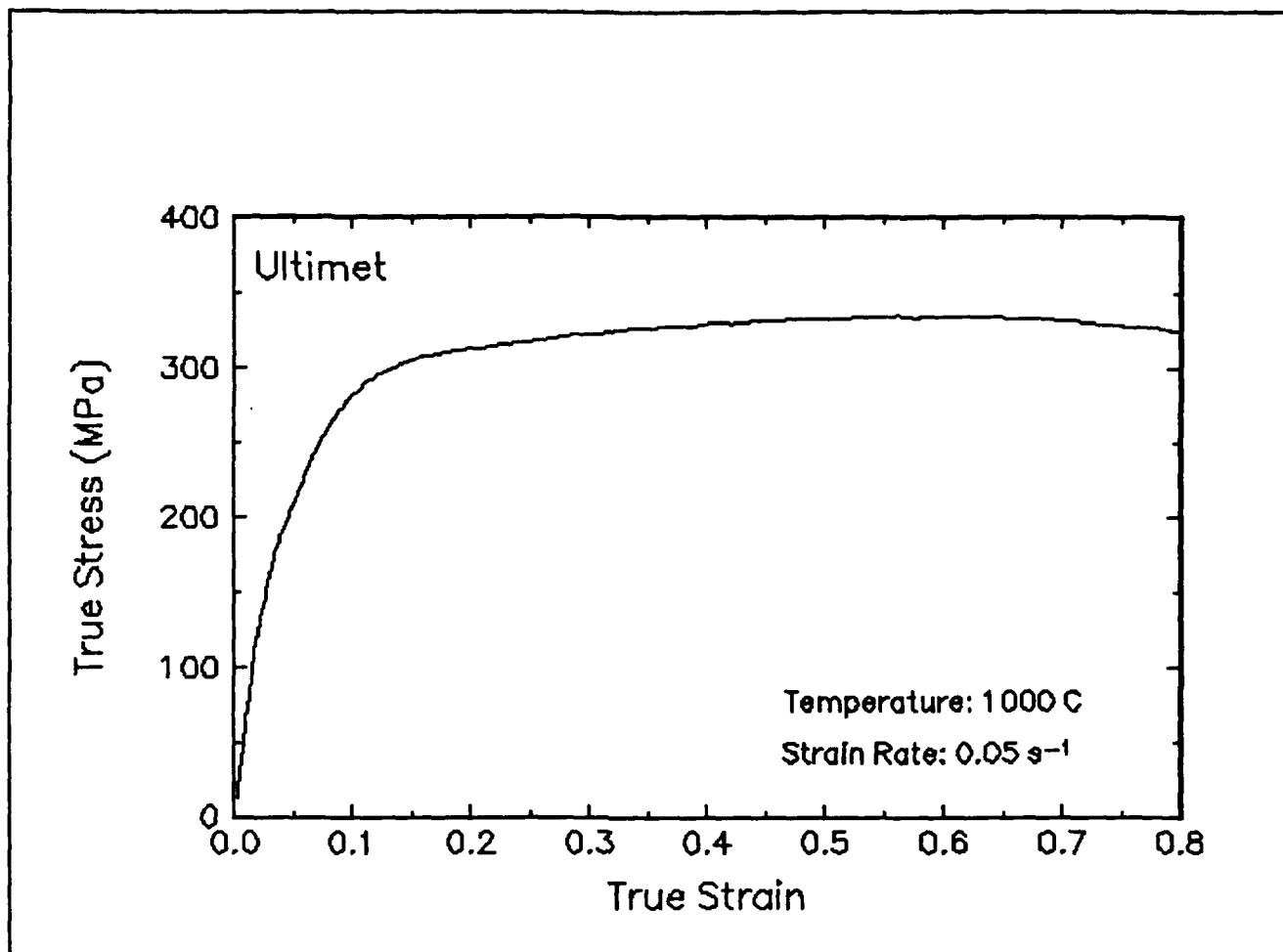


Figure 12. True stress-true strain curve and an optical micrograph from the center of the compressed sample cut through the compression axis, 1000 C and 0.05 s⁻¹.

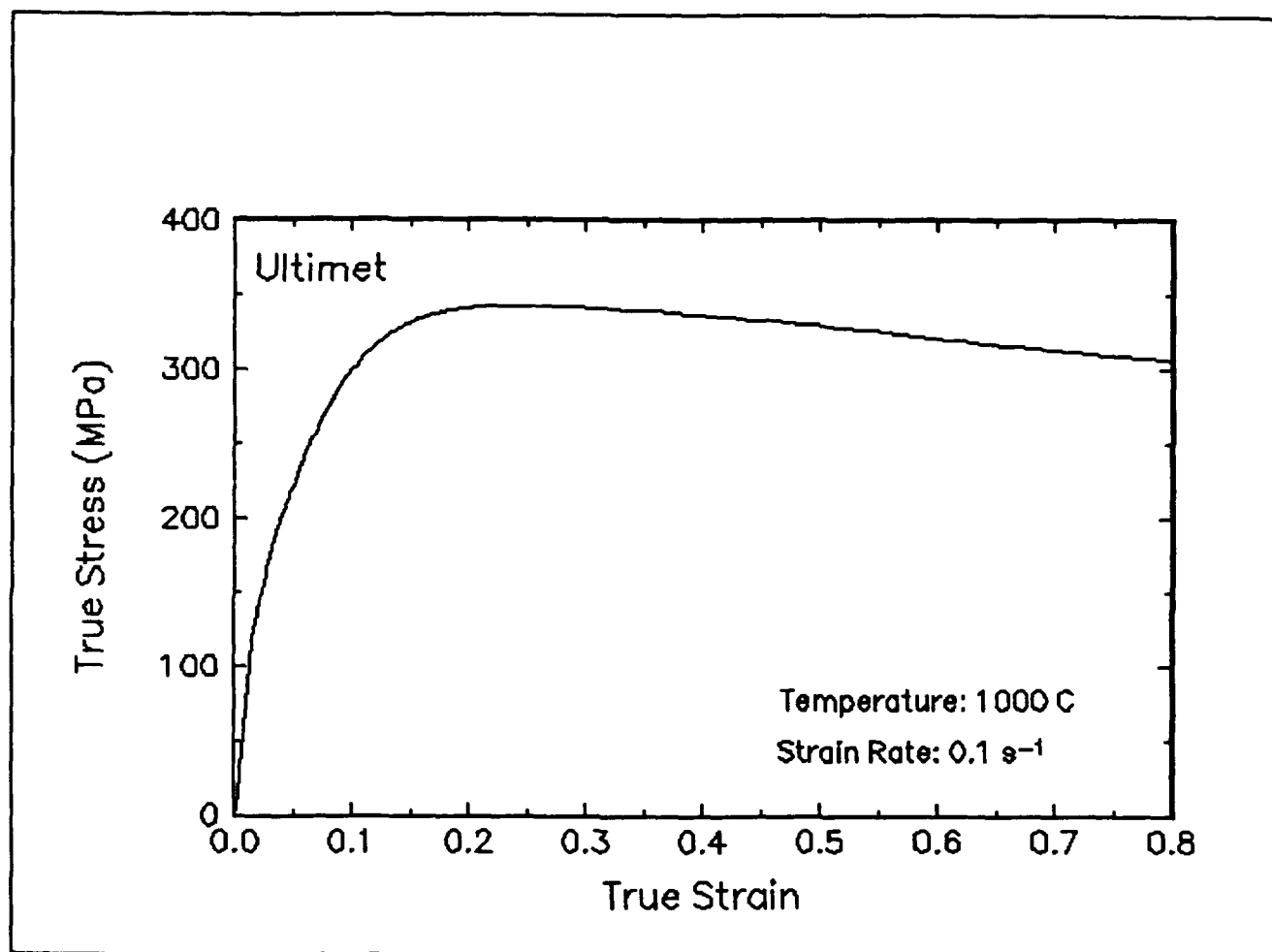


Figure 13. True stress-true strain curve, 1000 C and 0.1 s⁻¹.

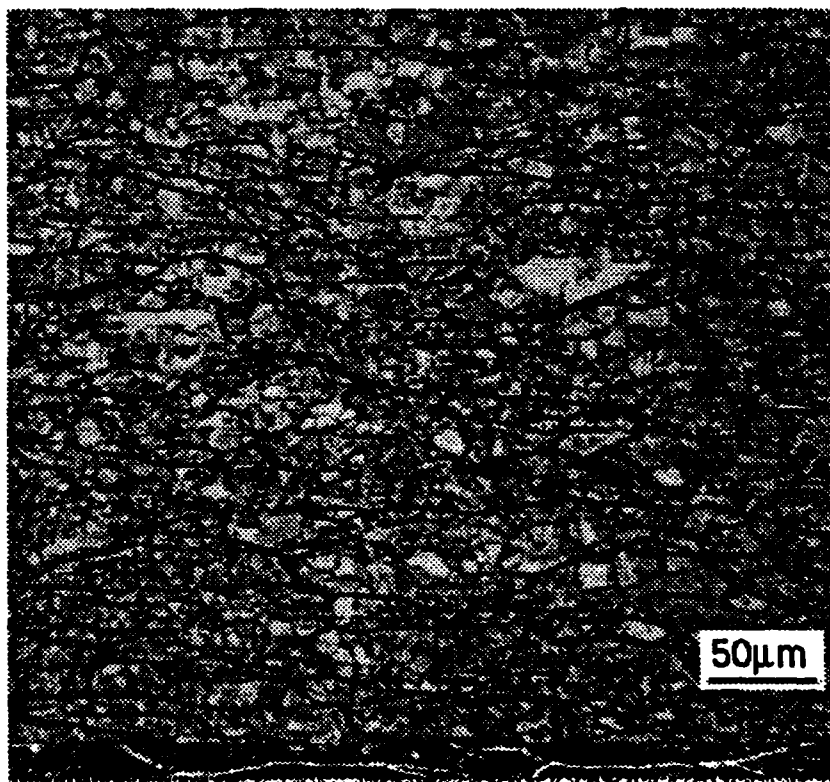
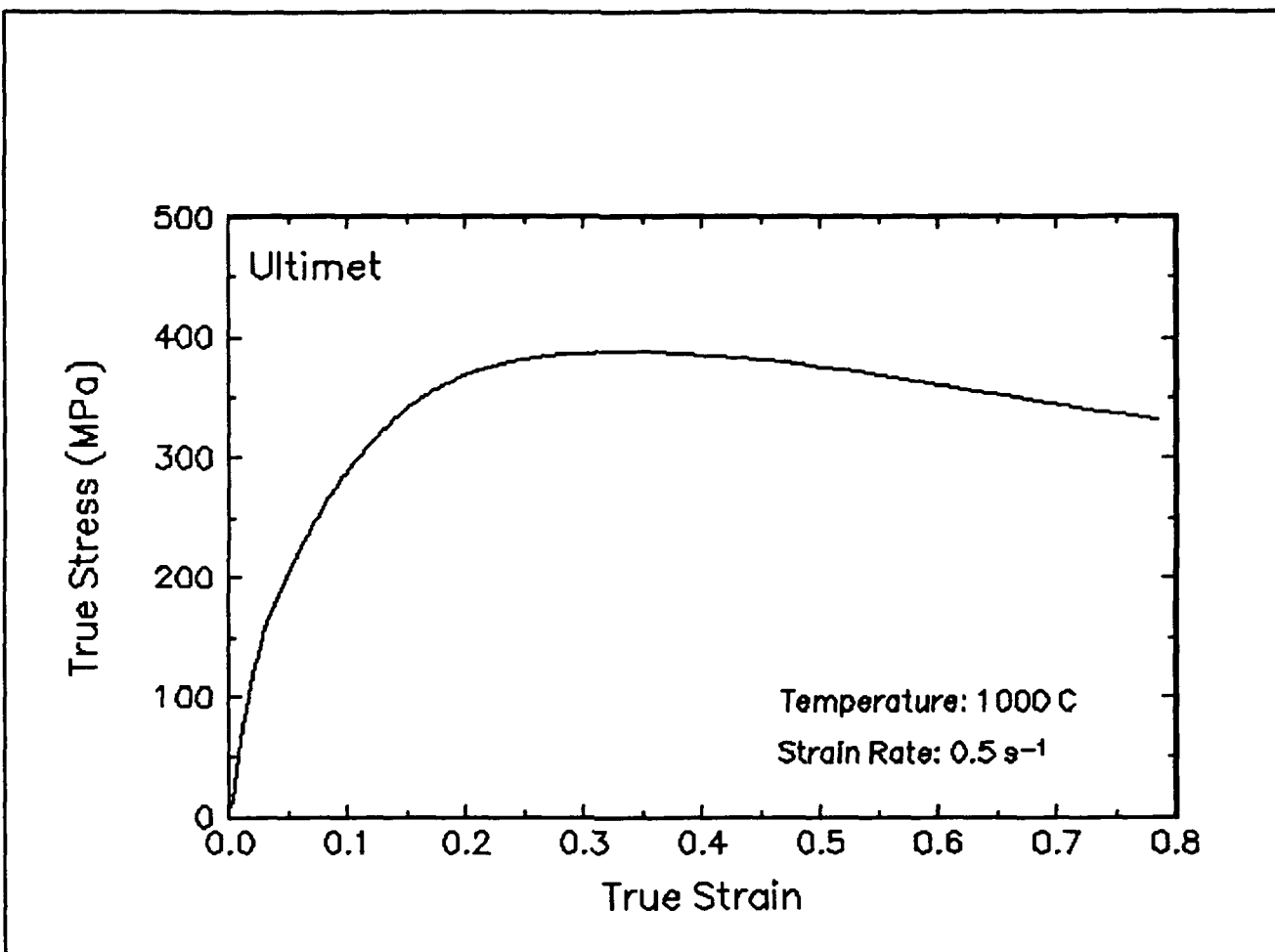


Figure 14. True stress-true strain curve and an optical micrograph from the center of the compressed sample cut through the compression axis, 1000 C and 0.5 s⁻¹.

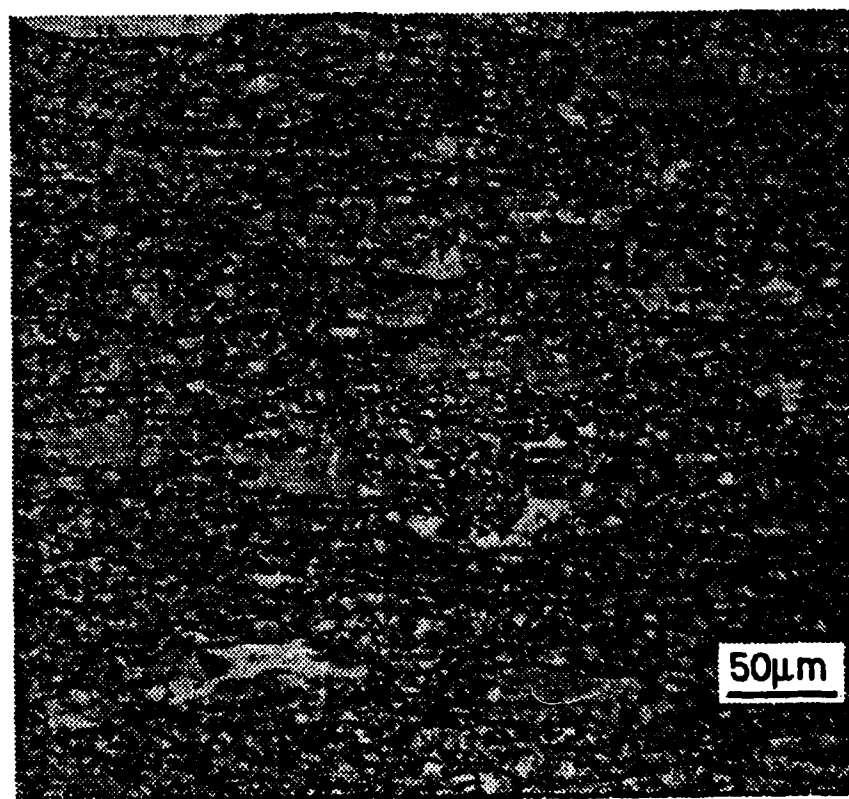
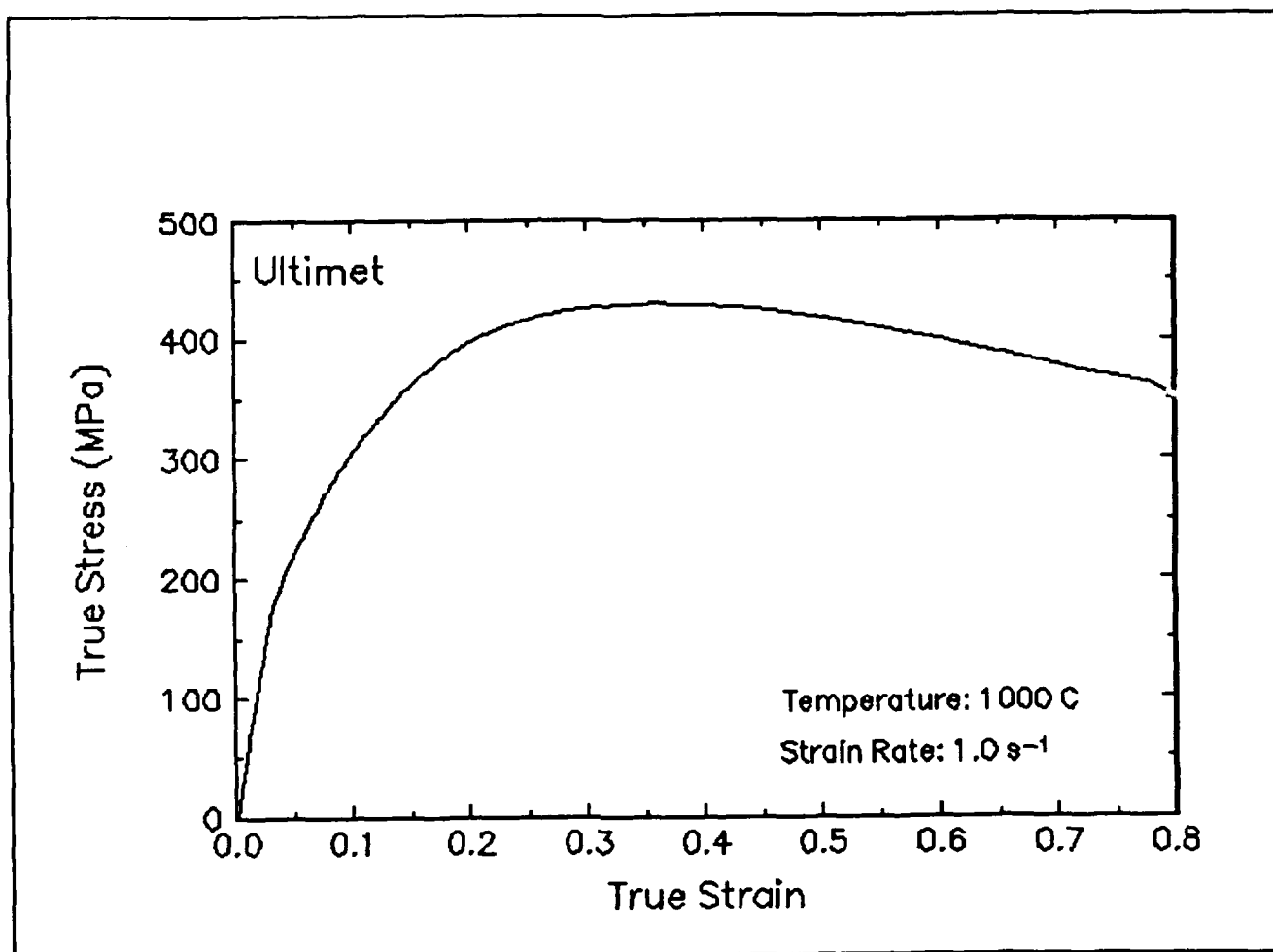


Figure 15. True stress-true strain curve and an optical micrograph from the center of the compressed sample cut through the compression axis, 1000 C and 1 s⁻¹.

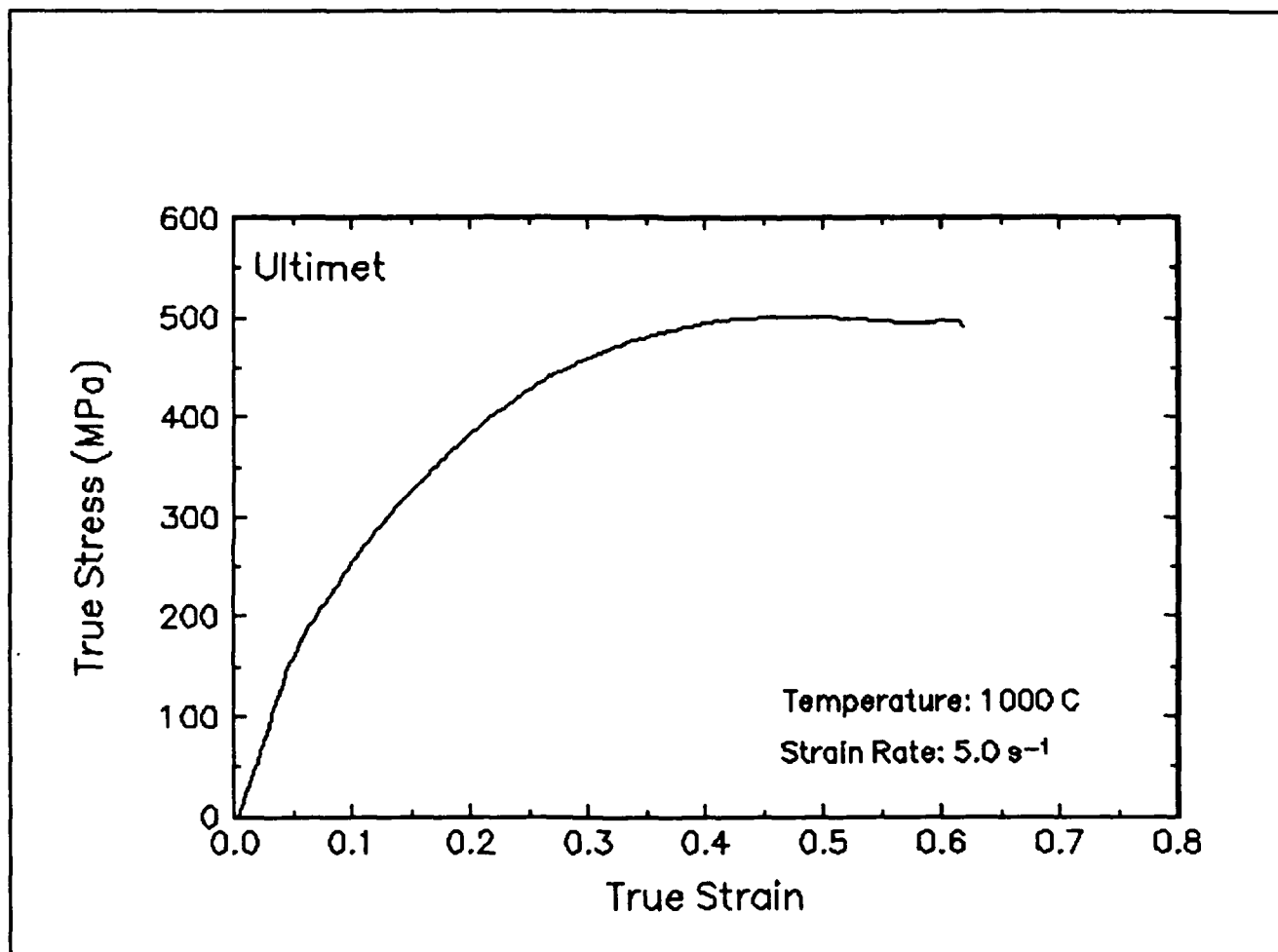


Figure 16. True stress-true strain curve, 1000 C and 5 s⁻¹.

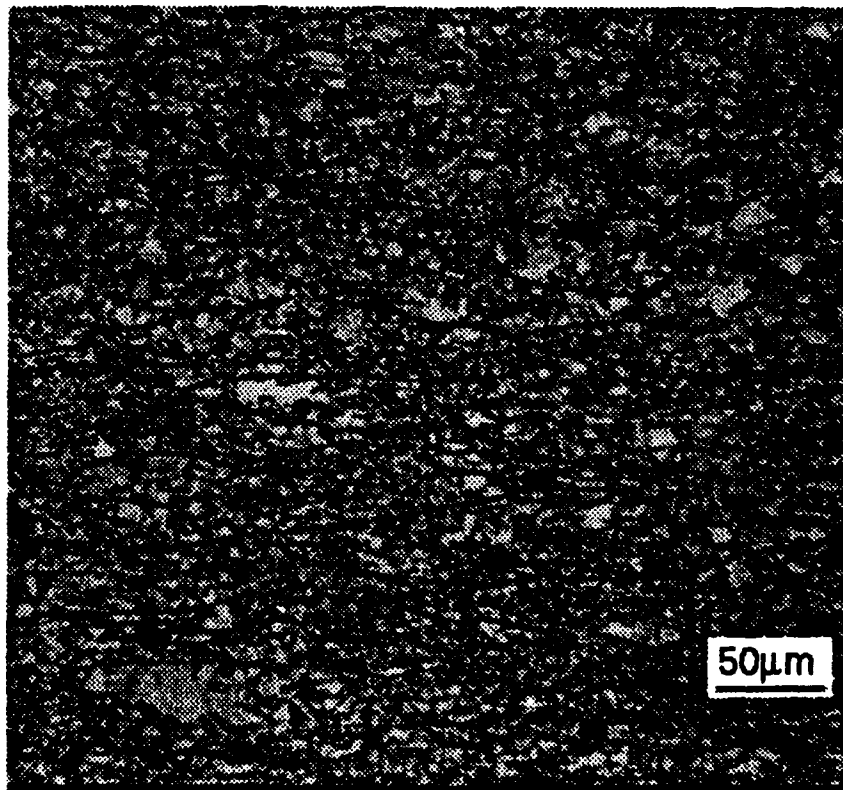
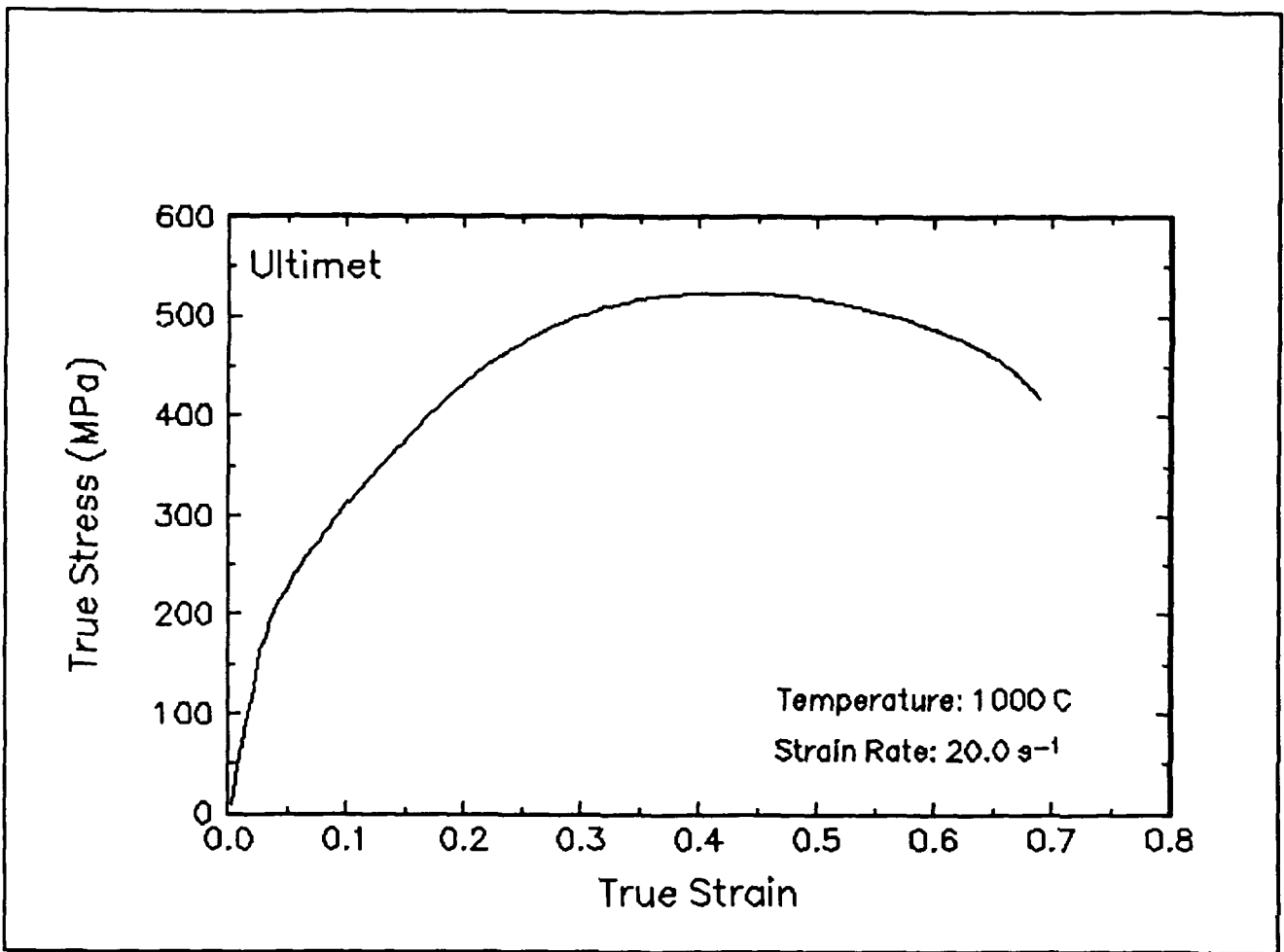


Figure 17. True stress-true strain curve and an optical micrograph from the center of the compressed sample cut through the compression axis, 1000 C and 20 s⁻¹.

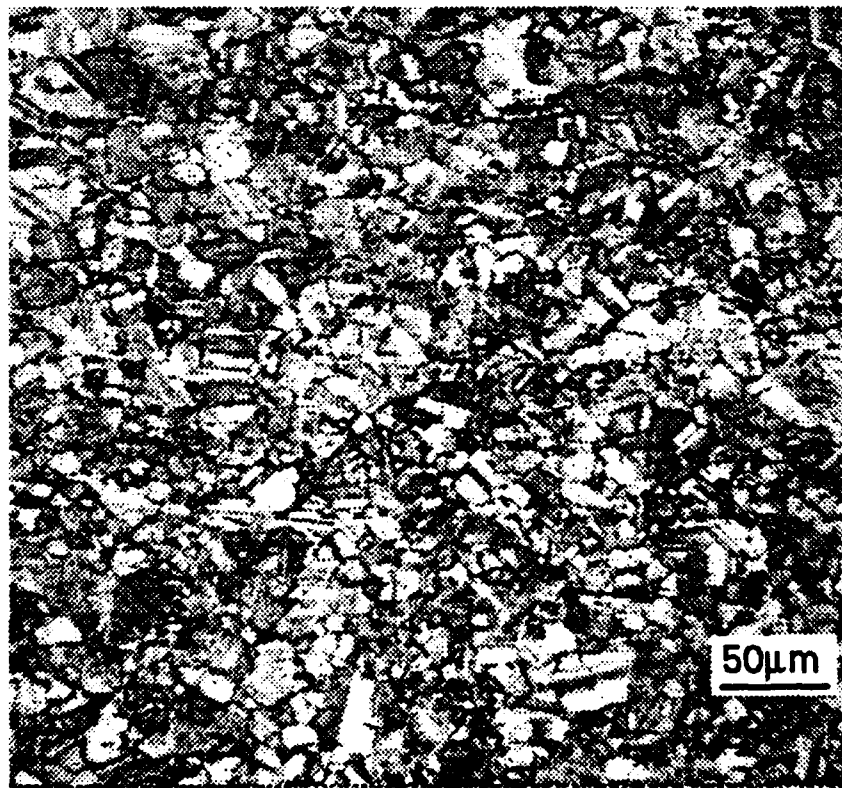
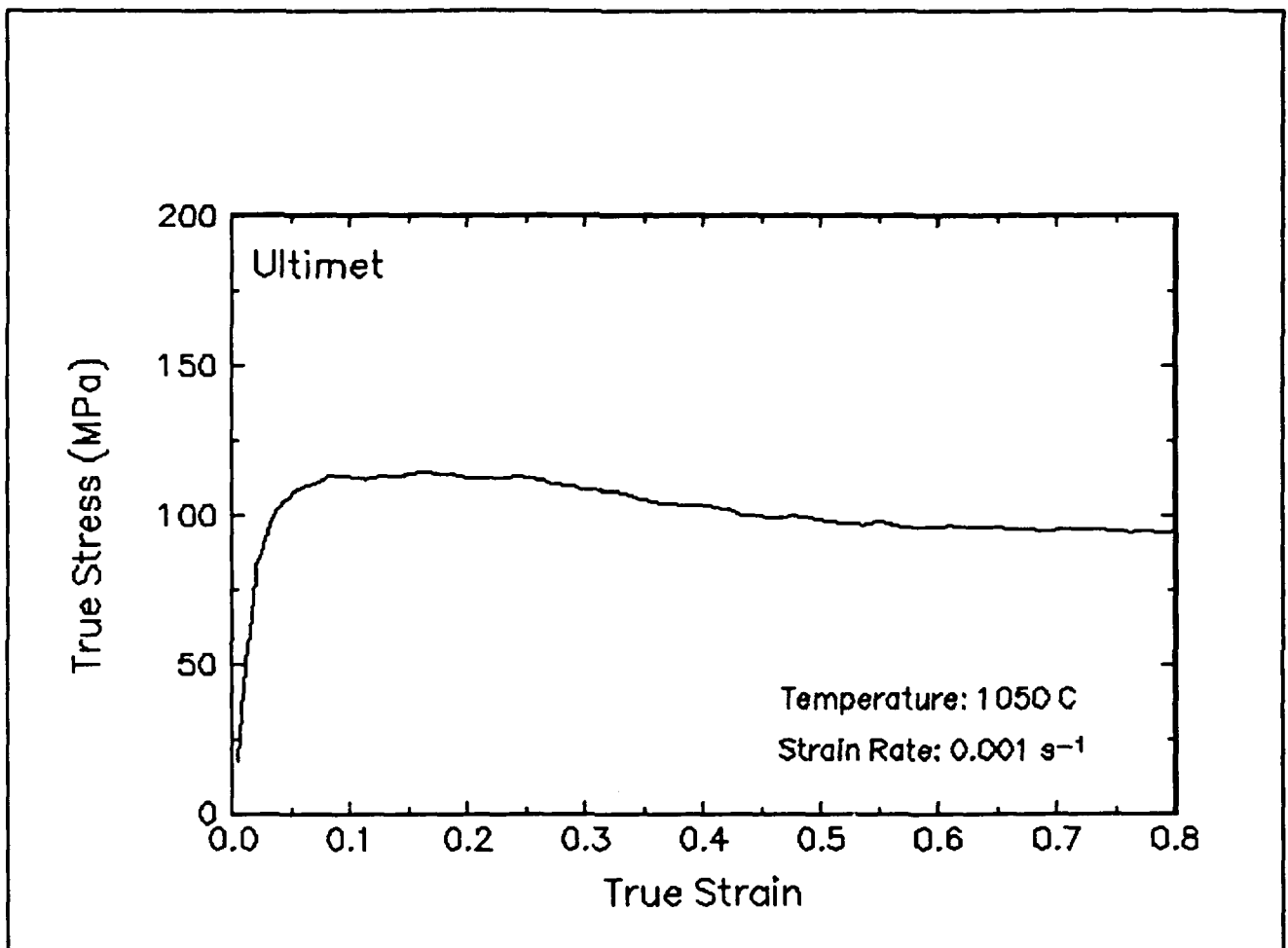


Figure 18. True stress-true strain curve and an optical micrograph from the center of the compressed sample cut through the compression axis, 1050 C and 0.001 s⁻¹.

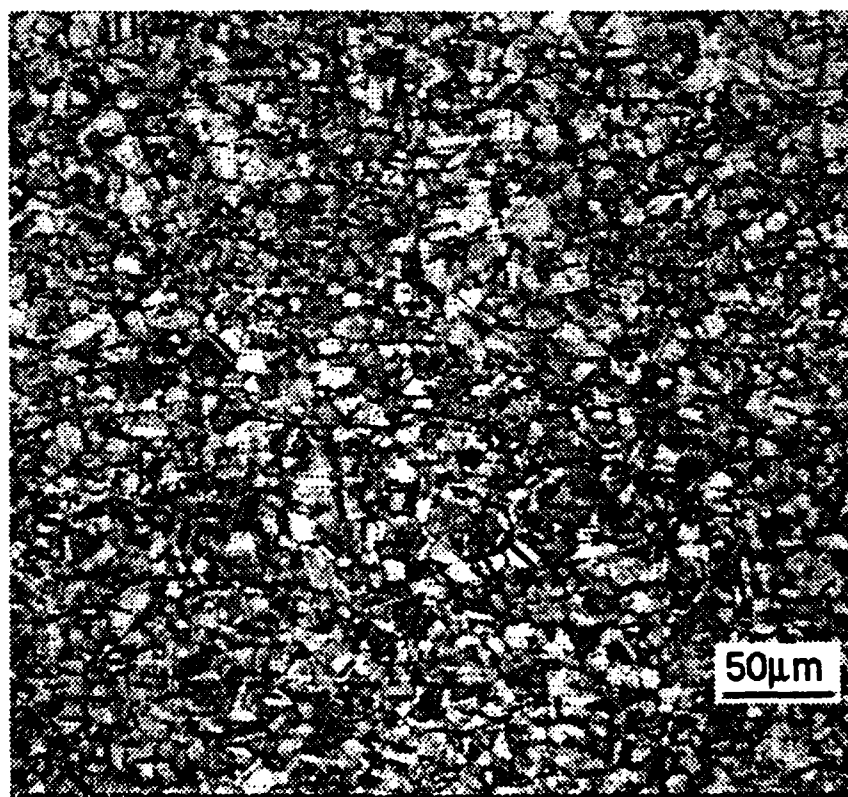
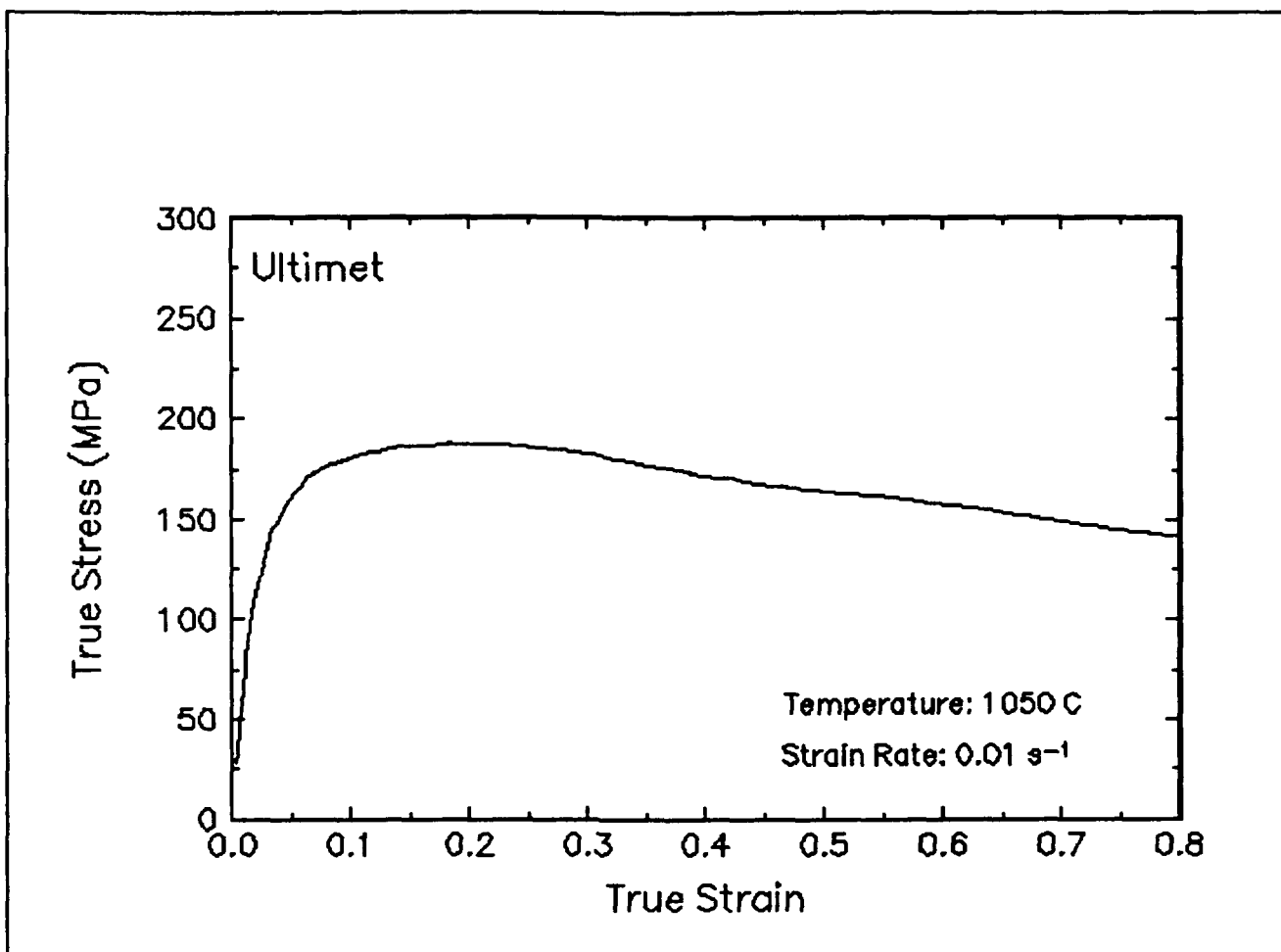


Figure 19. True stress-true strain curve and an optical micrograph from the center of the compressed sample cut through the compression axis, 1050 C and 0.01 s⁻¹.

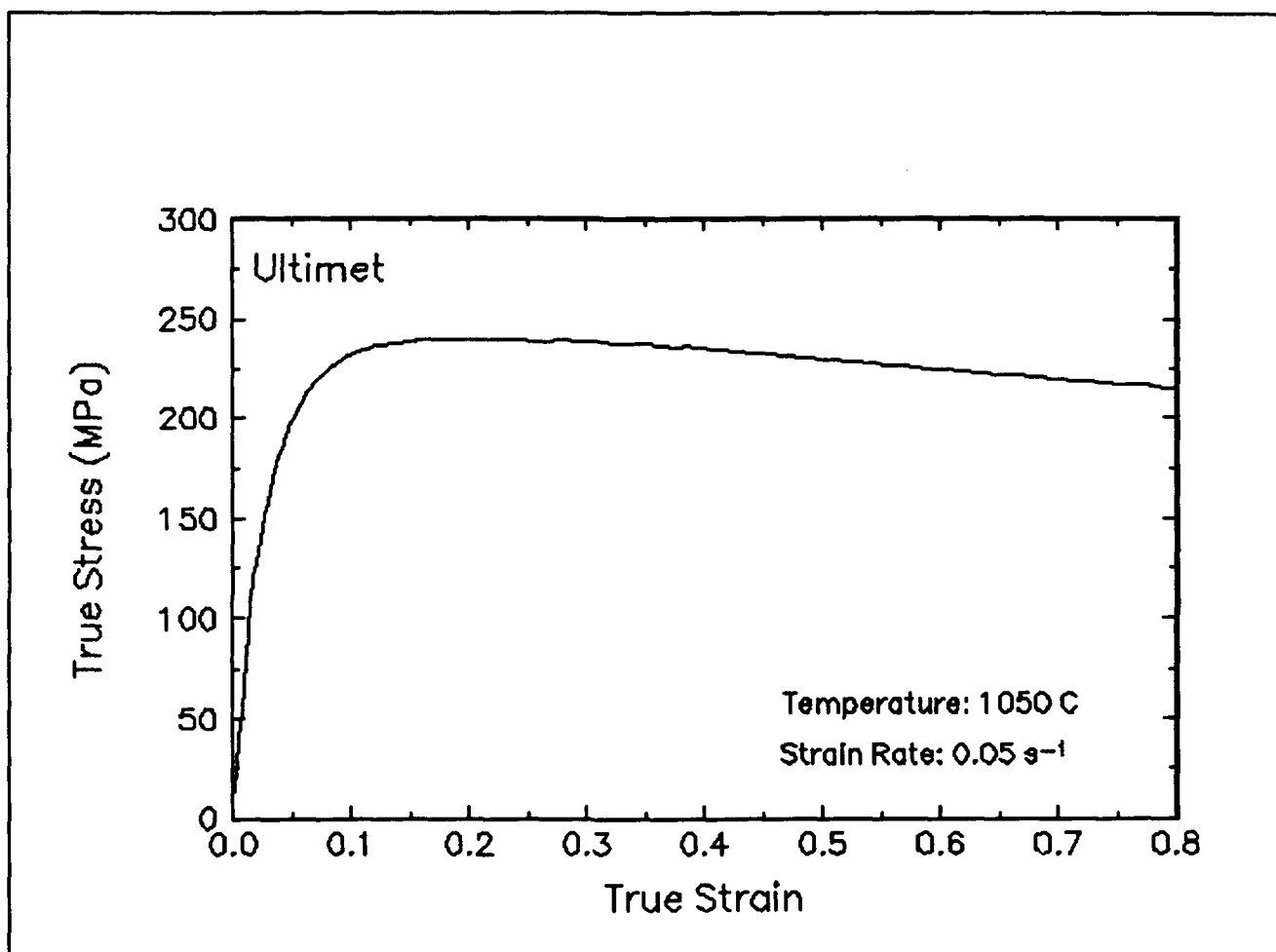


Figure 20. True stress-true strain curve, 1050 C and 0.05 s⁻¹.

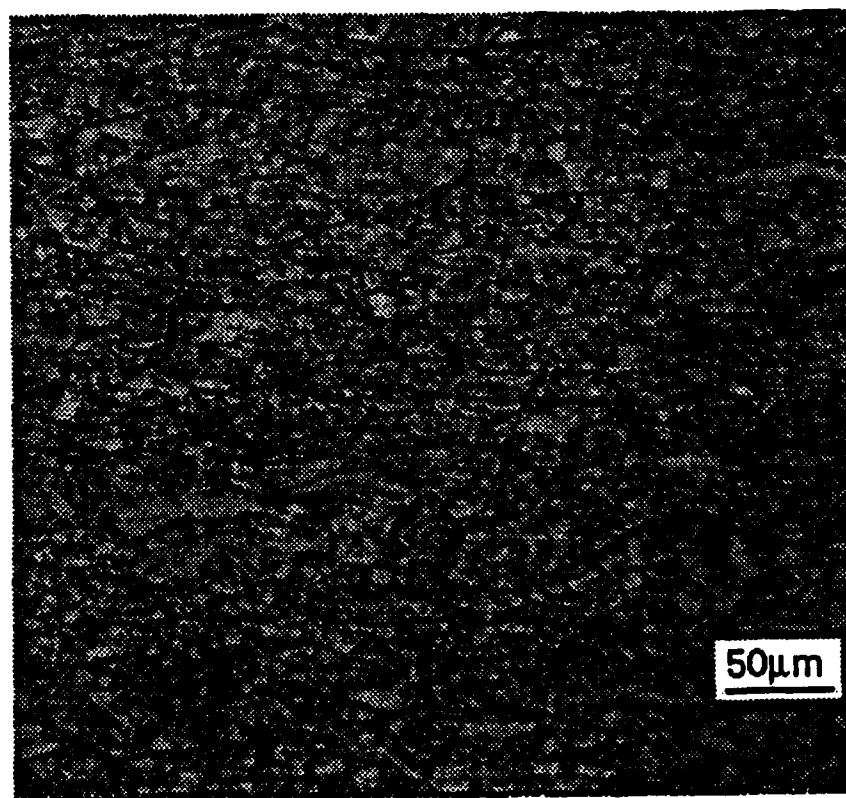
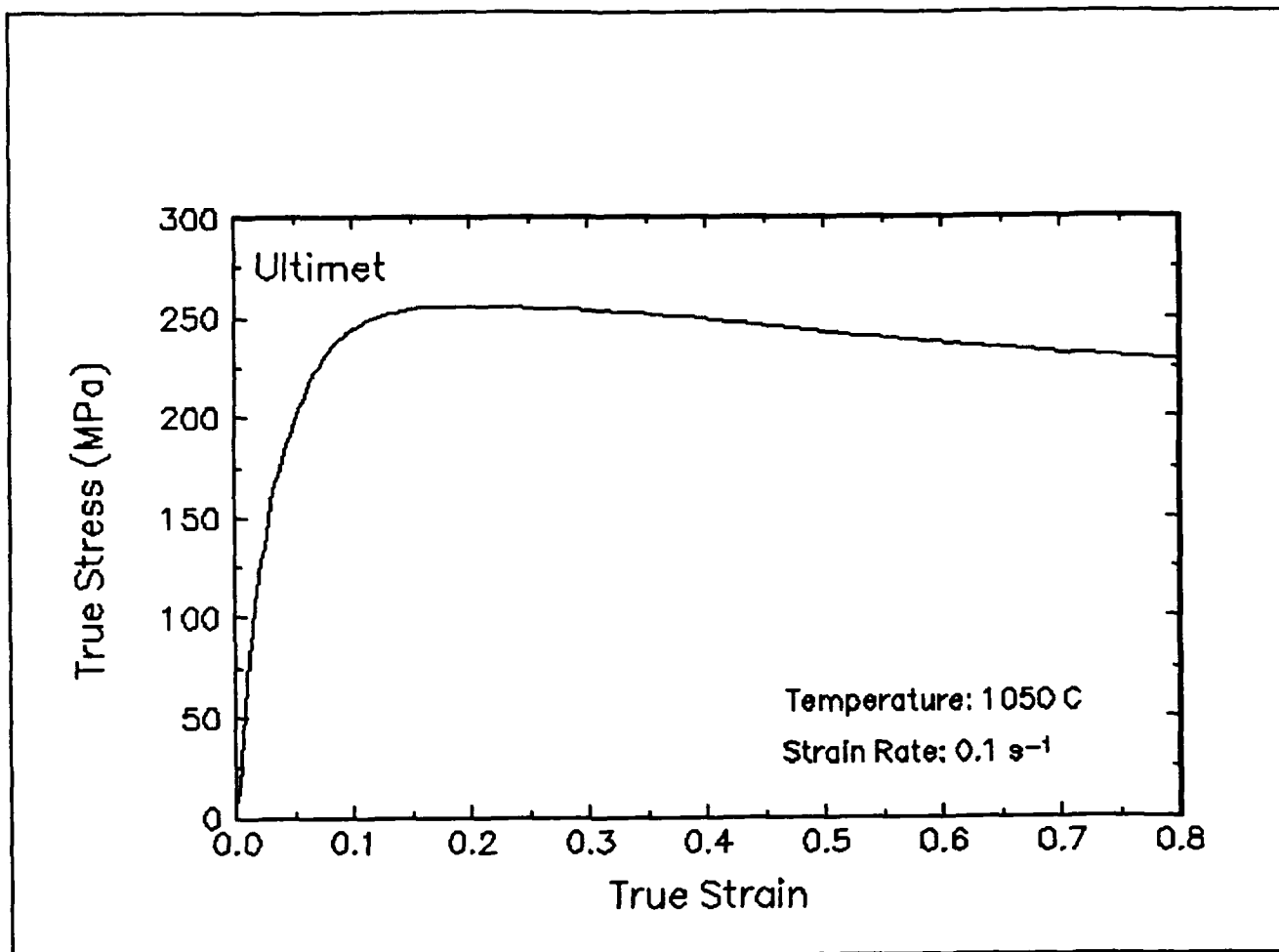


Figure 21. True stress-true strain curve and an optical micrograph from the center of the compressed sample cut through the compression axis, 1050 C and 0.1 s⁻¹.

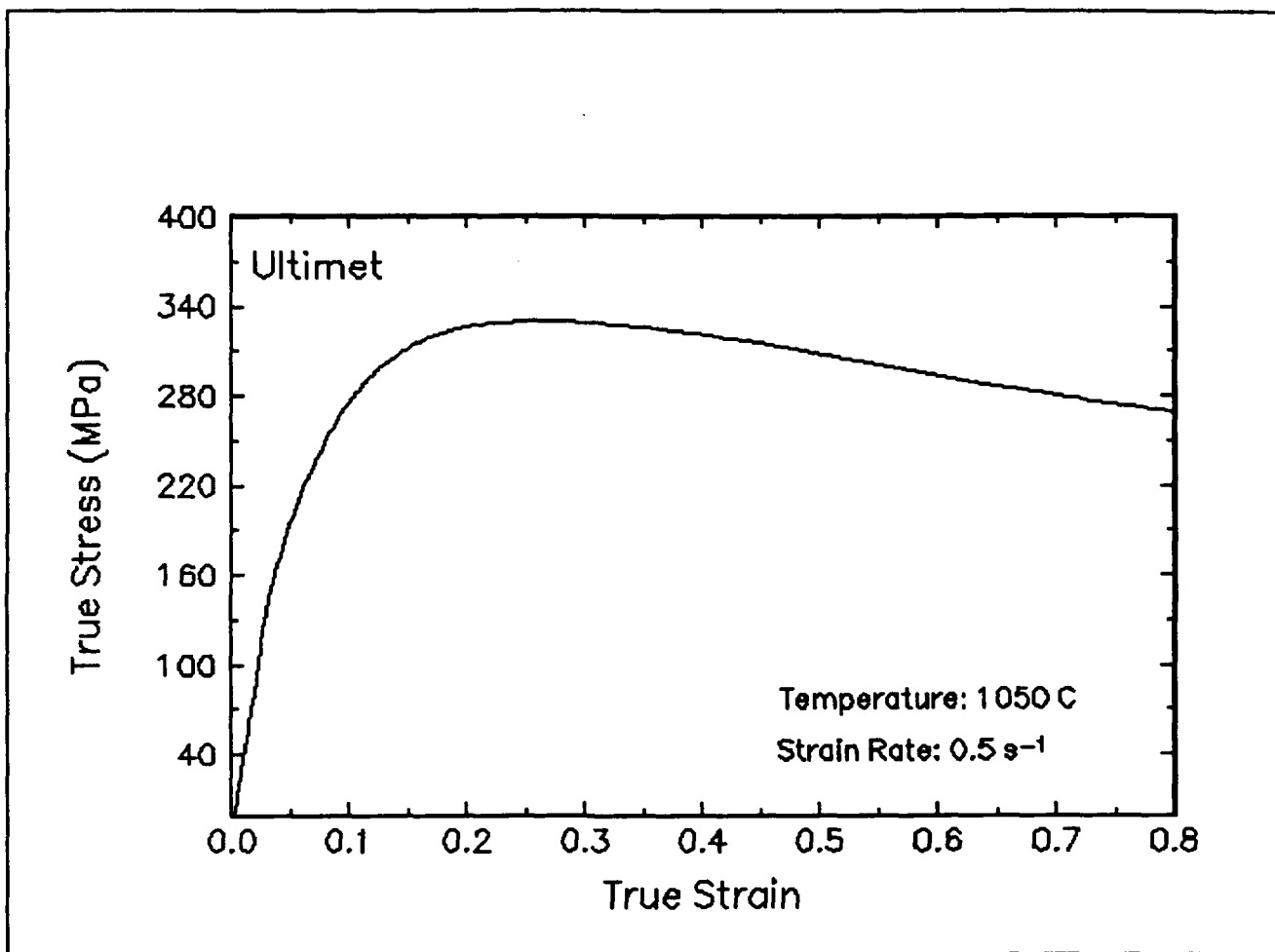


Figure 22. True stress-true strain curve, 1050 C and 0.5 s⁻¹.

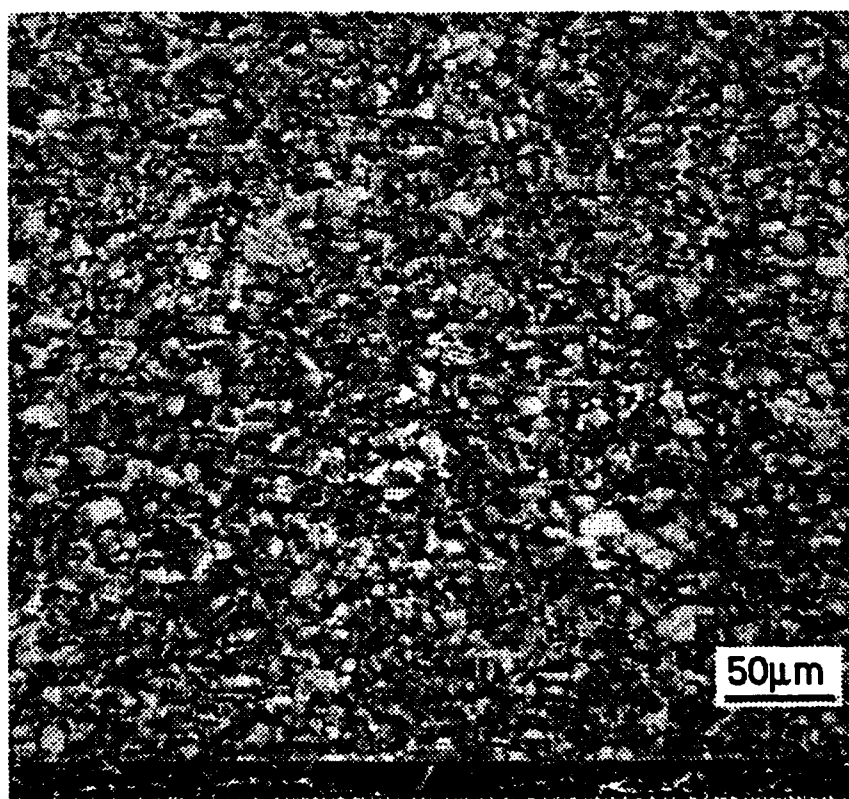
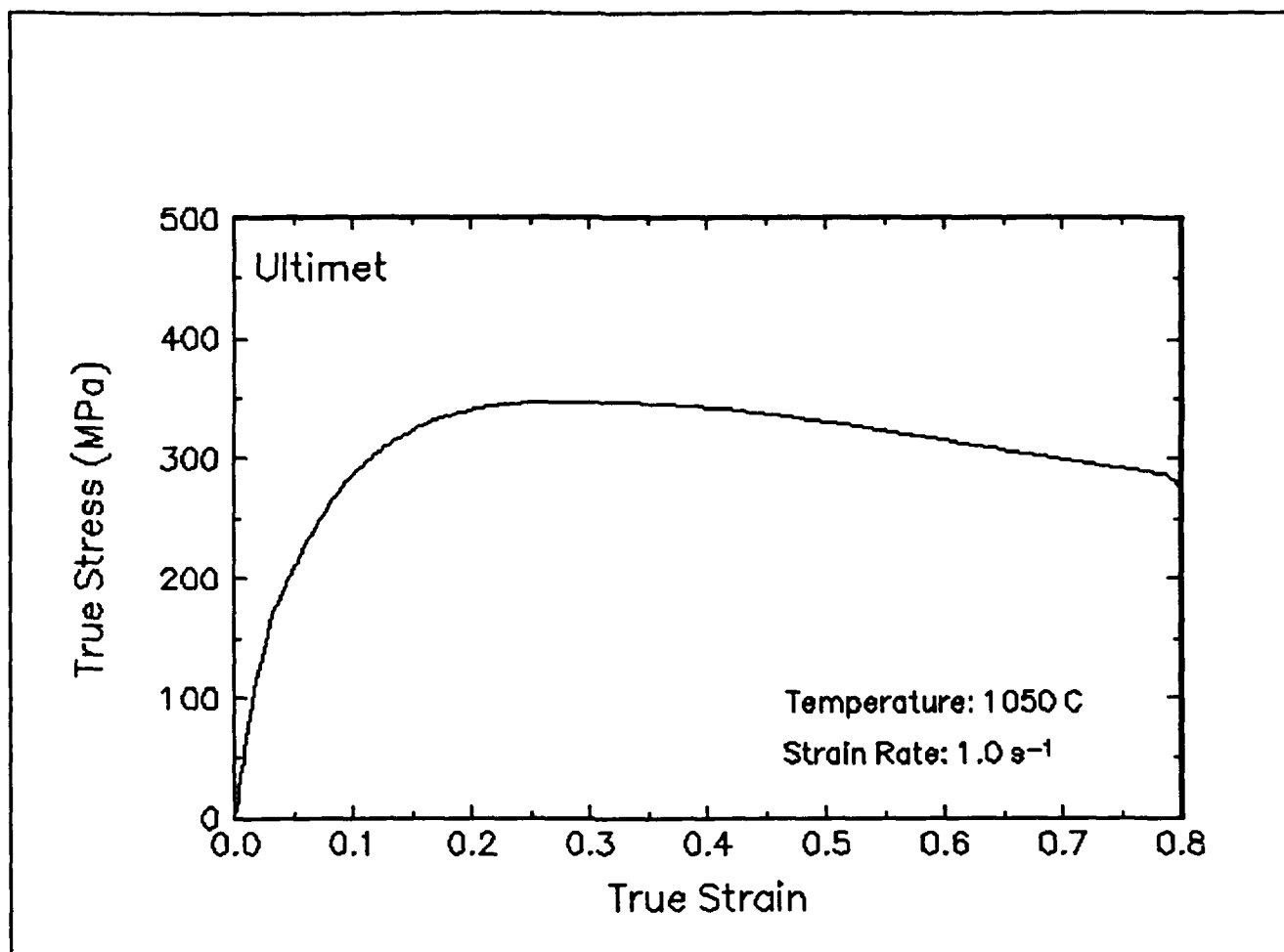


Figure 23. True stress-true strain curve and an optical micrograph from the center of the compressed sample cut through the compression axis, 1050 C and 1 s⁻¹.

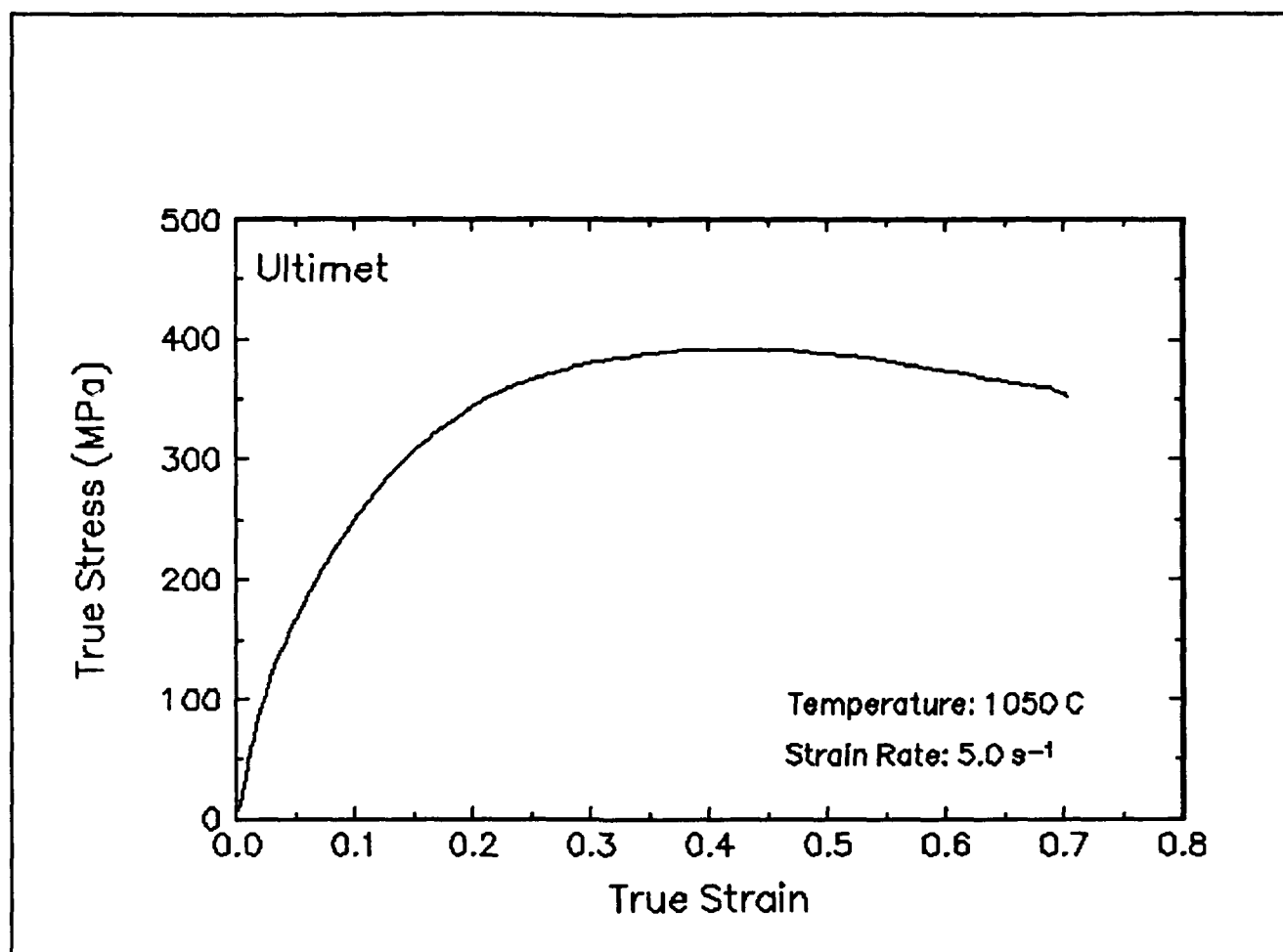


Figure 24. True stress-true strain curve and an optical micrograph from the center of the compressed sample cut through the compression axis, 1050 C and 5 s⁻¹.

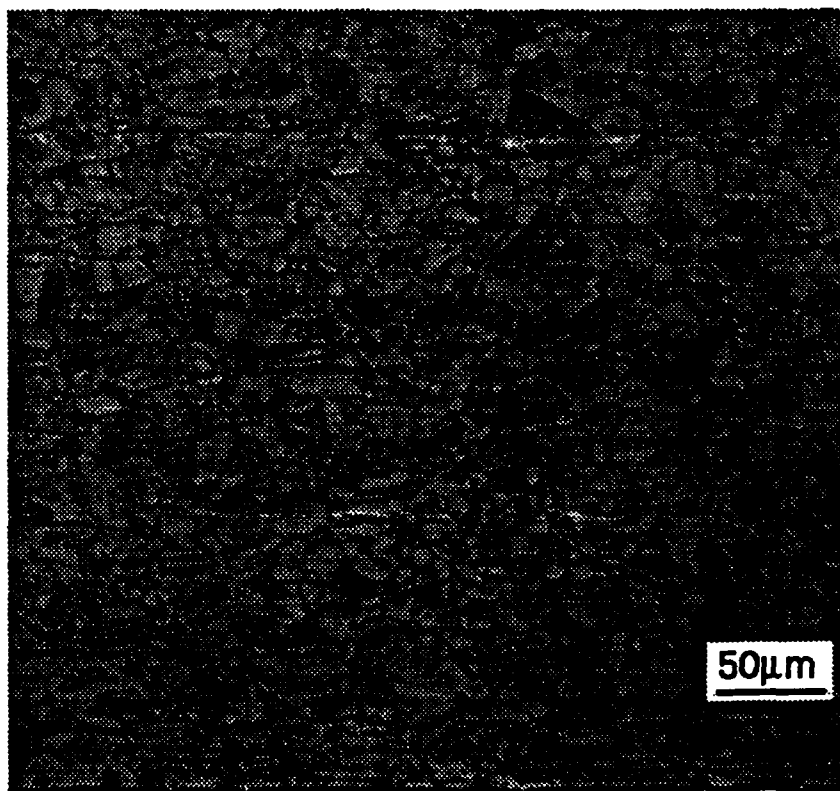
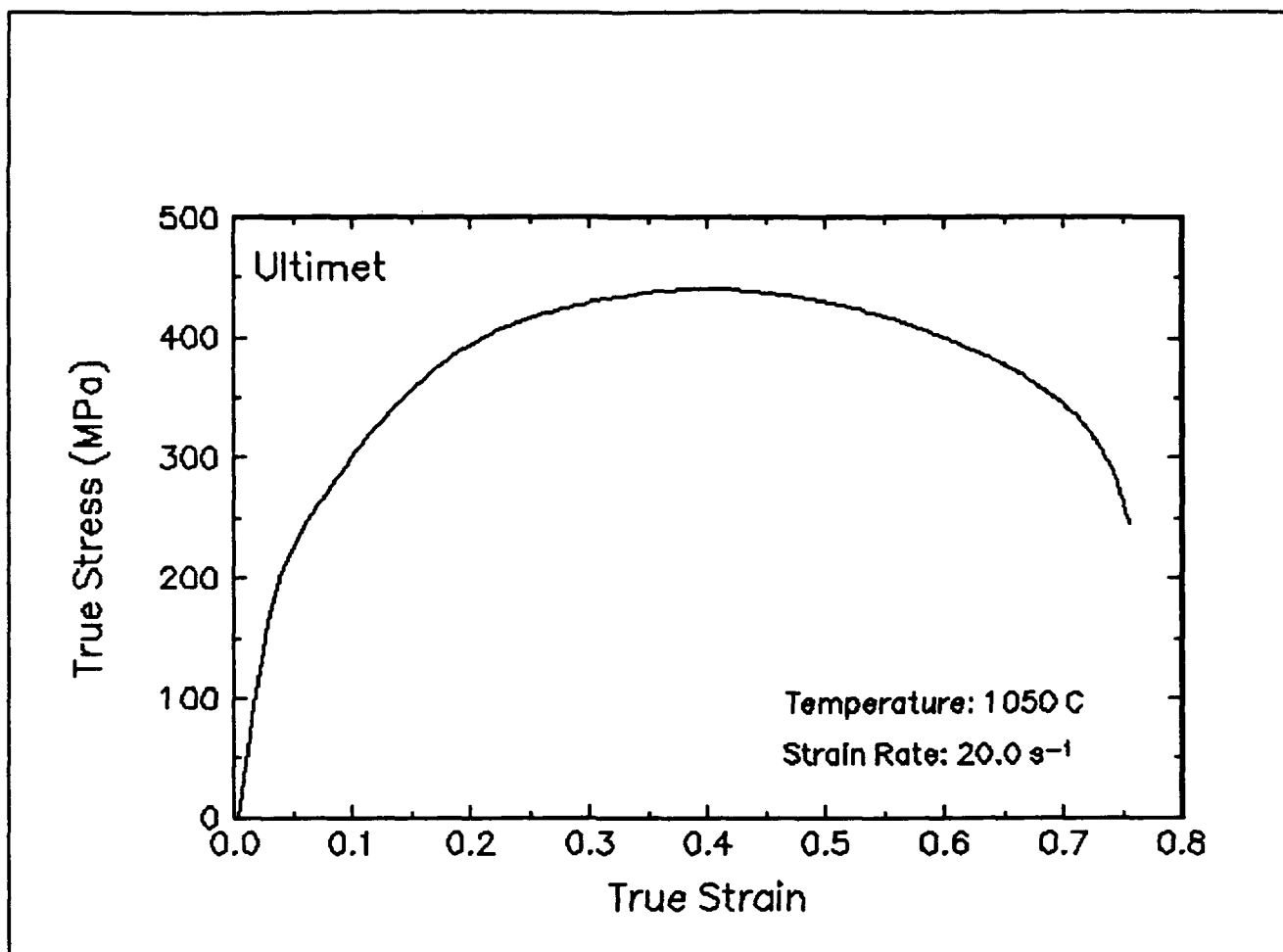


Figure 25. True stress-true strain curve and an optical micrograph from the center of the compressed sample cut through the compression axis, 1050 C and 20 s⁻¹.

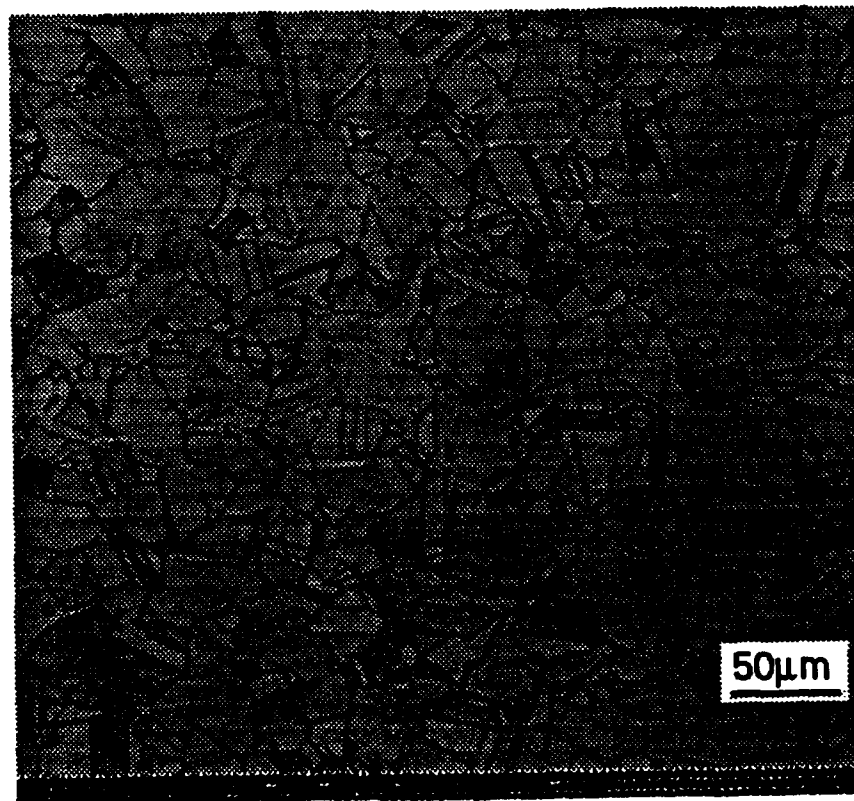
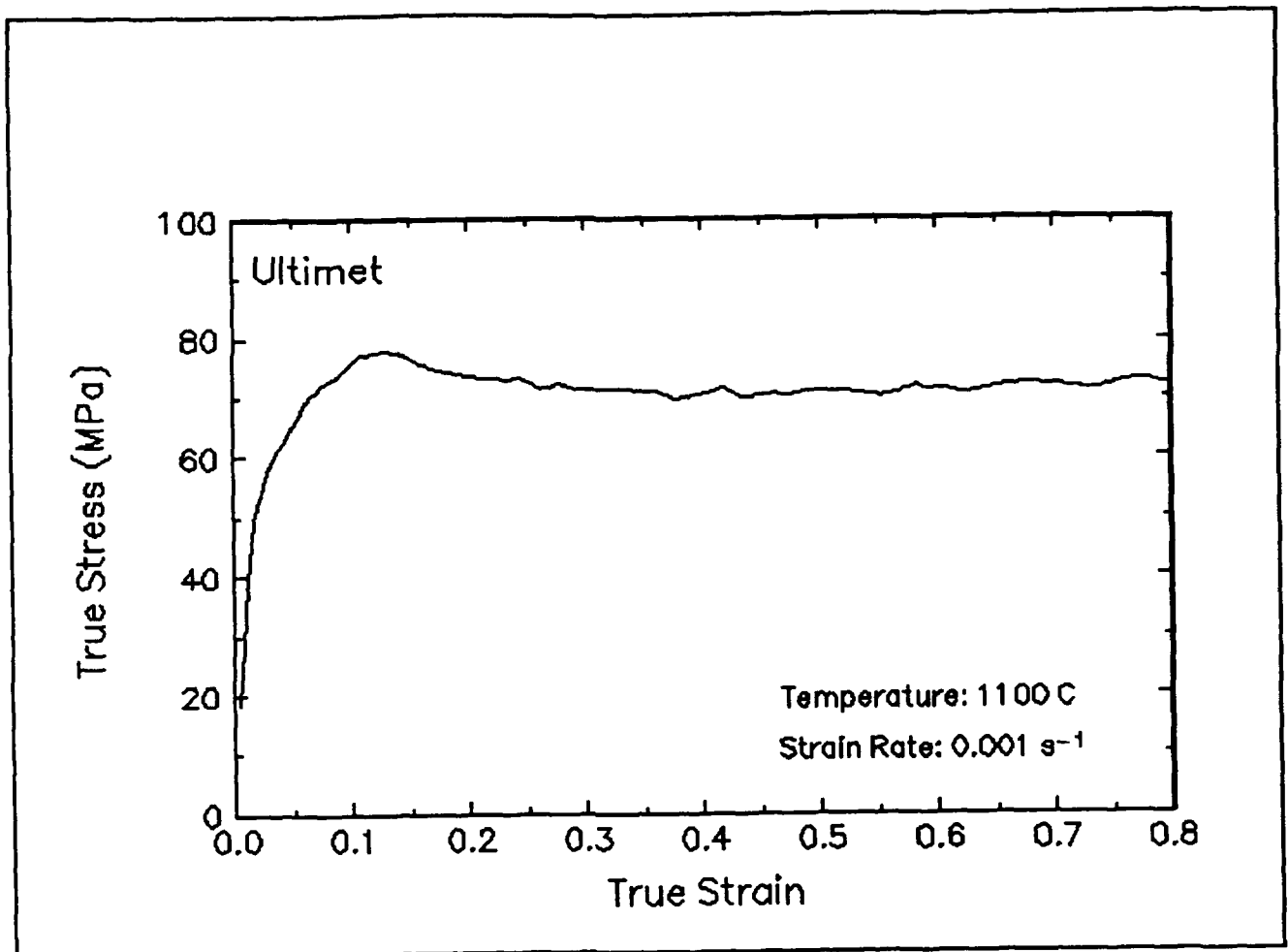


Figure 26. True stress-true strain curve and an optical micrograph from the center of the compressed sample cut through the compression axis, 1100 C and 0.001 s⁻¹.

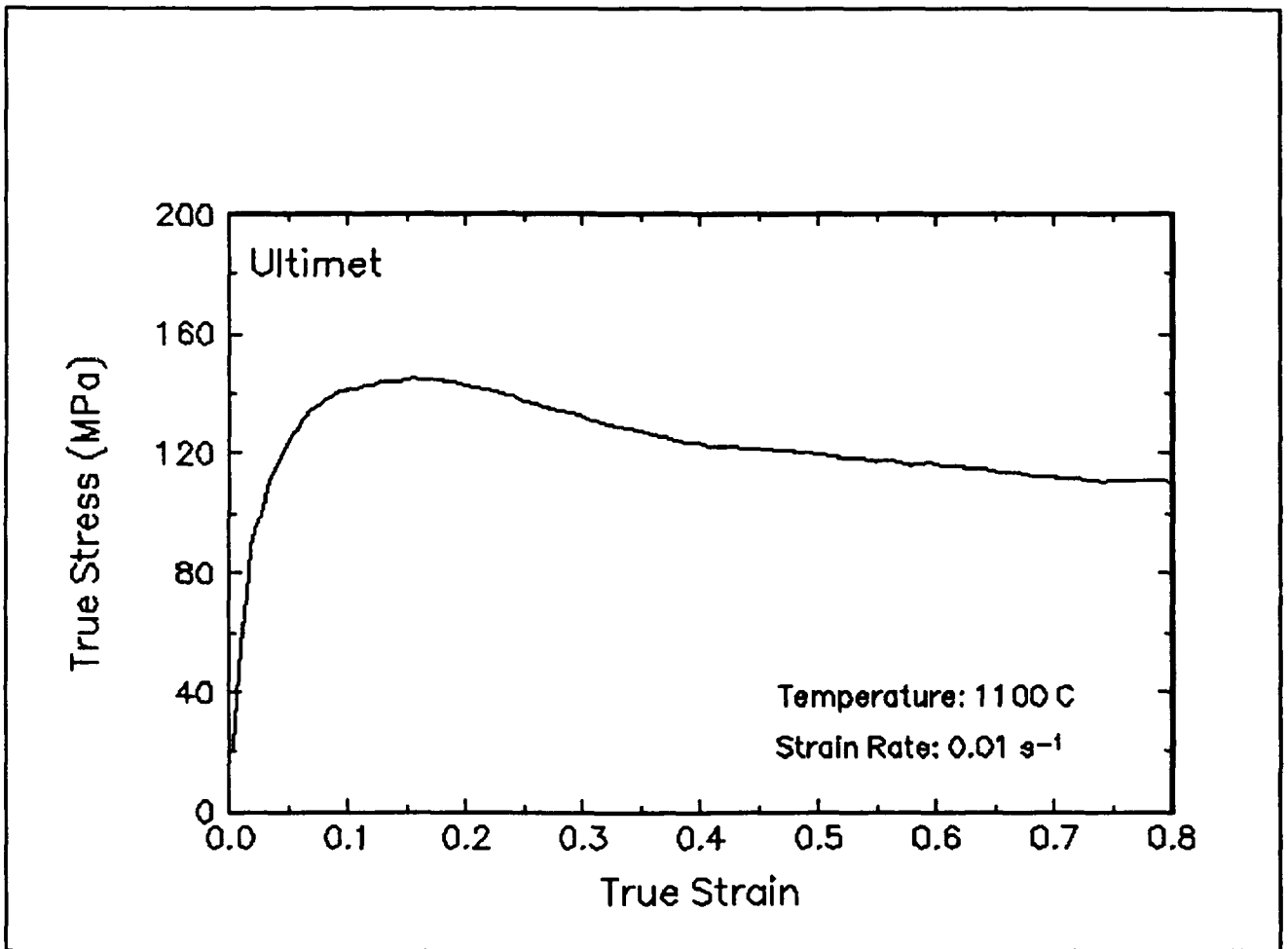


Figure 27. True stress-true strain curve, 1100 C and 0.01 s⁻¹.

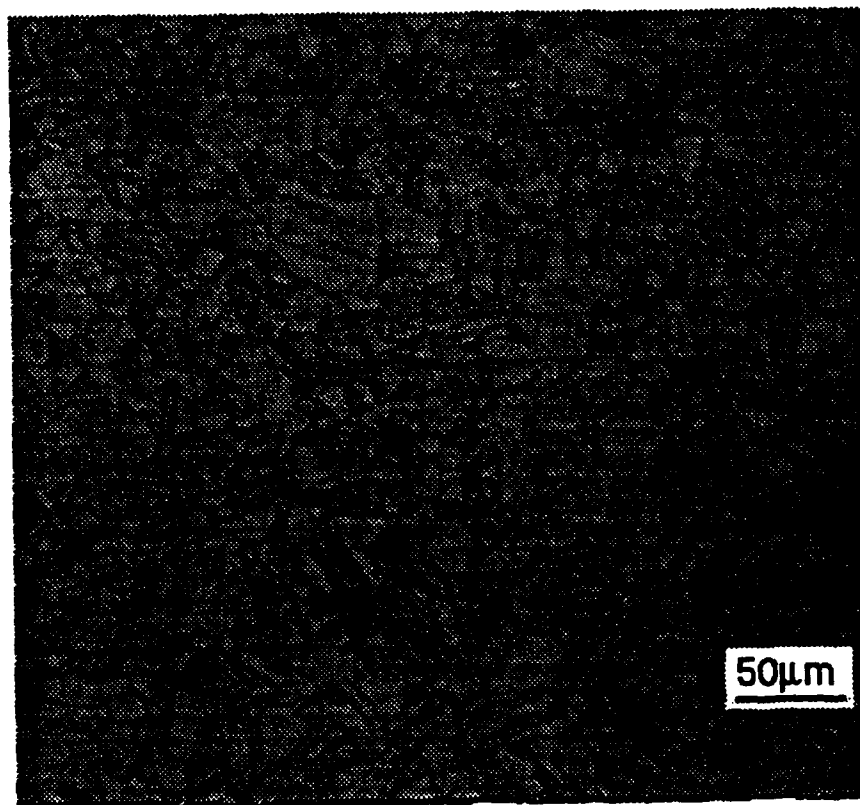
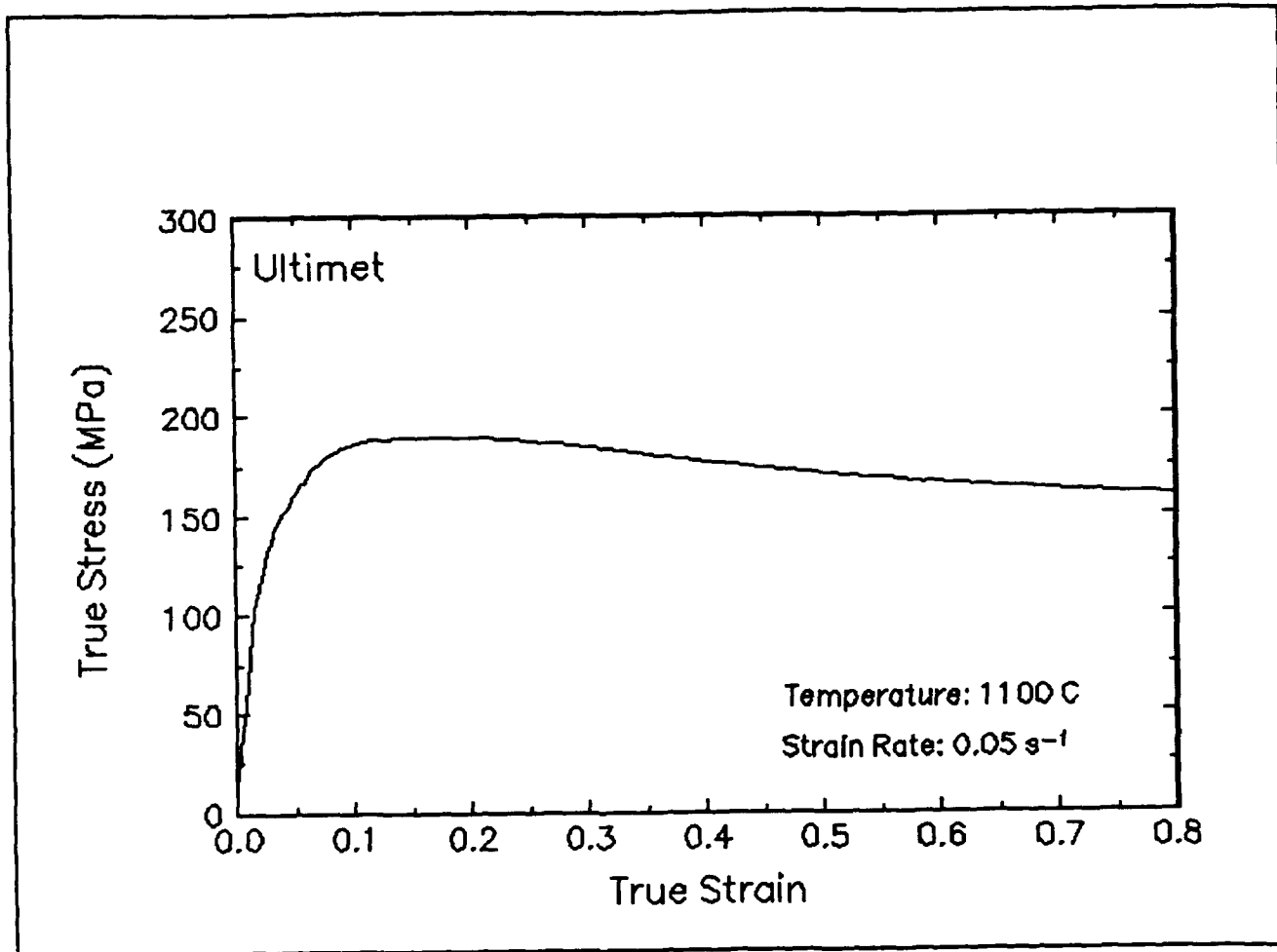


Figure 28. True stress-true strain curve and an optical micrograph from the center of the compressed sample cut through the compression axis, 1100 C and 0.05 s⁻¹.

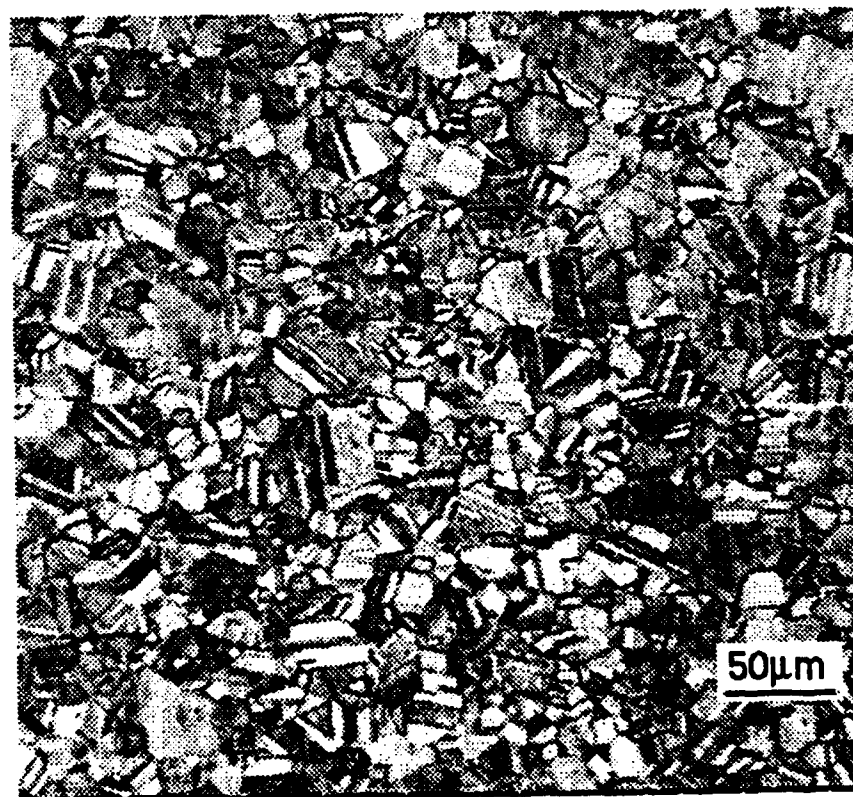
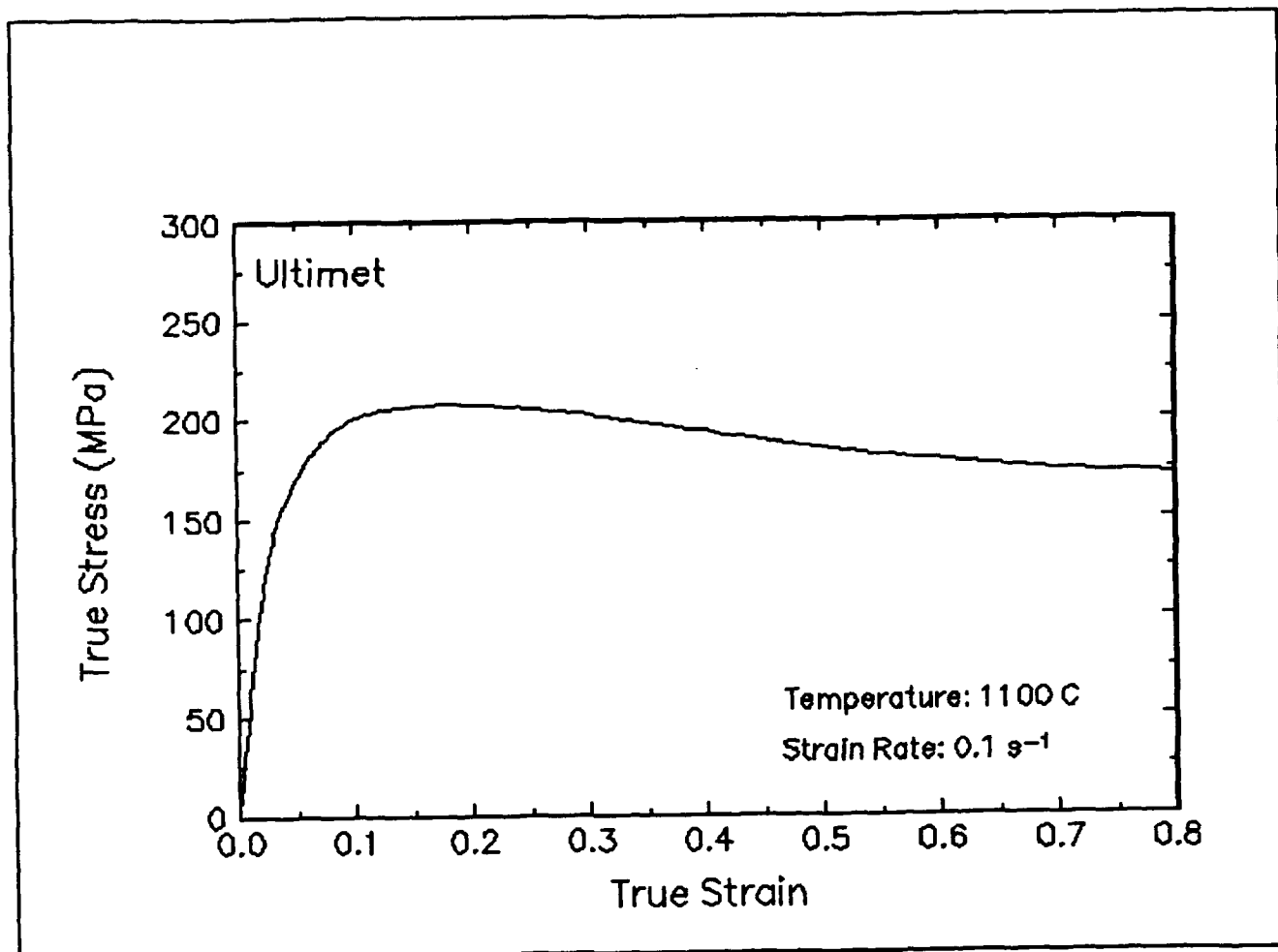


Figure 29. True stress-true strain curve and an optical micrograph from the center of the compressed sample cut through the compression axis, 1100 C and 0.1 s⁻¹.

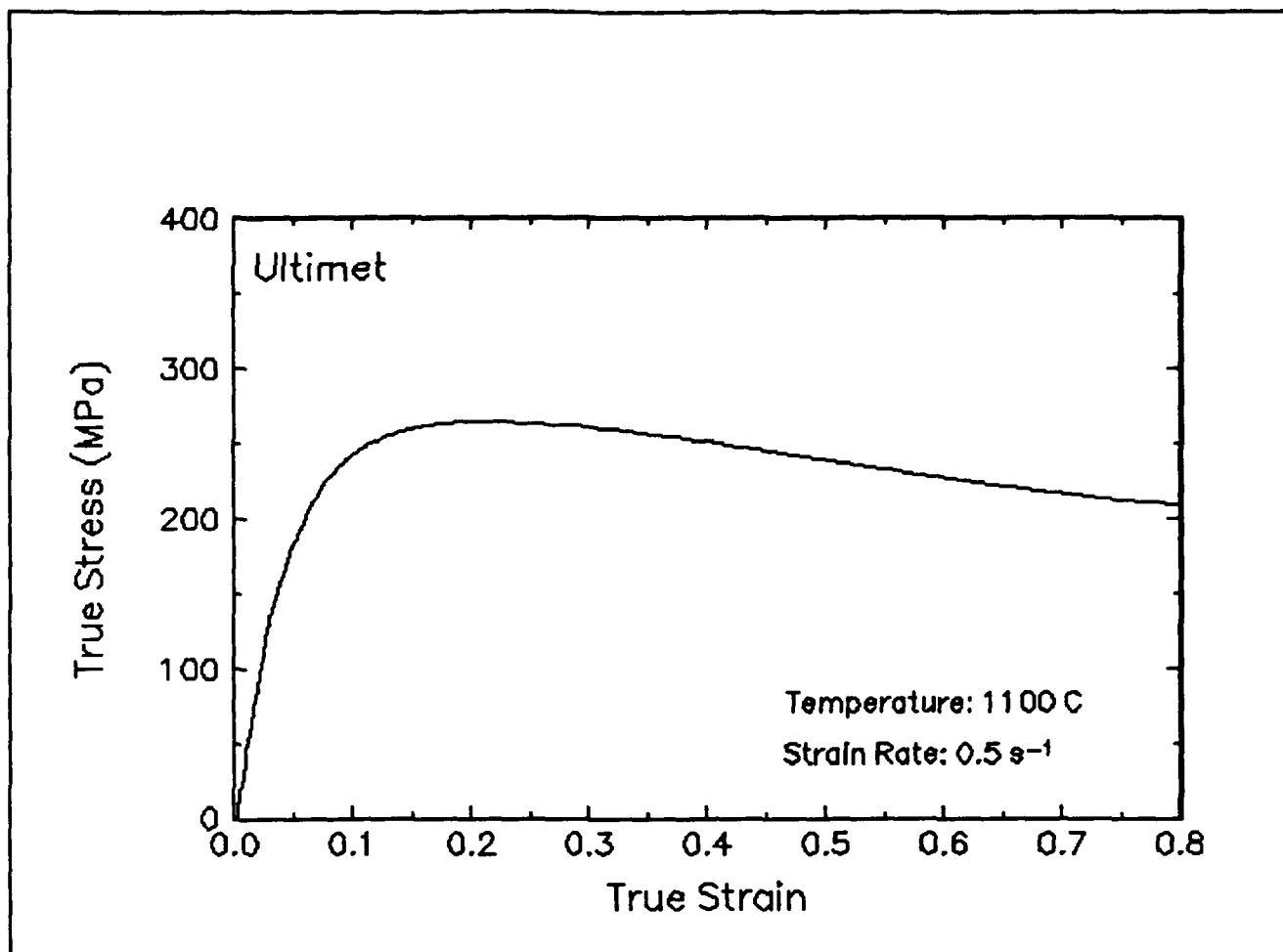


Figure 30. True stress-true strain curve and an optical micrograph from the center of the compressed sample cut through the compression axis, 1100 C and 0.5 s⁻¹.

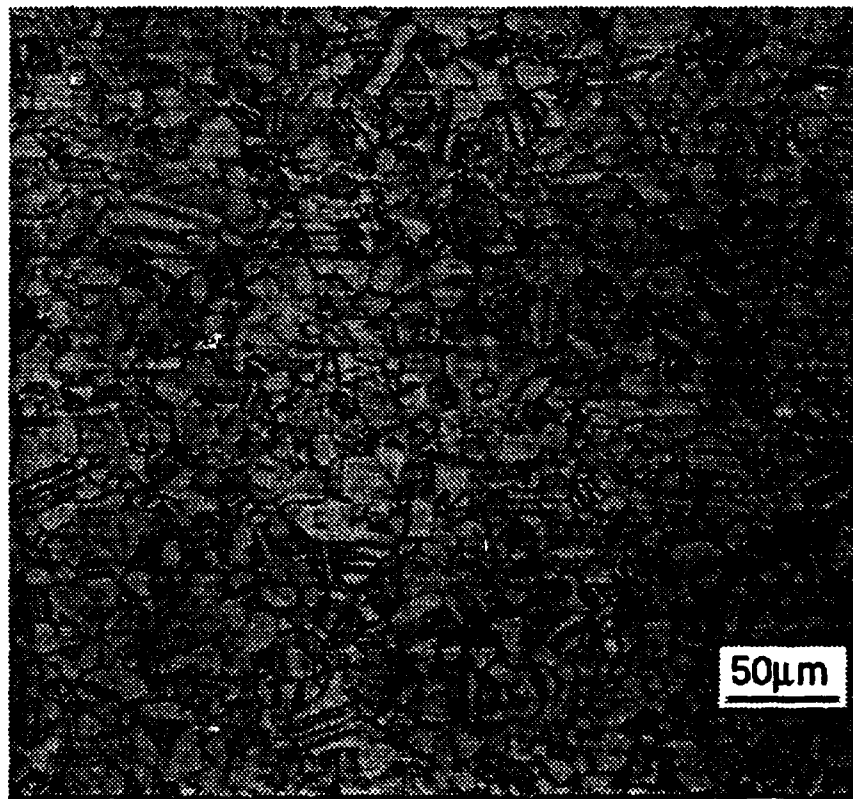
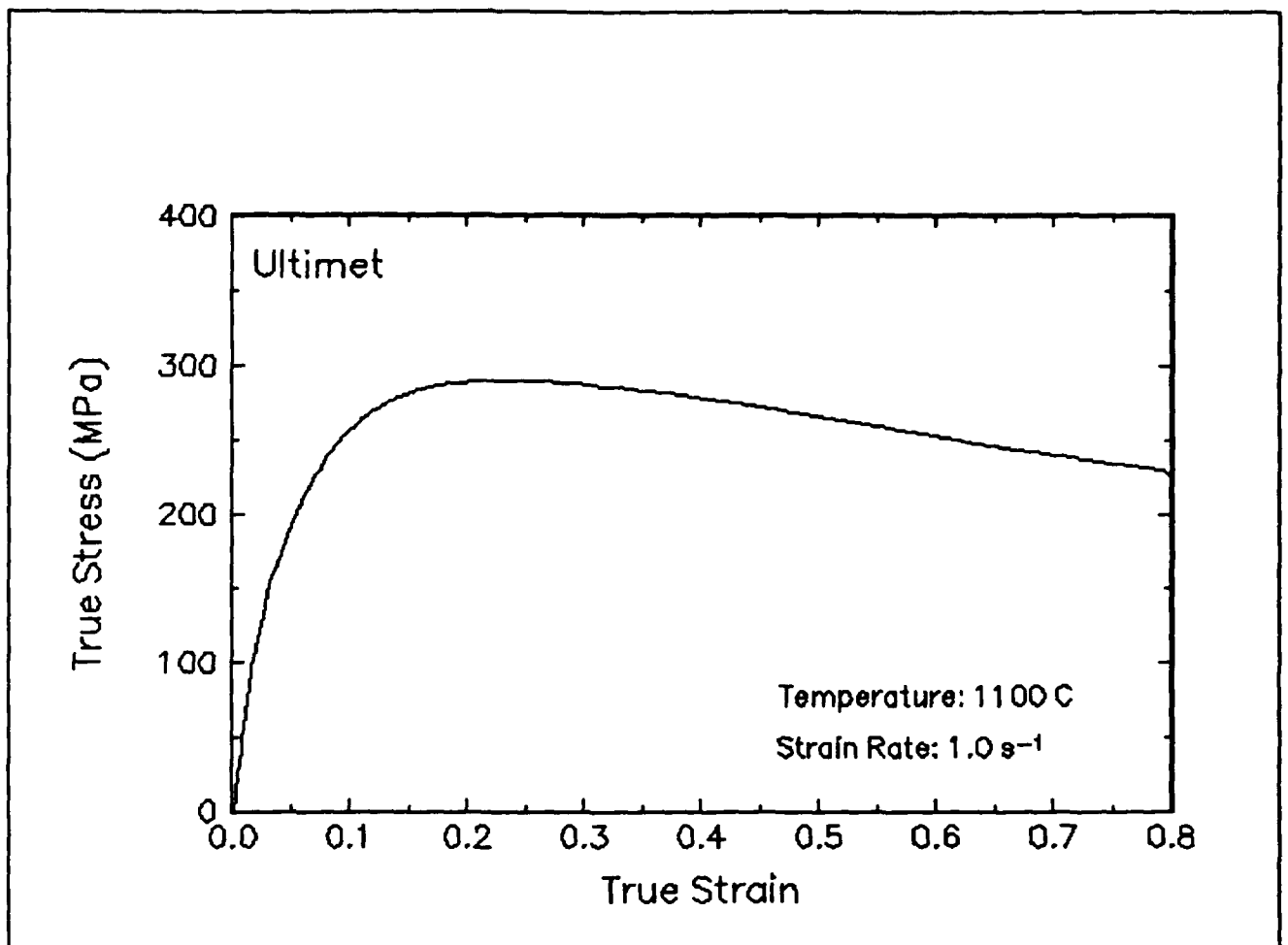


Figure 31. True stress-true strain curve and an optical micrograph from the center of the compressed sample cut through the compression axis, 1100 C and 1 s⁻¹.

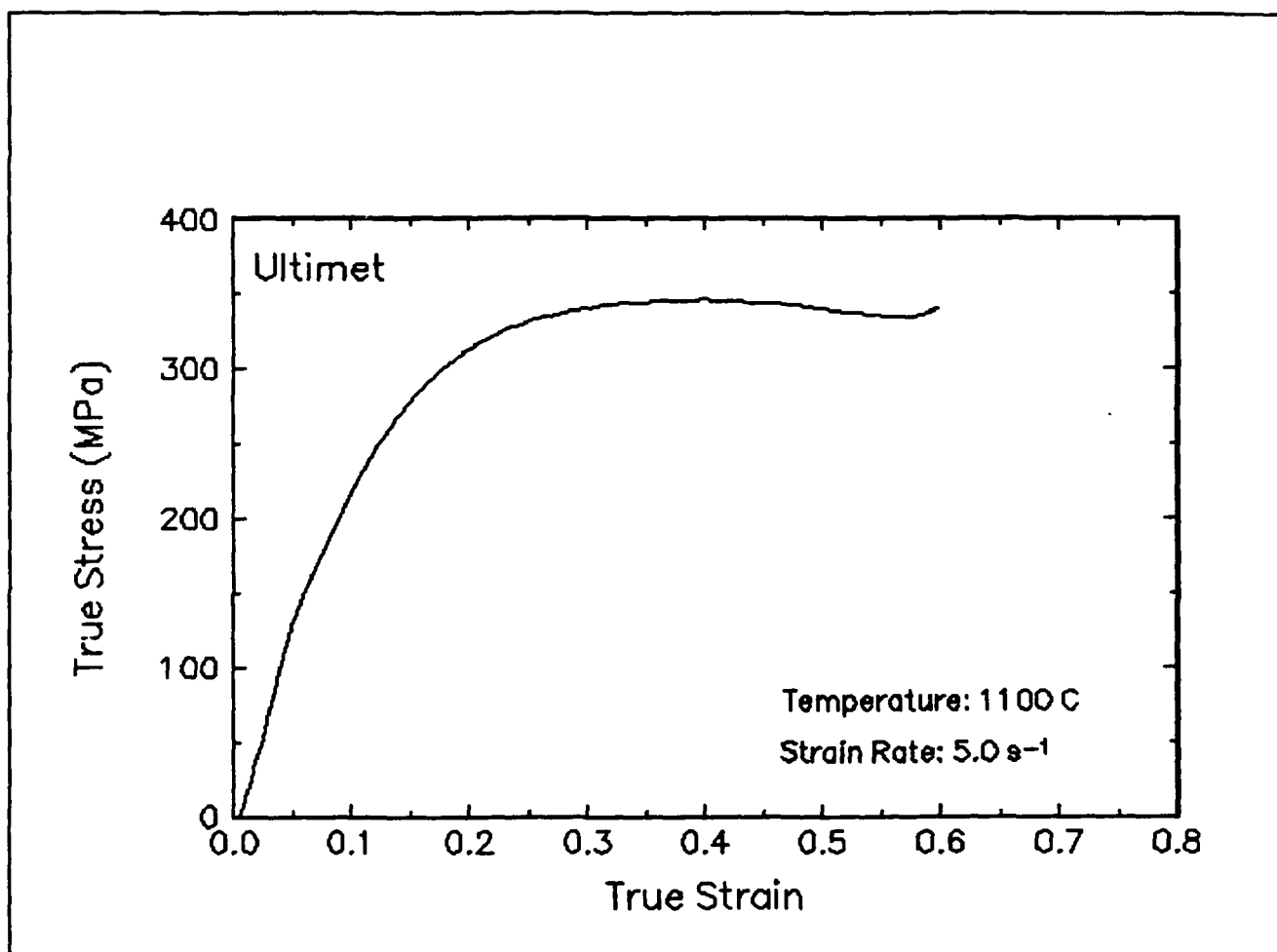


Figure 32. True stress-true strain curve, 1100 C and 5 s⁻¹.

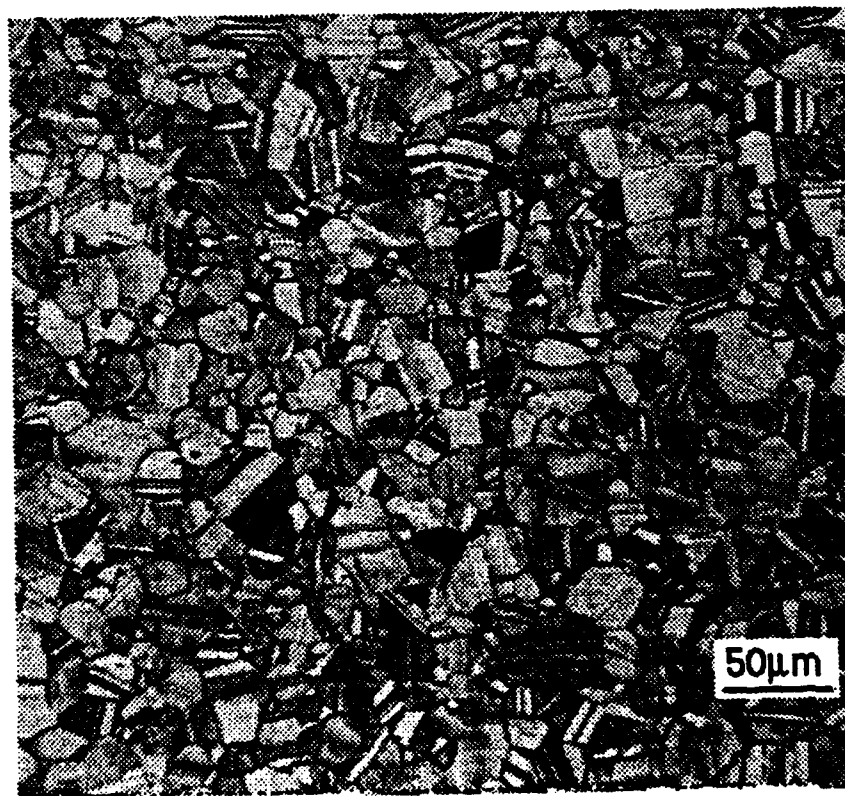
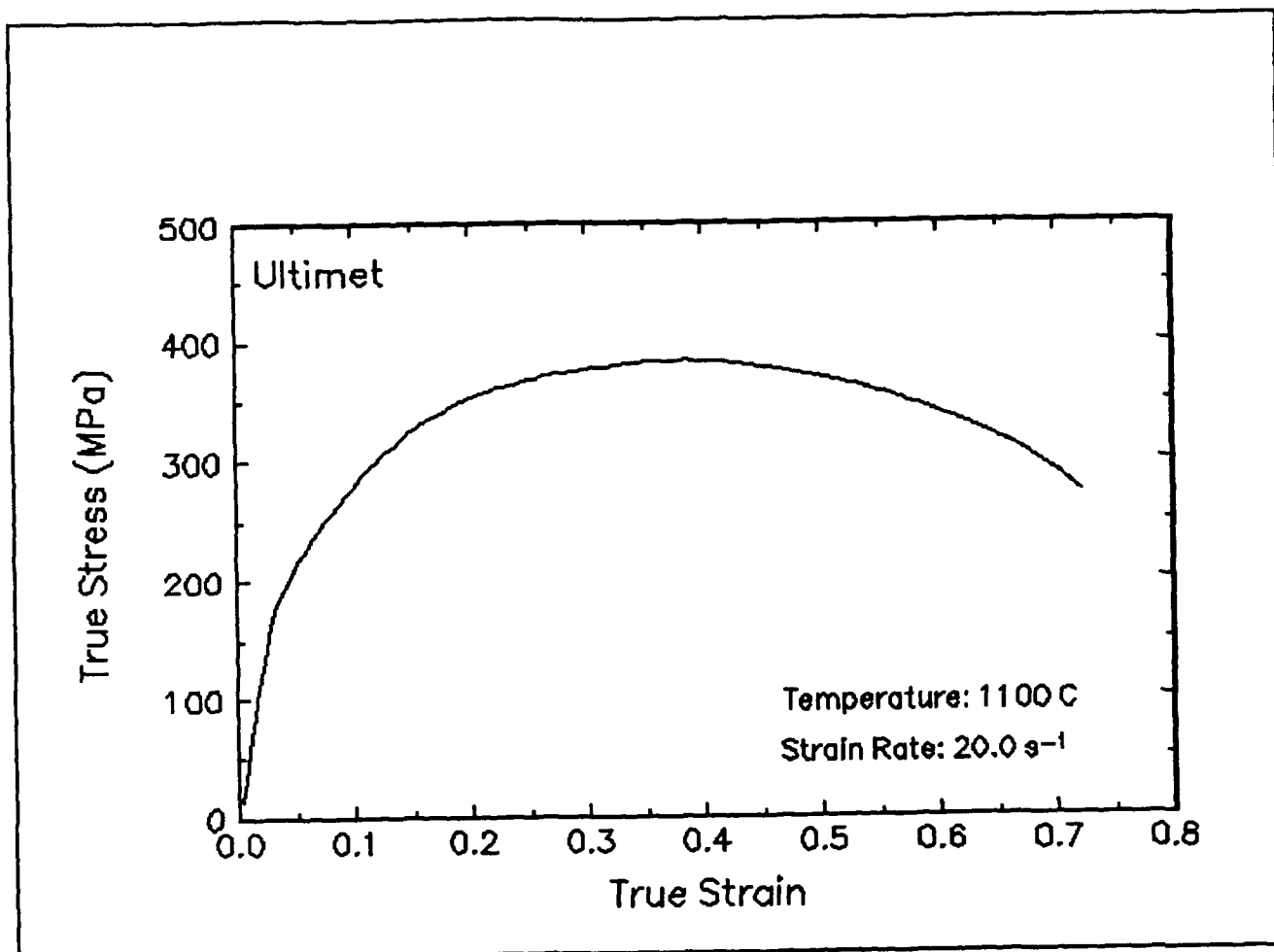


Figure 33. True stress-true strain curve and an optical micrograph from the center of the compressed sample cut through the compression axis, 1100 C and 20 s⁻¹.

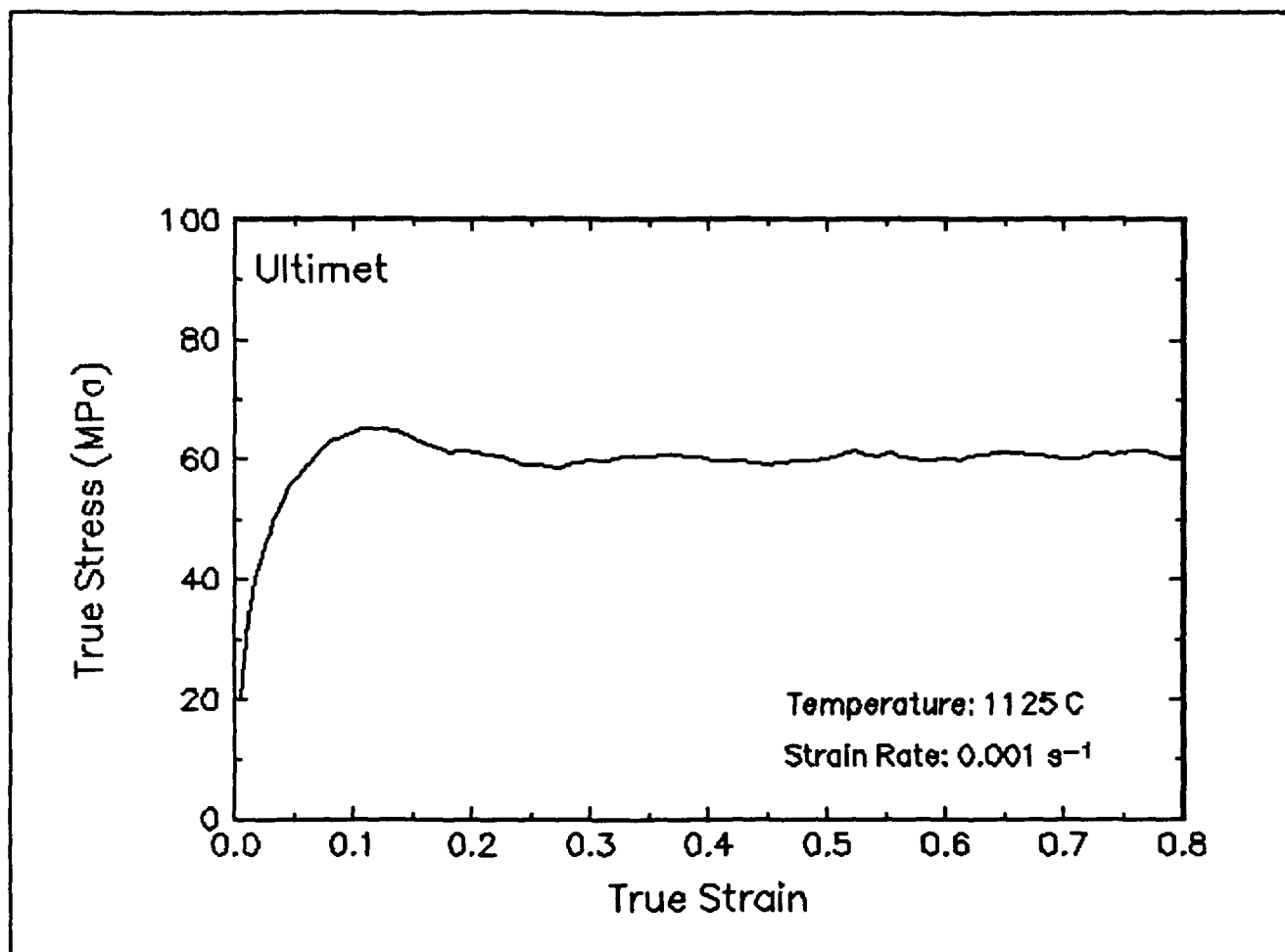


Figure 34. True stress-true strain curve and an optical micrograph from the center of the compressed sample cut through the compression axis, 1125 C and 0.001 s⁻¹.

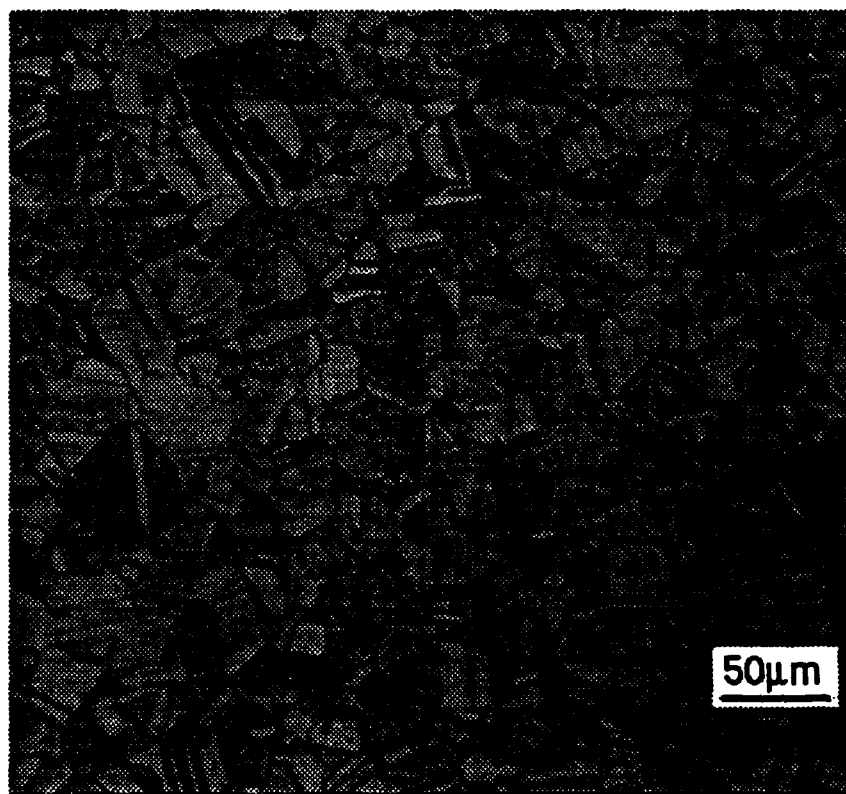
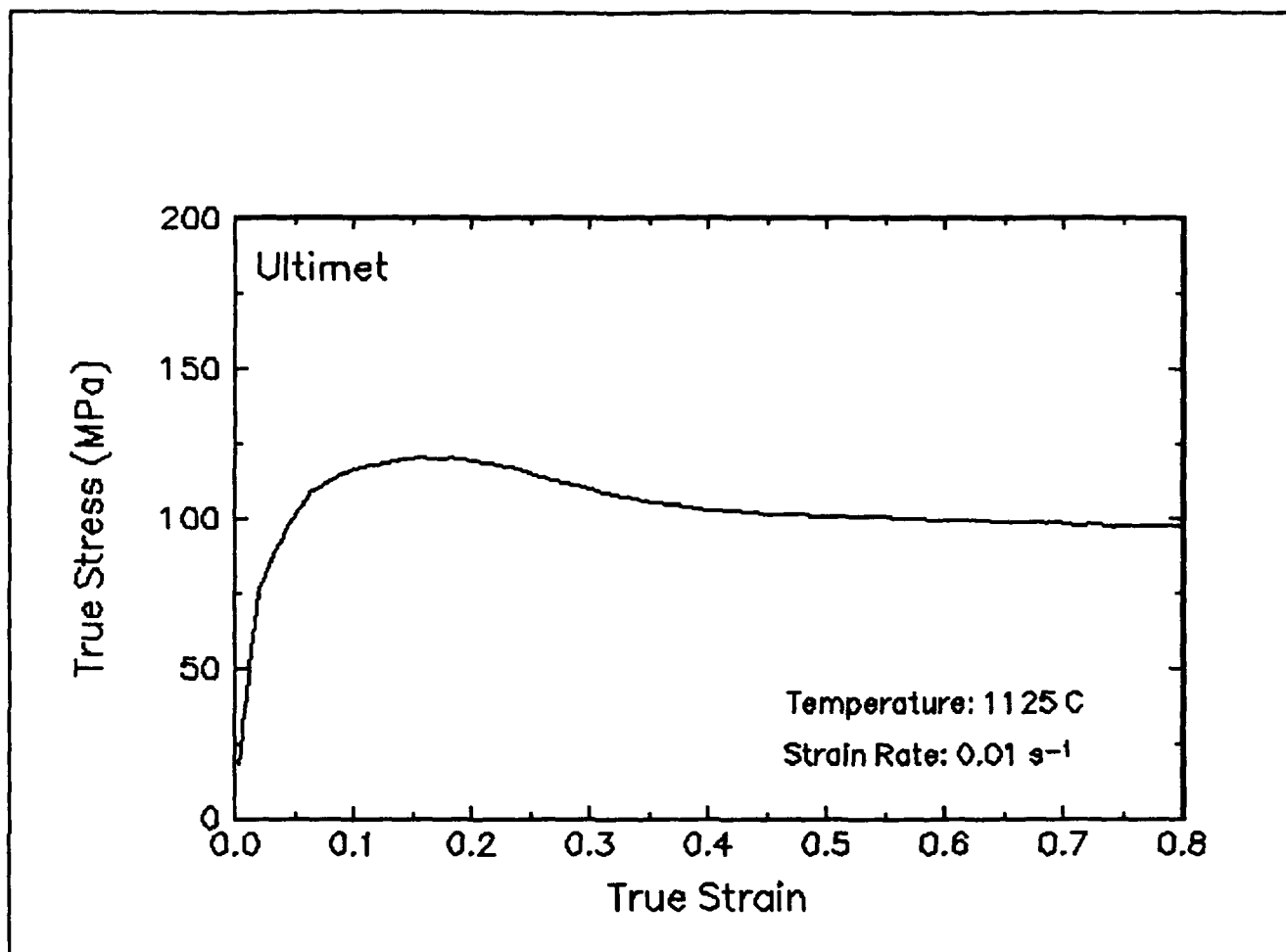


Figure 35. True stress-true strain curve and an optical micrograph from the center of the compressed sample cut through the compression axis, 1125 C and 0.01 s⁻¹.

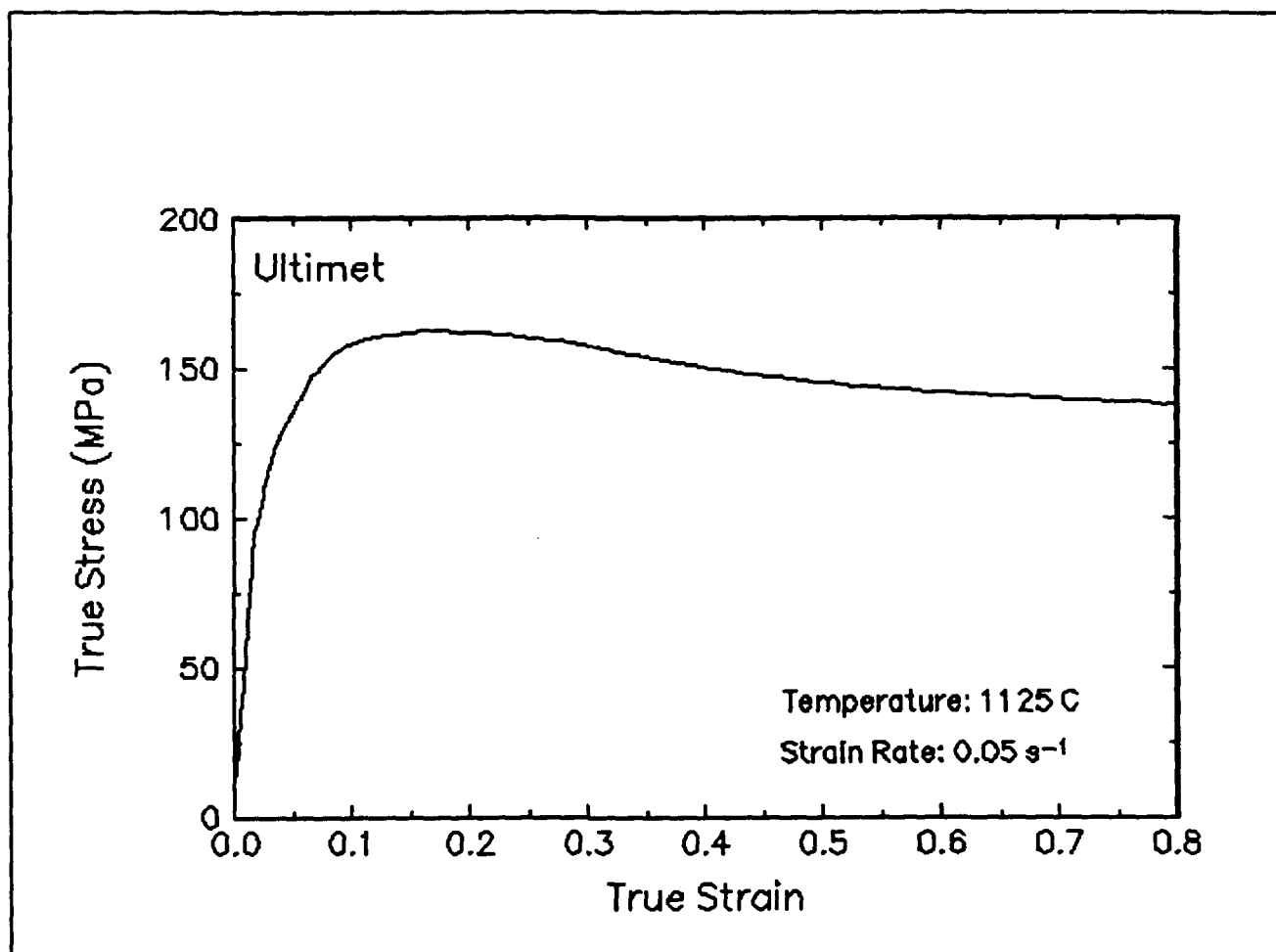


Figure 36. True stress-true strain curve, 1125 C and 0.05 s⁻¹.

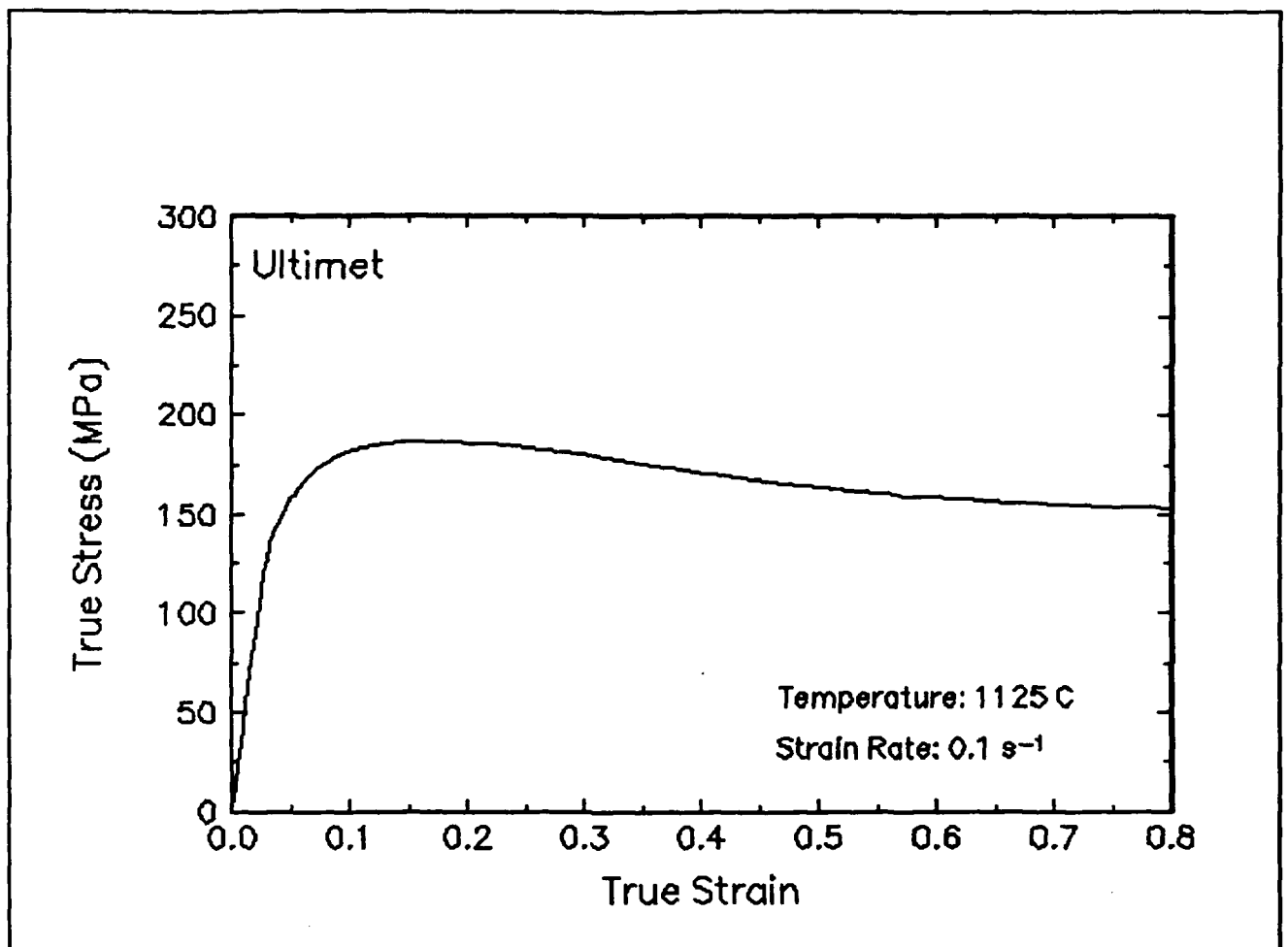


Figure 37. True stress-true strain curve and an optical micrograph from the center of the compressed sample cut through the compression axis, 1125 C and 0.1 s⁻¹.

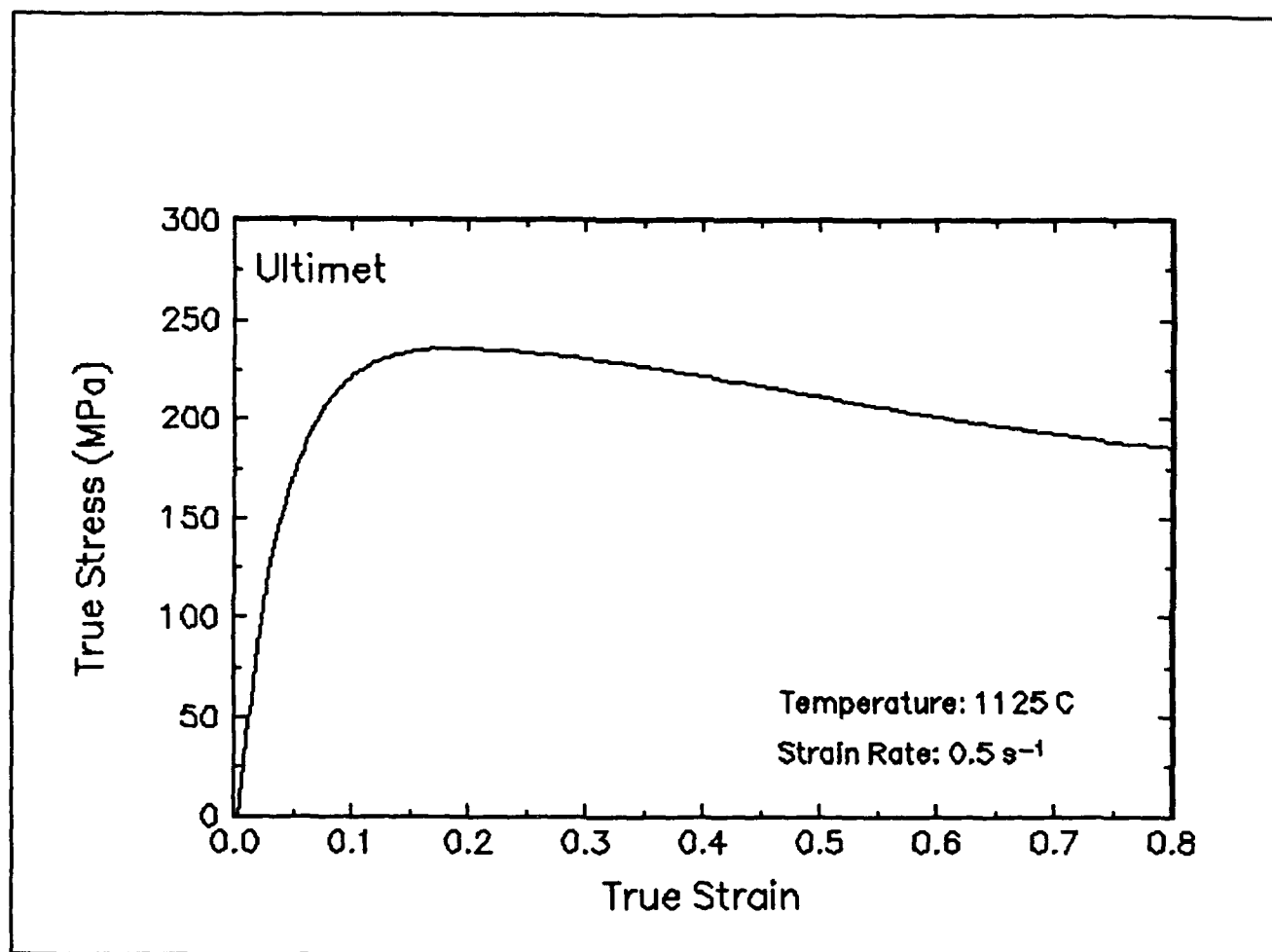


Figure 38. True stress-true strain curve, 1125 C and 0.5 s⁻¹.

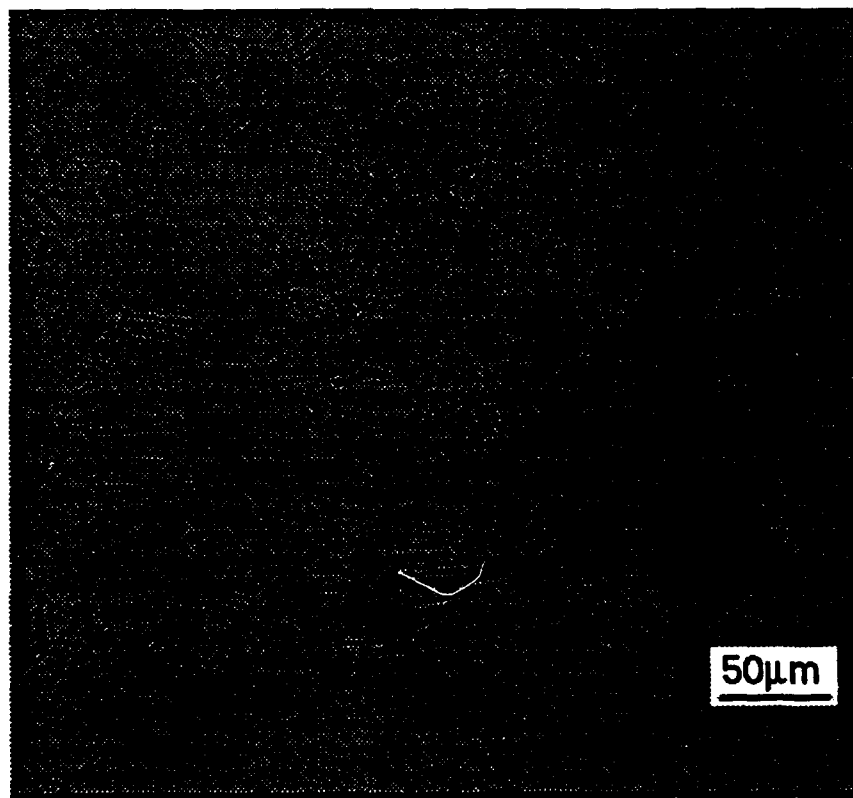
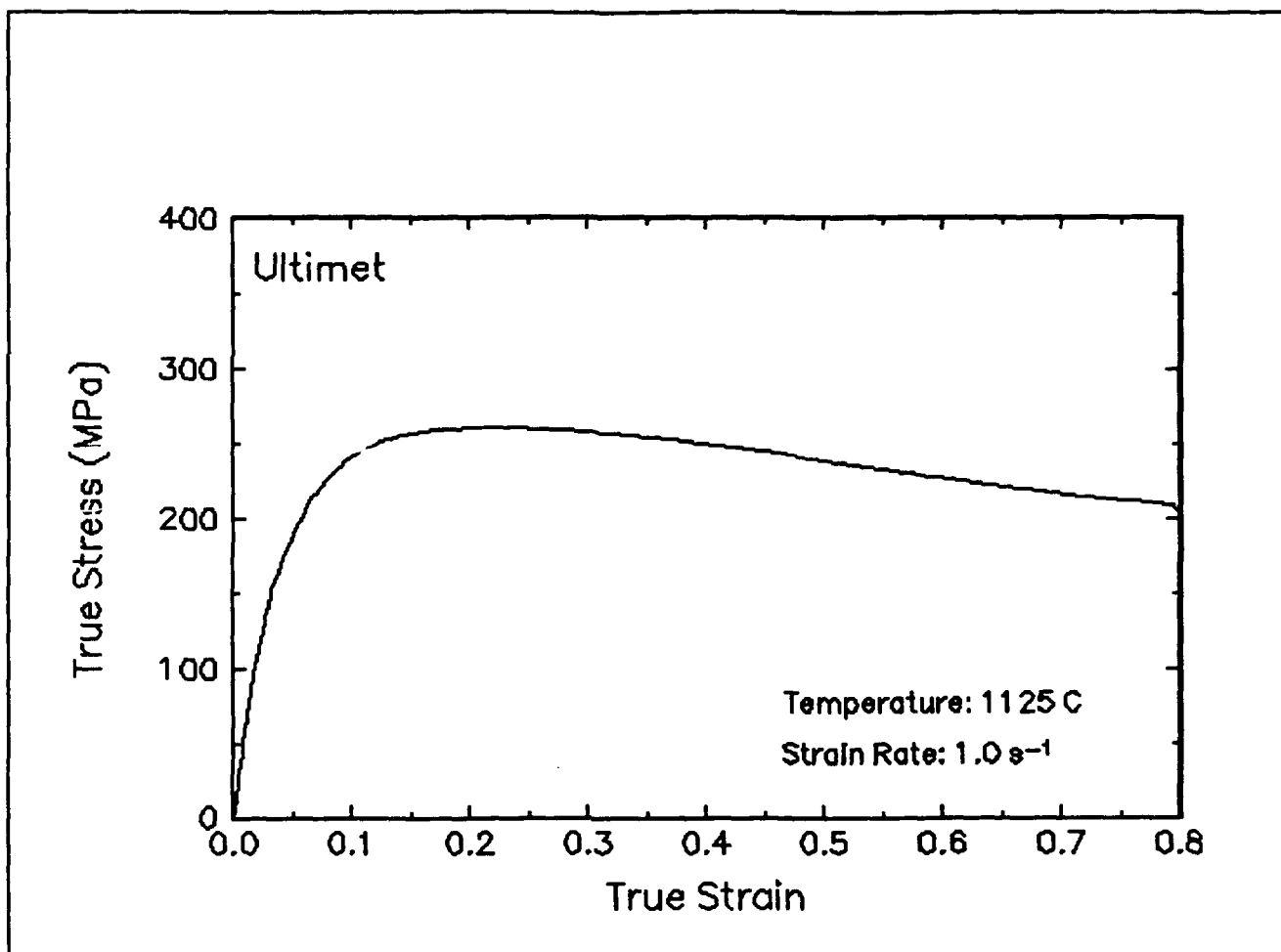


Figure 39. True stress-true strain curve and an optical micrograph from the center of the compressed sample cut through the compression axis, 1125 C and 1 s⁻¹.

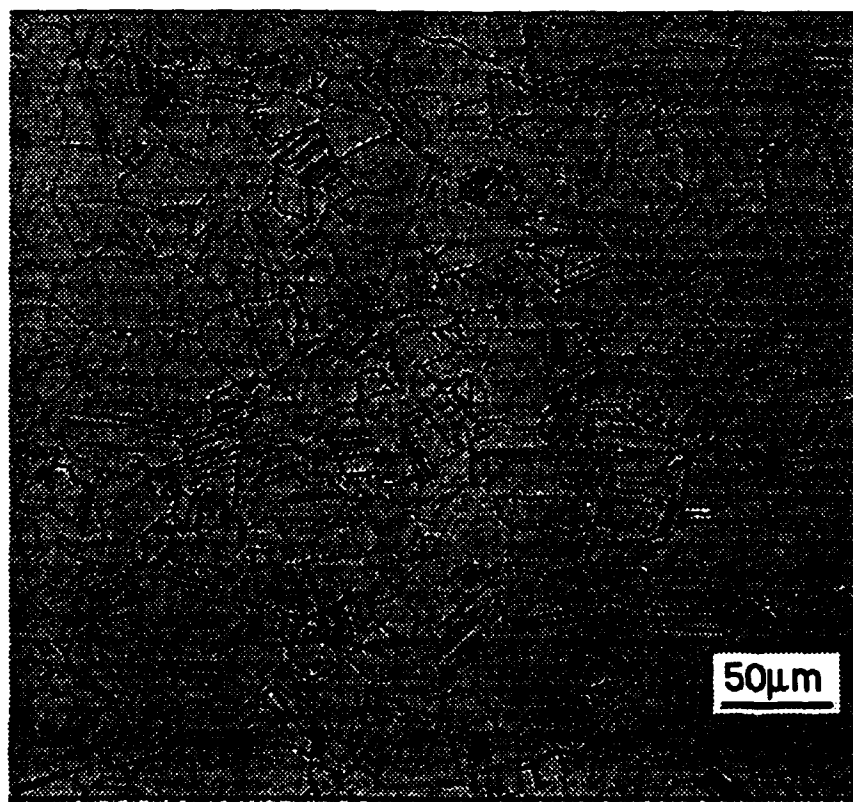
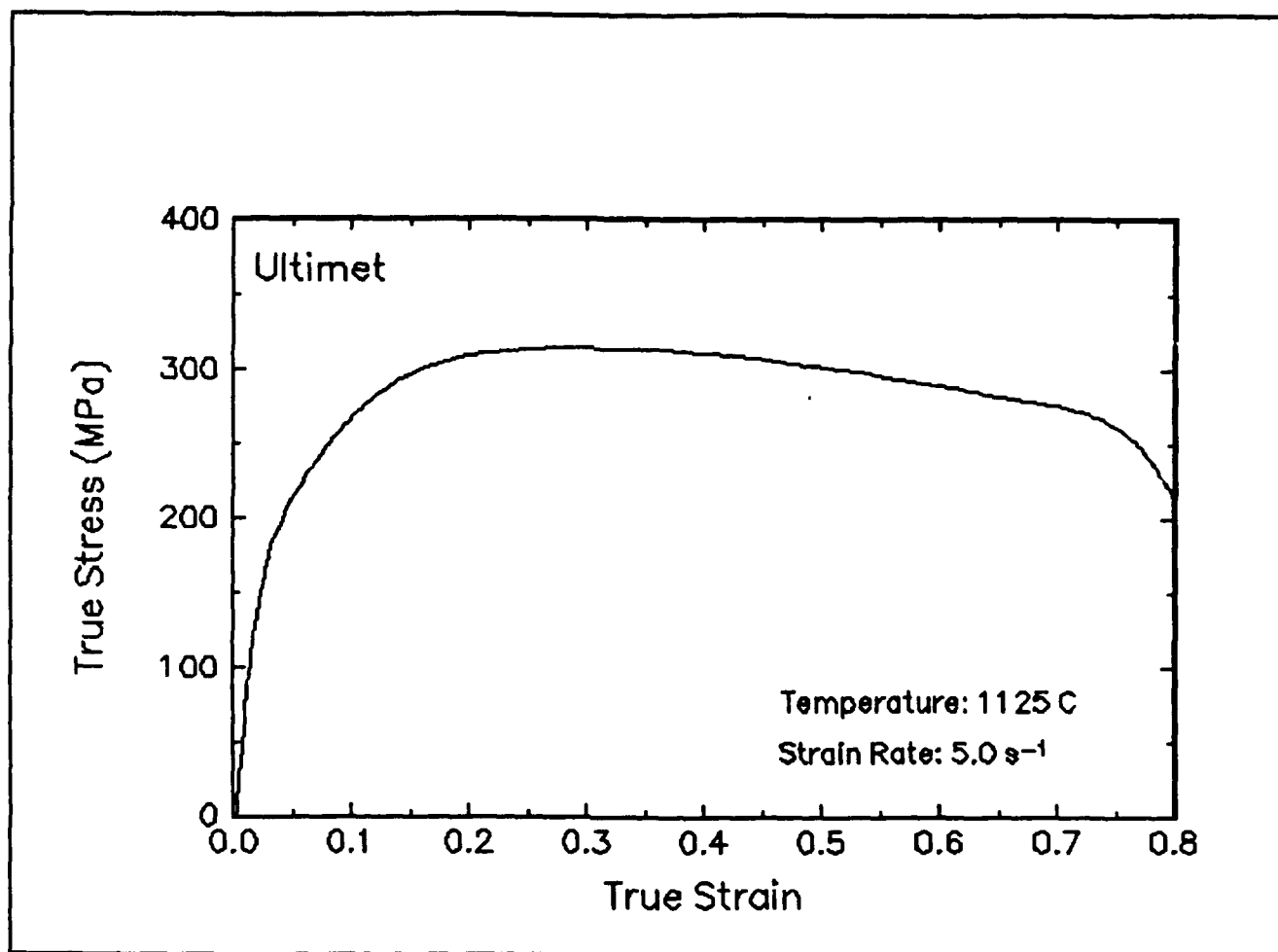


Figure 40. True stress-true strain curve and an optical micrograph from the center of the compressed sample cut through the compression axis, 1125 C and 5 s⁻¹.

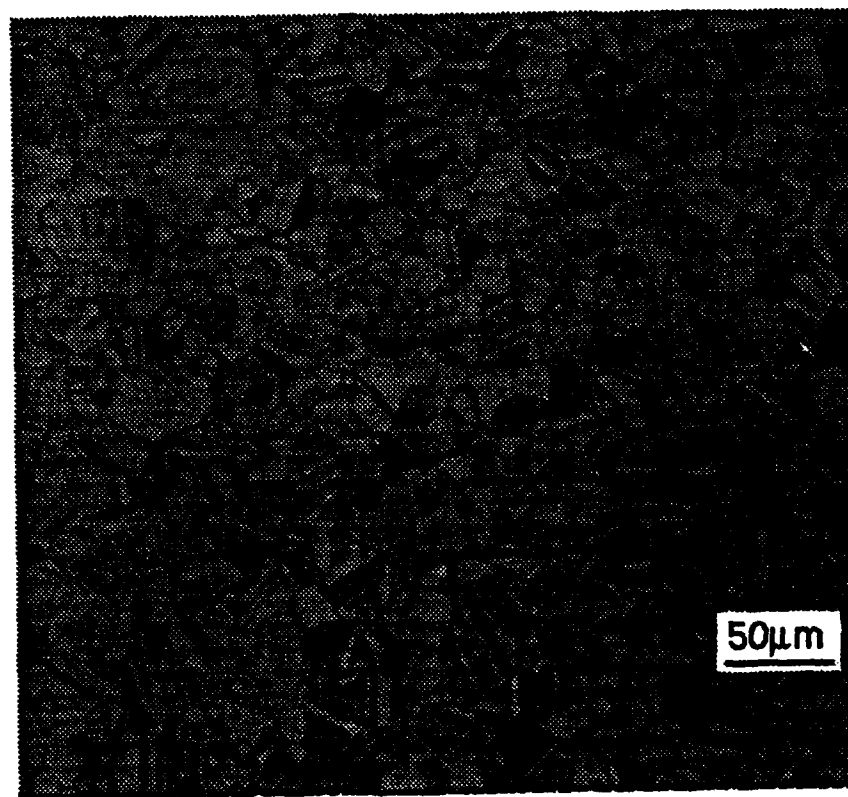
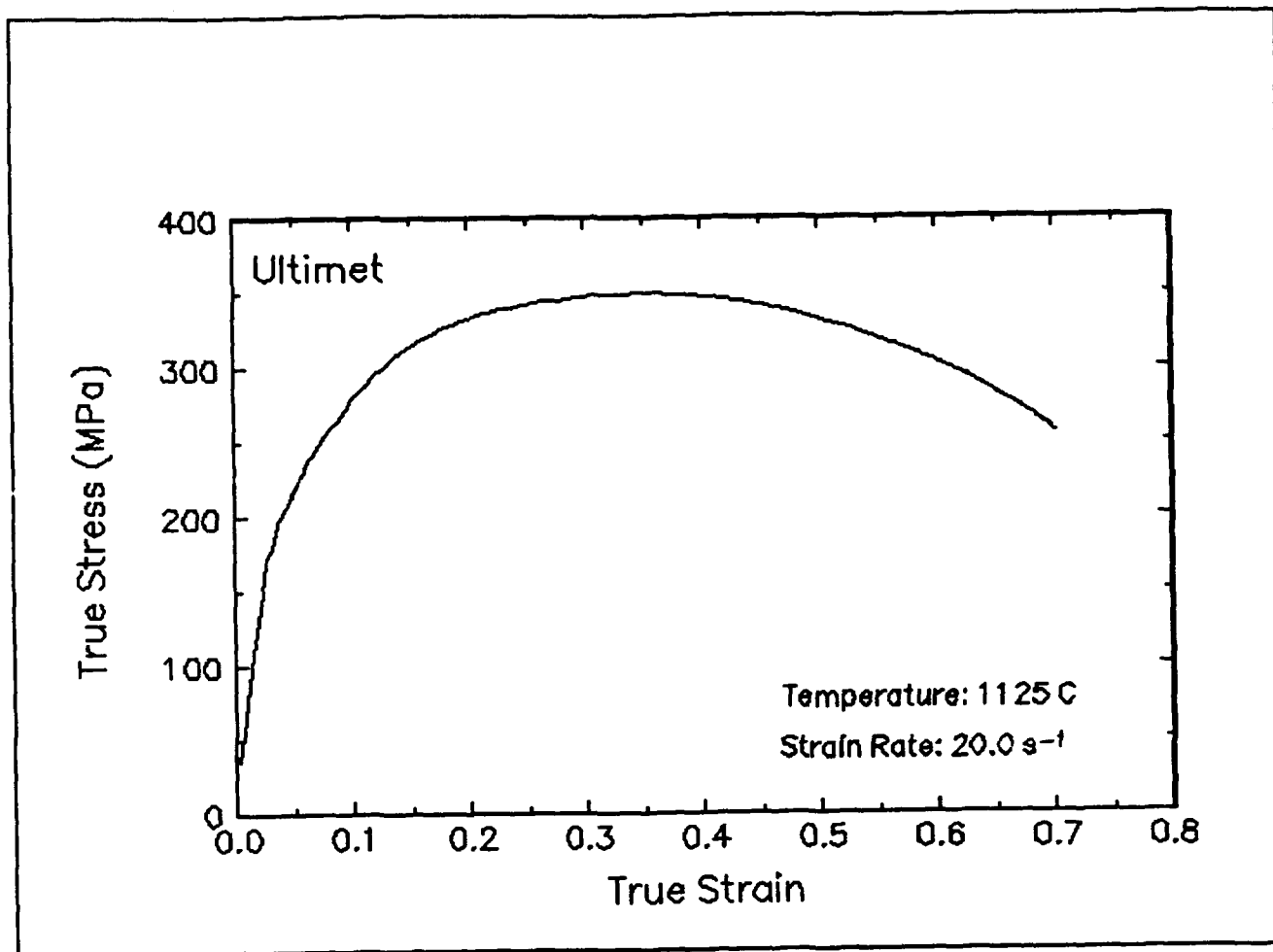


Figure 41. True stress-true strain curve and an optical micrograph from the center of the compressed sample cut through the compression axis, 1125 C and 20 s⁻¹.

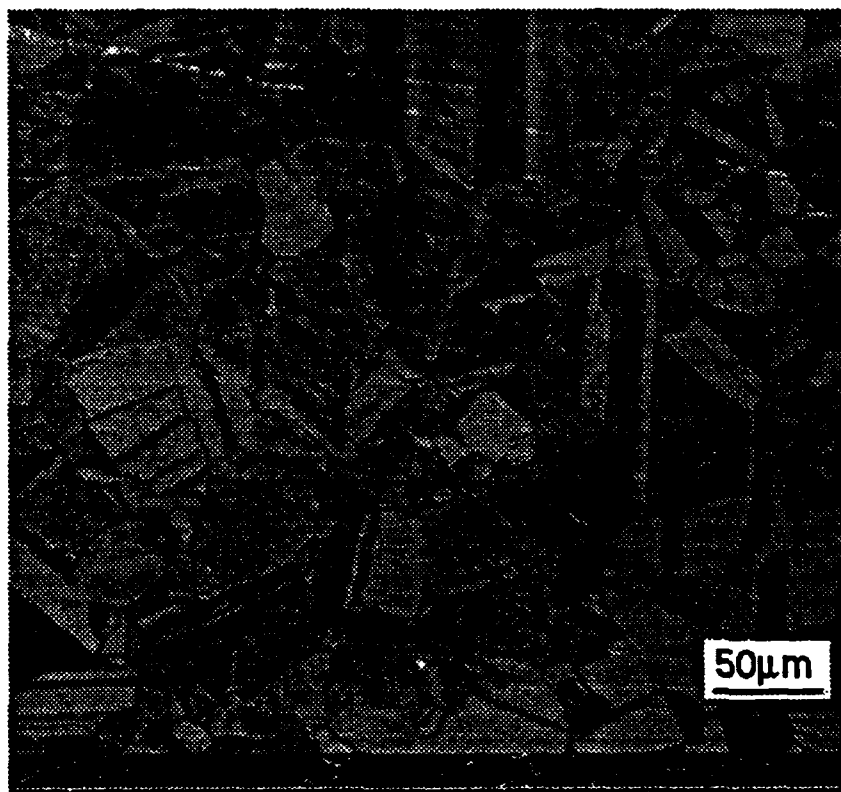
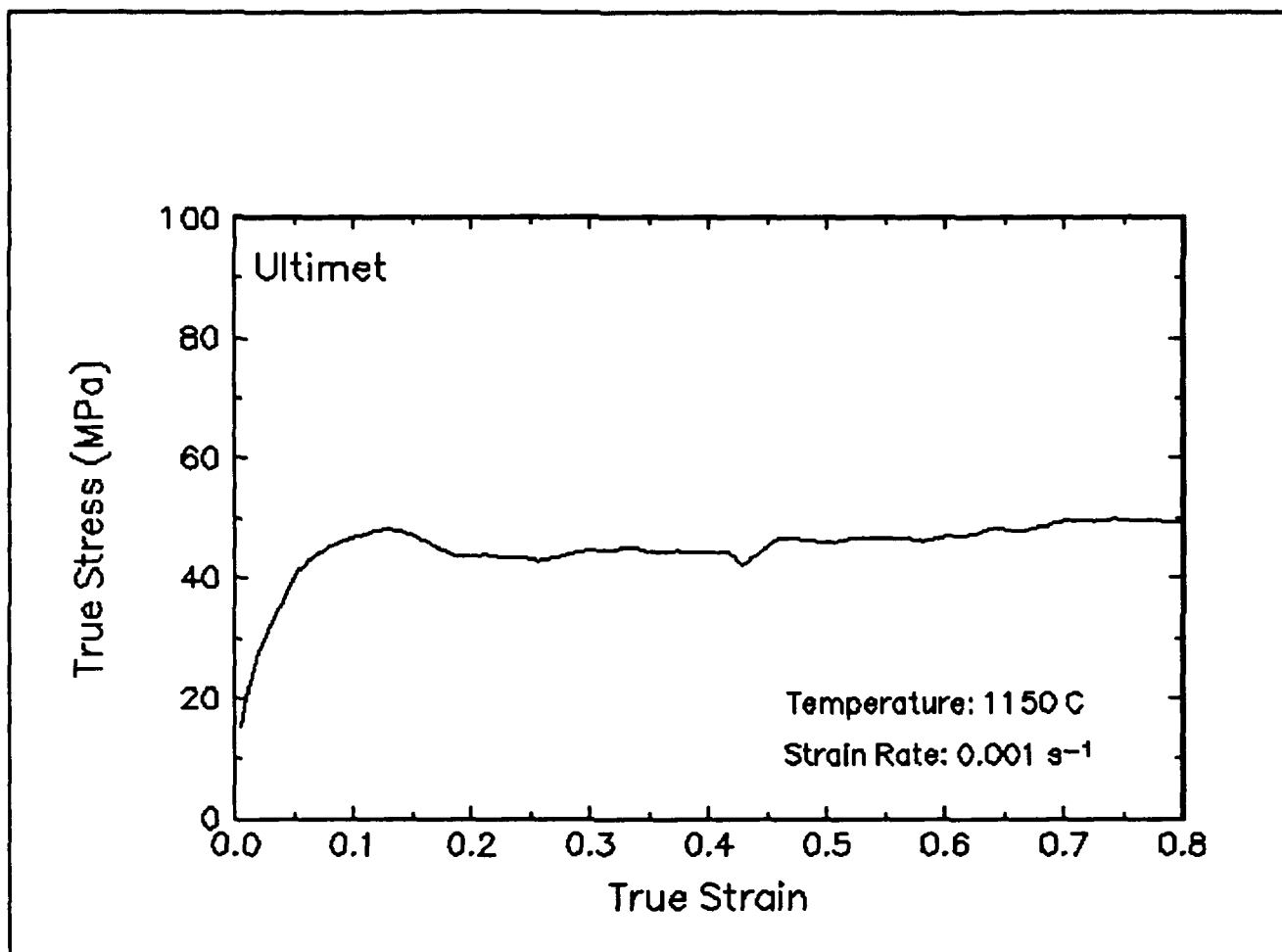


Figure 42. True stress-true strain curve and an optical micrograph from the center of the compressed sample cut through the compression axis, 1150 C and 0.001 s⁻¹.

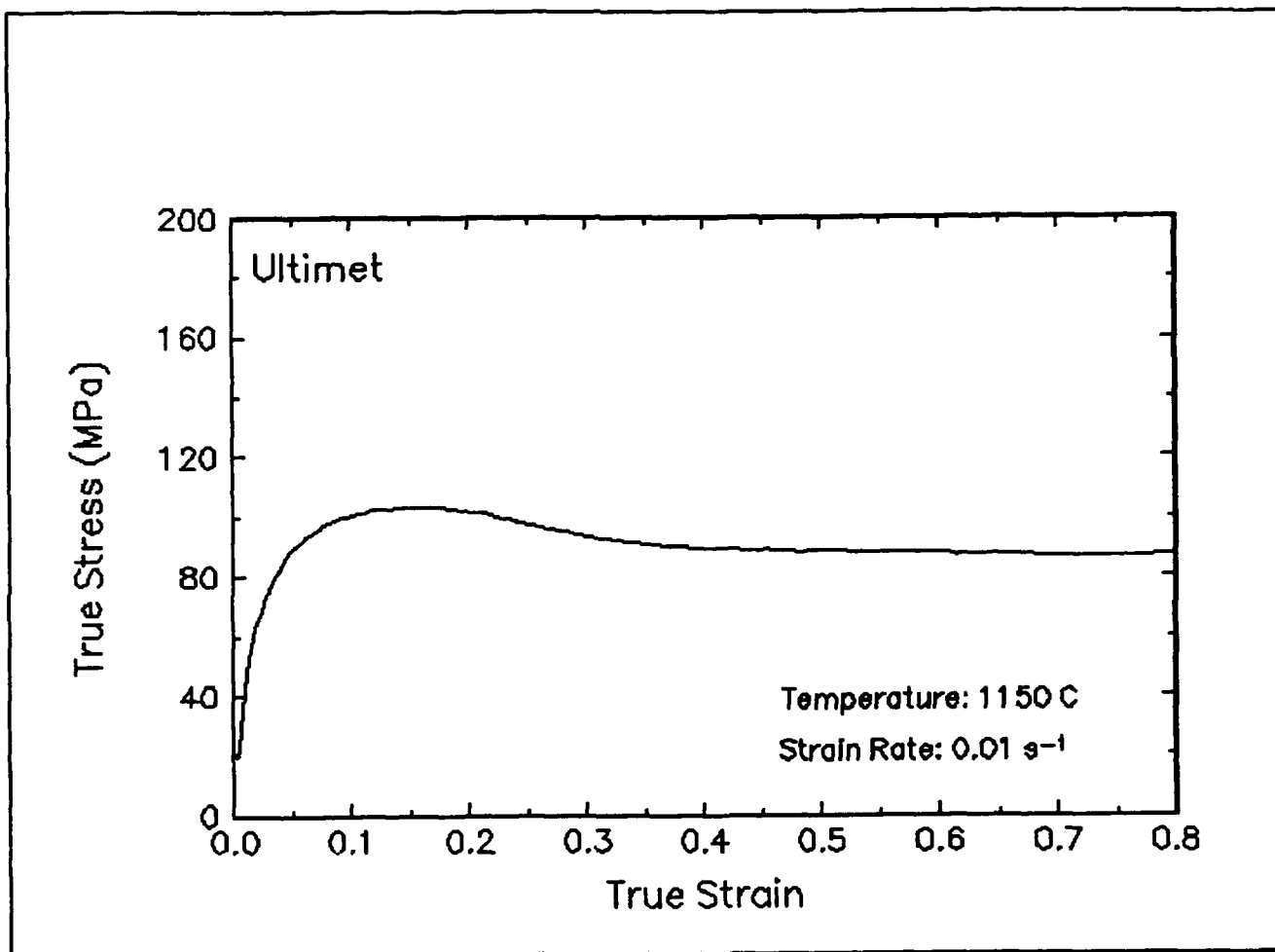


Figure 43. True stress-true strain curve, 1150 C and 0.01 s⁻¹.

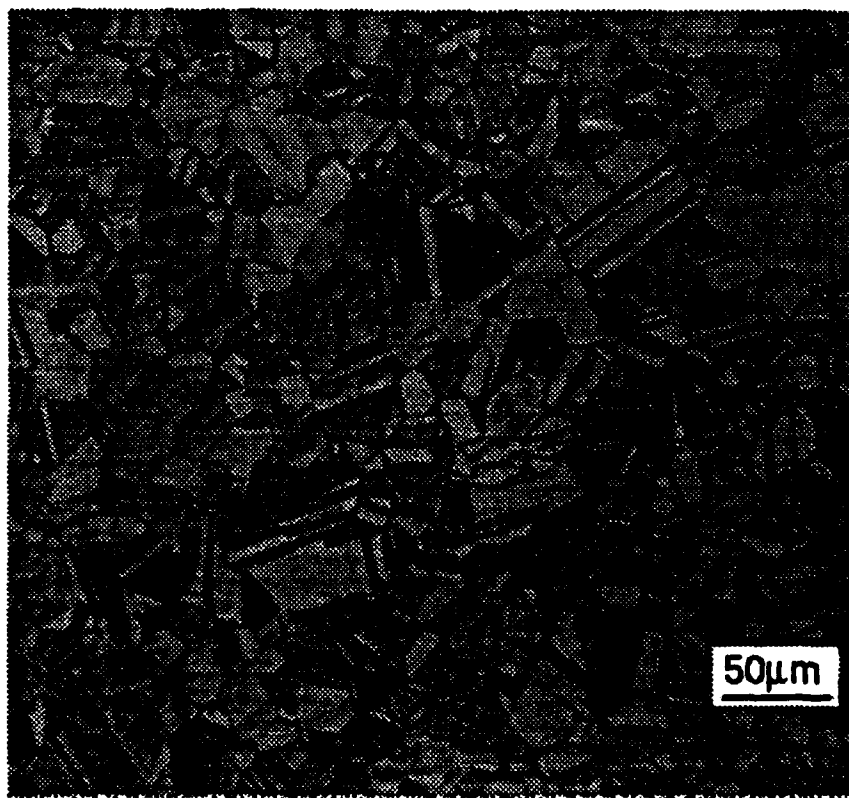
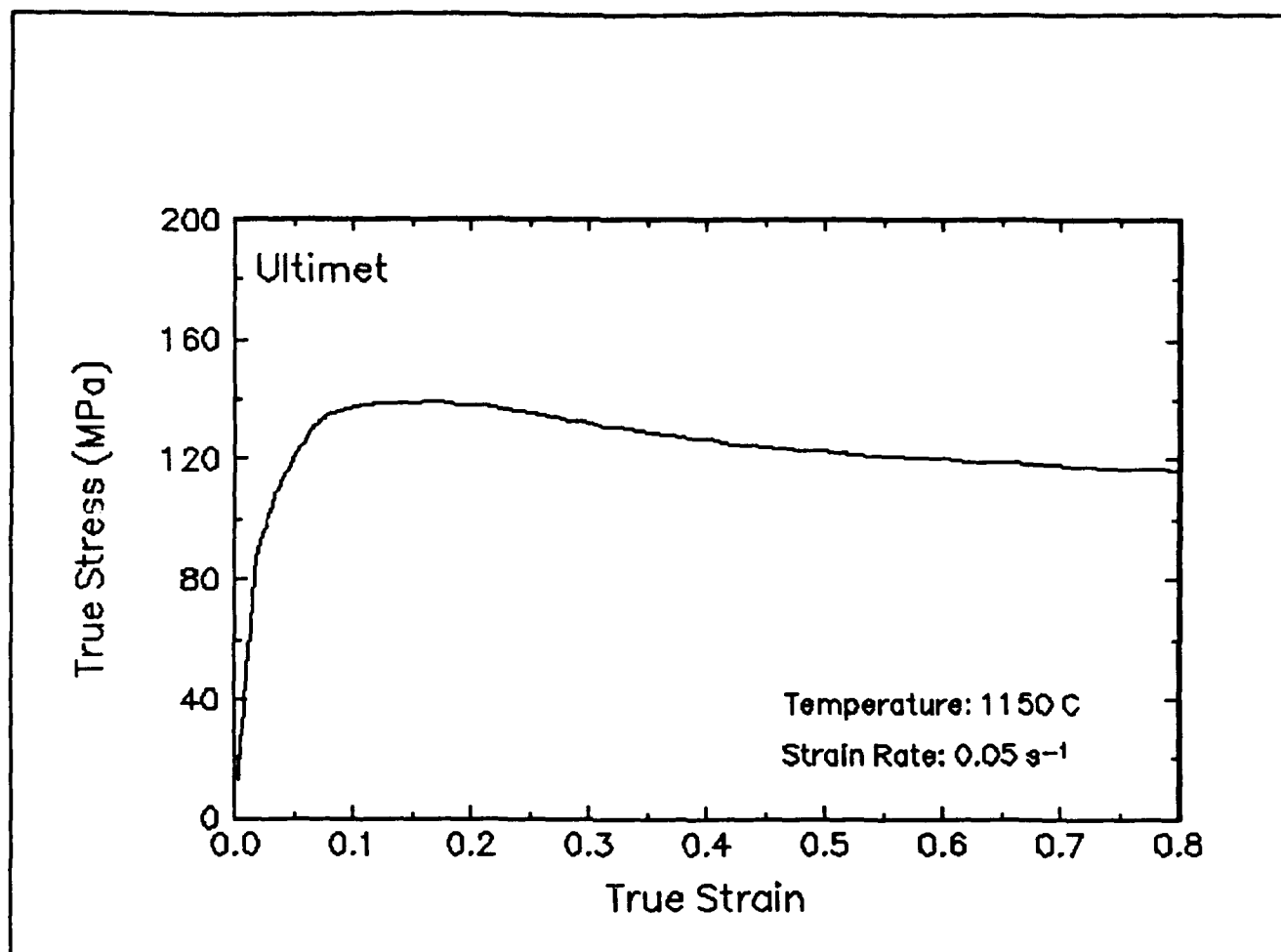


Figure 44. True stress-true strain curve and an optical micrograph from the center of the compressed sample cut through the compression axis, 1150 C and 0.05 s⁻¹.

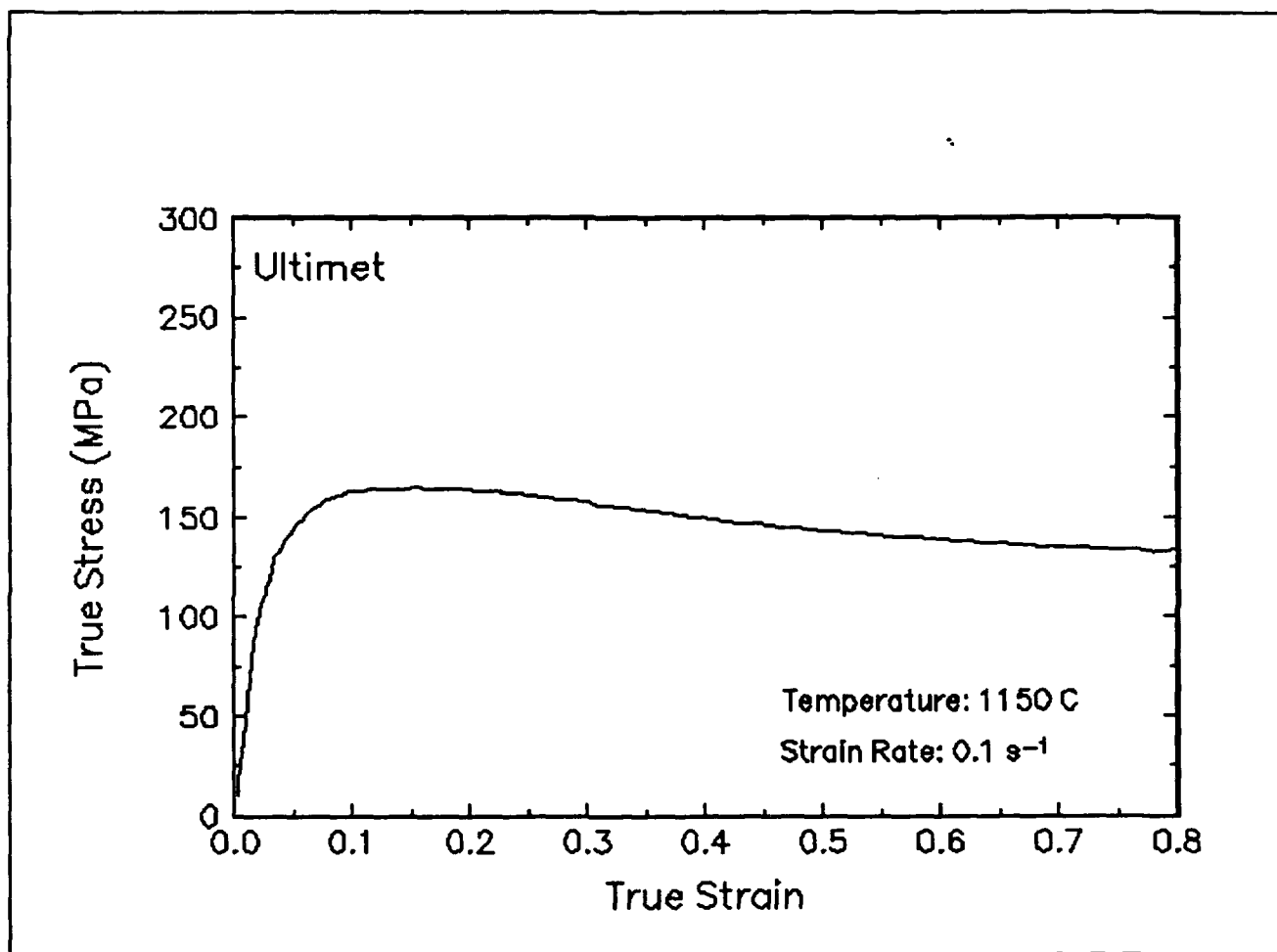


Figure 45. True stress-true strain curve, 1150 C and 0.1 s⁻¹.

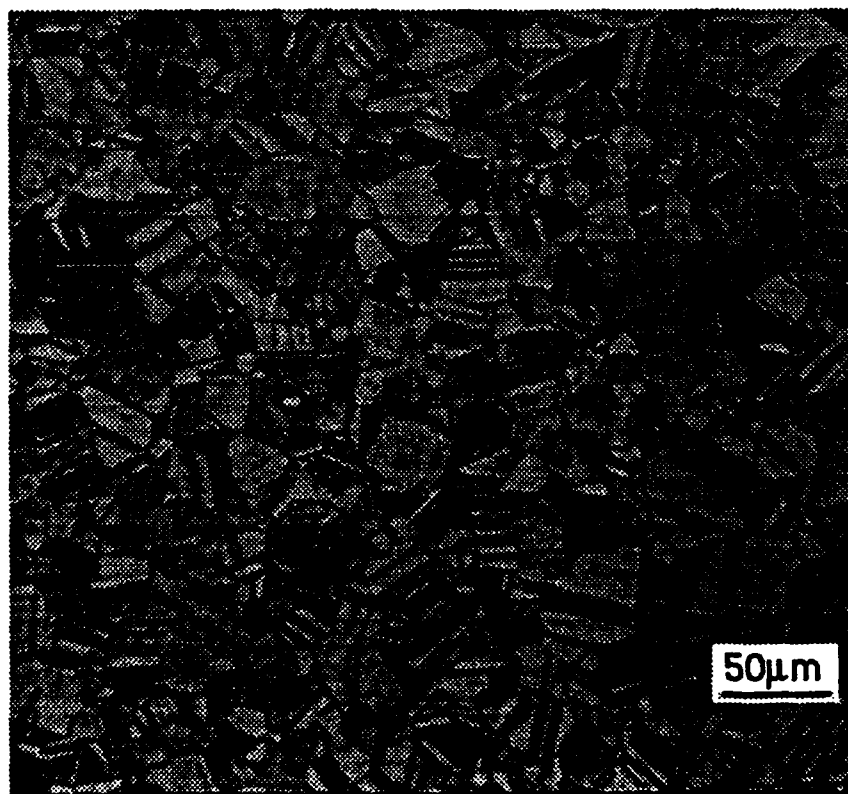
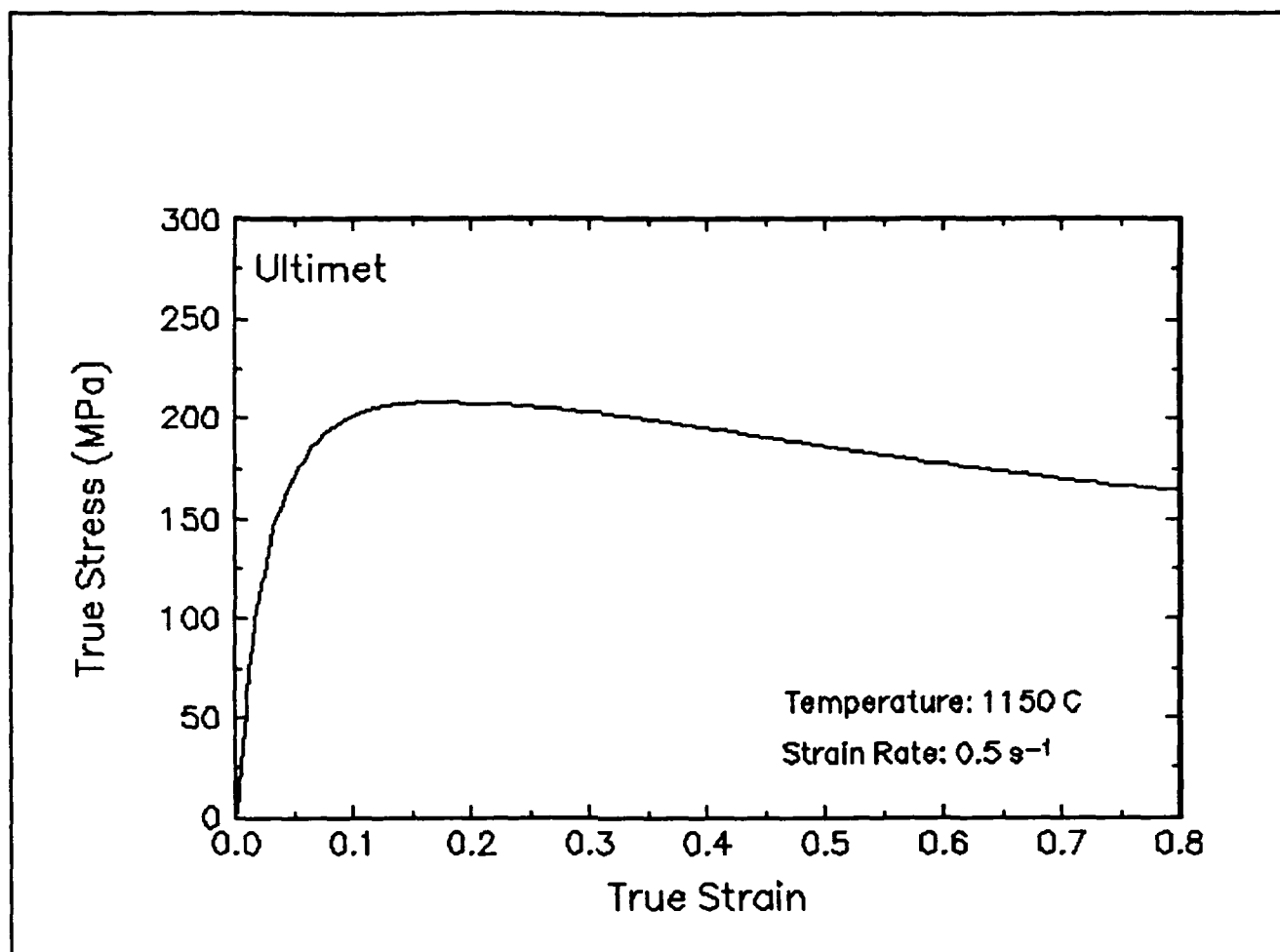


Figure 46. True stress-true strain curve and an optical micrograph from the center of the compressed sample cut through the compression axis, 1150 C and 0.5 s⁻¹.

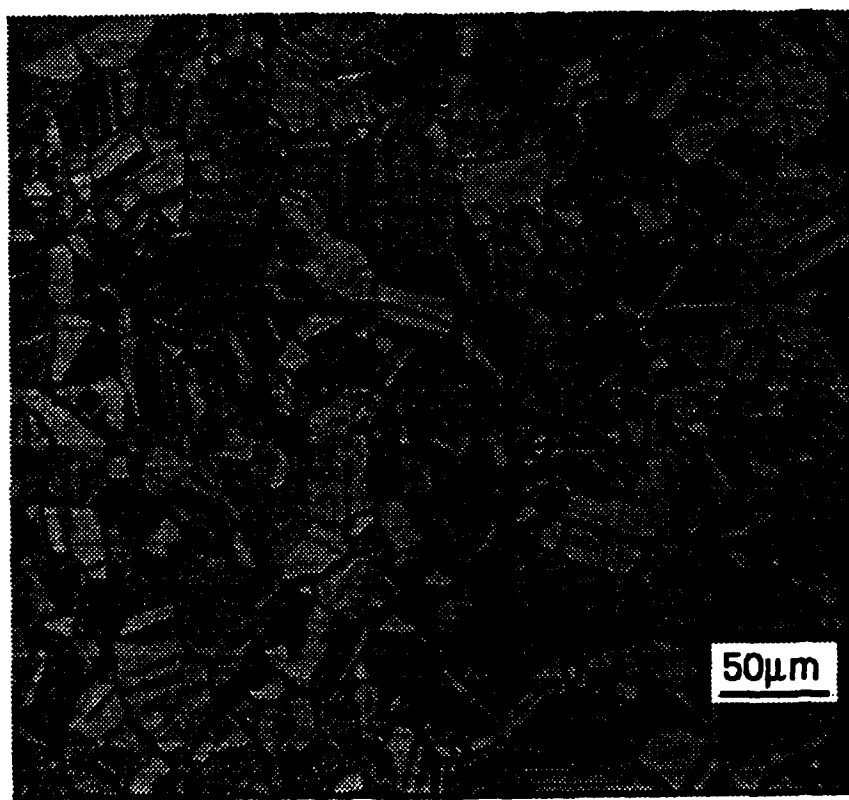
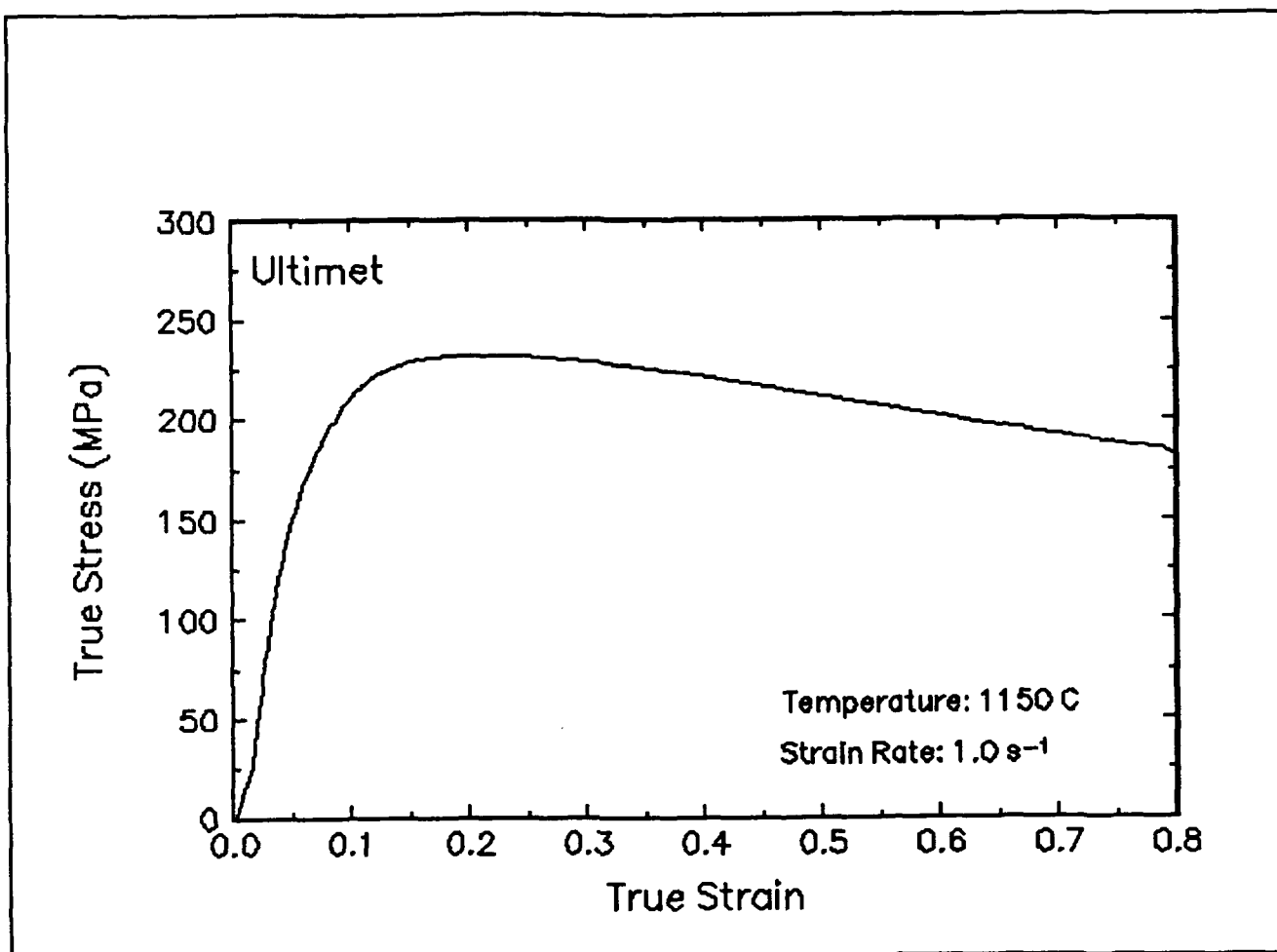


Figure 47. True stress-true strain curve and an optical micrograph from the center of the compressed sample cut through the compression axis, 1150 C and 1 s⁻¹.

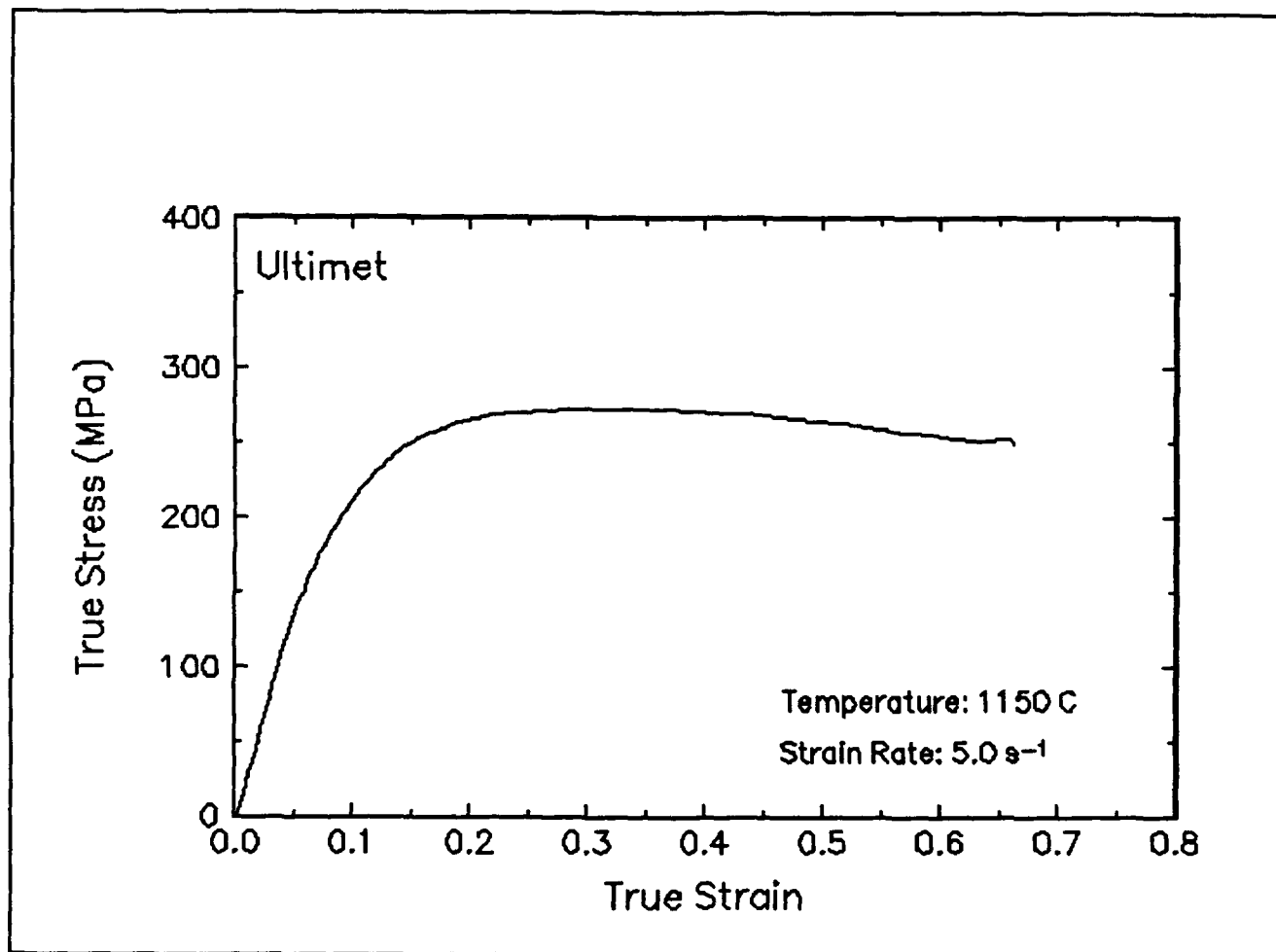


Figure 48. True stress-true strain curve, 1150 C and 5 s⁻¹.

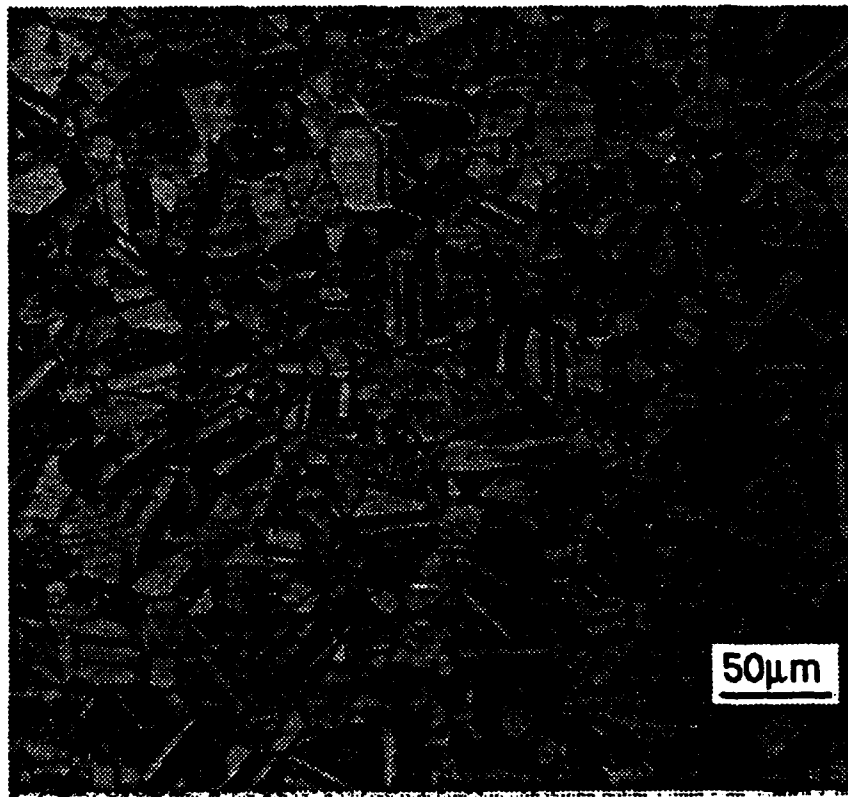
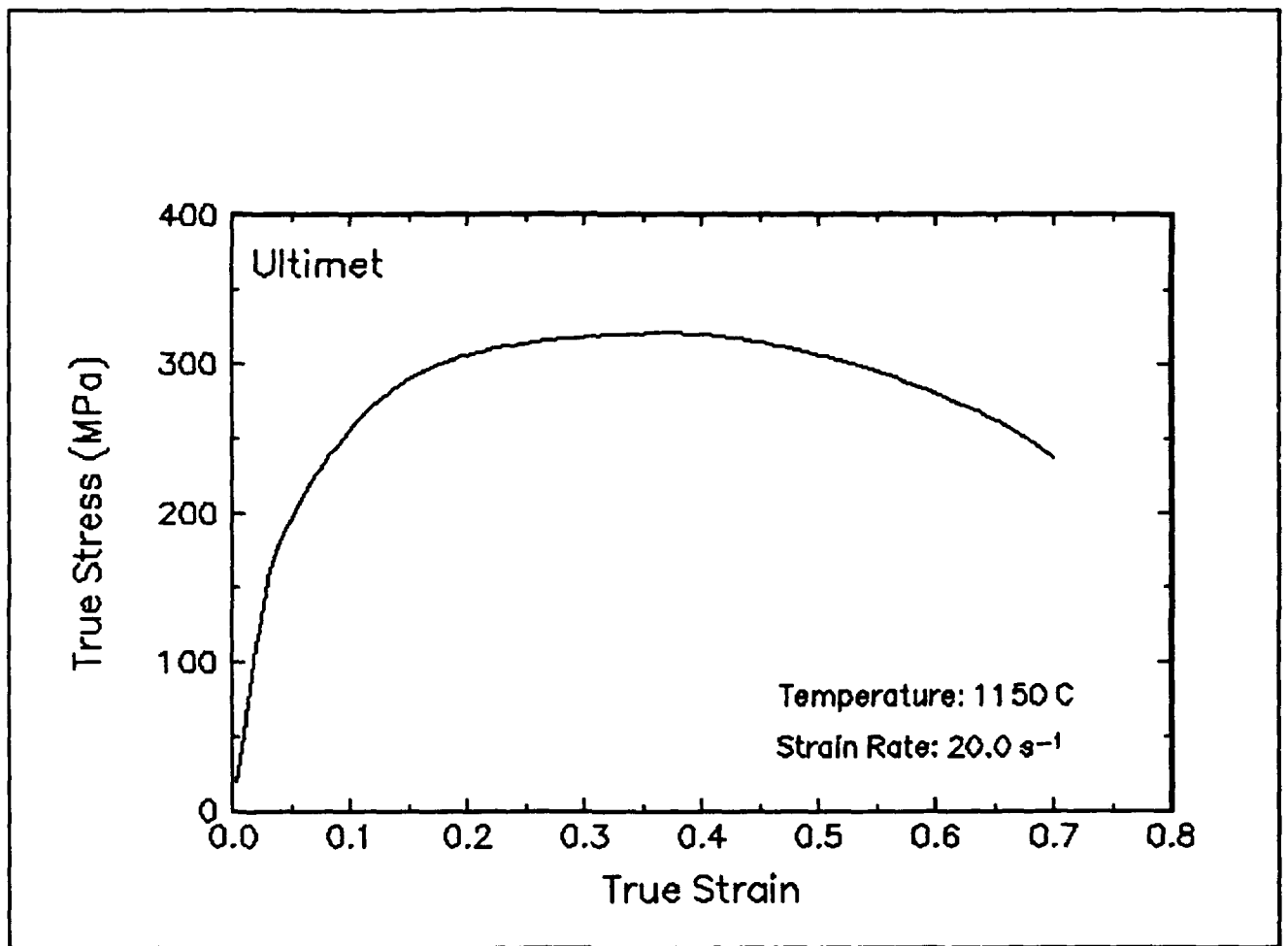


Figure 49. True stress-true strain curve and an optical micrograph from the center of the compressed sample cut through the compression axis, 1150 C and 20 s⁻¹.

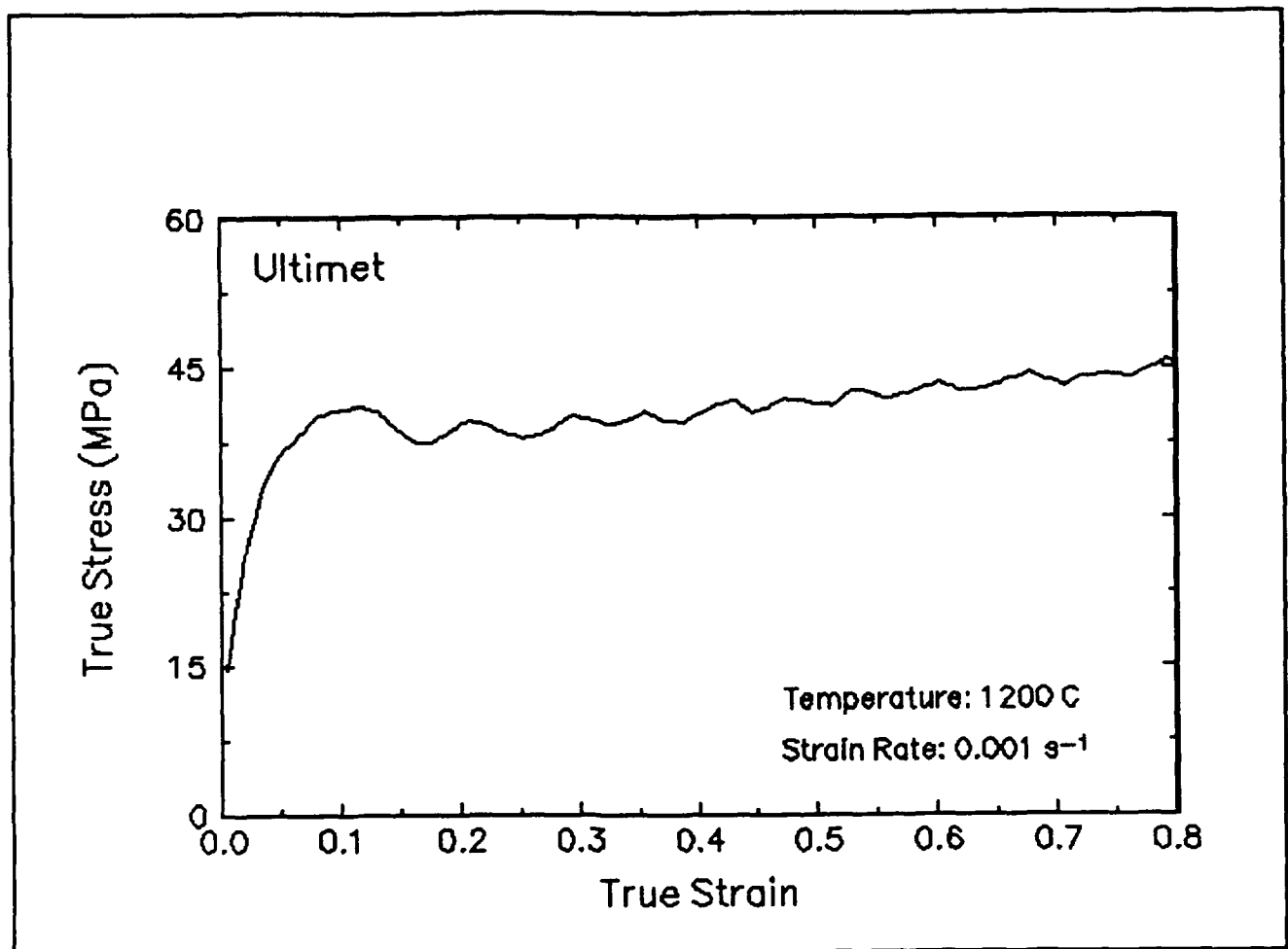


Figure 50. True stress-true strain curve and an optical micrograph from the center of the compressed sample cut through the compression axis, 1200 C and 0.001 s⁻¹.

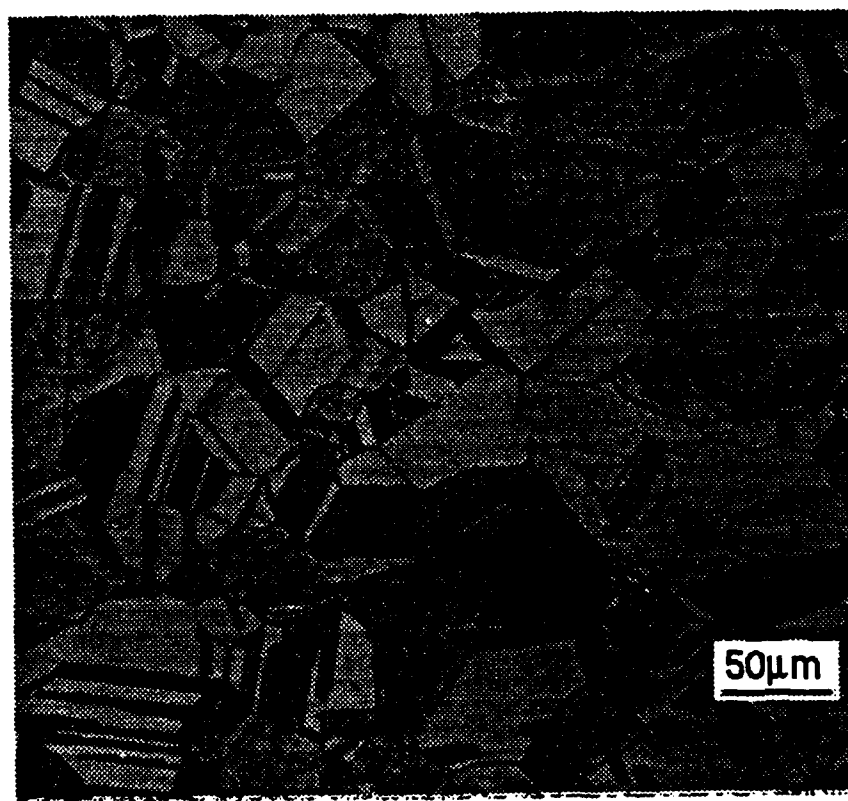
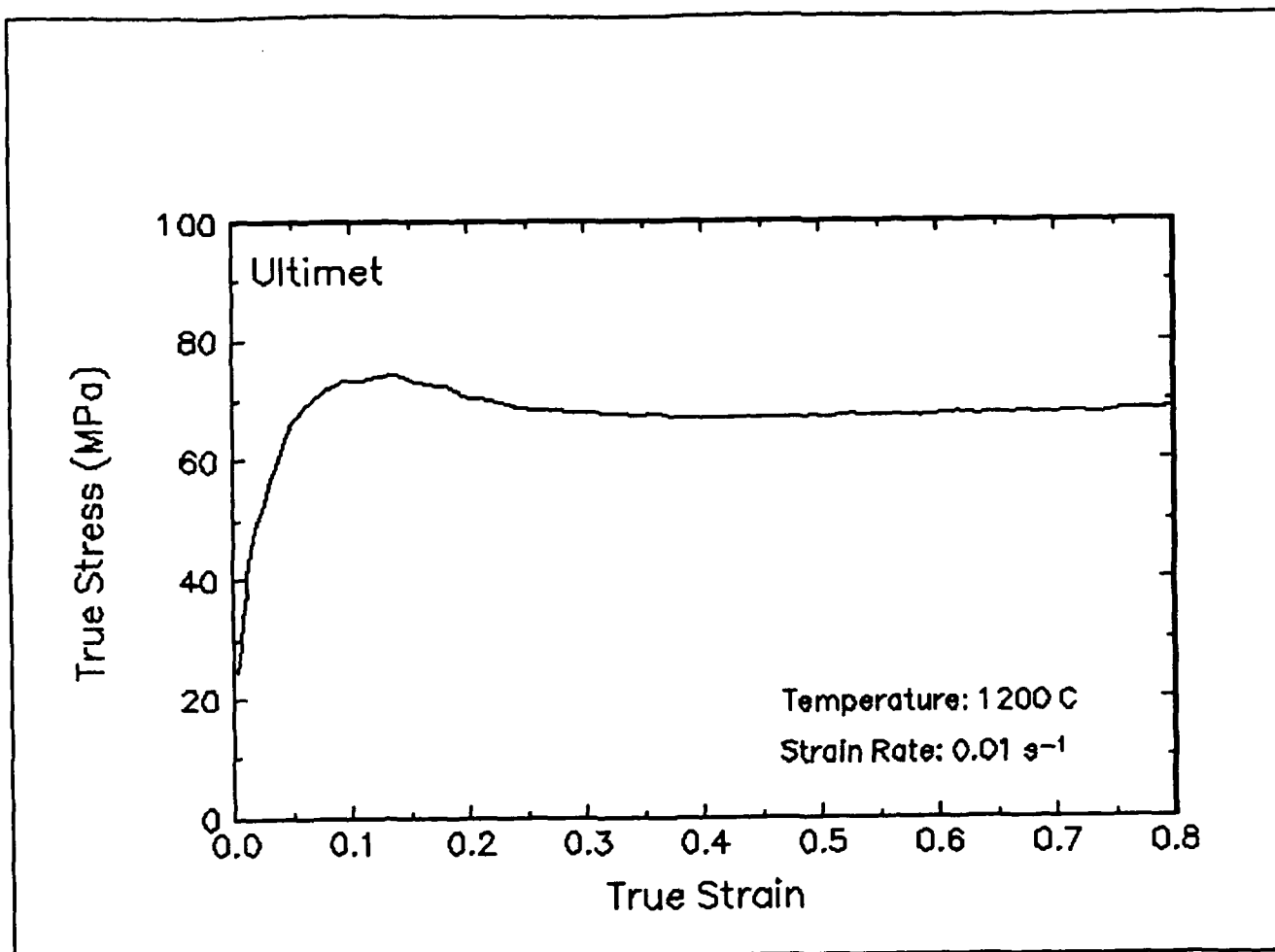


Figure 51. True stress-true strain curve and an optical micrograph from the center of the compressed sample cut through the compression axis, 1200 C and 0.01 s⁻¹.

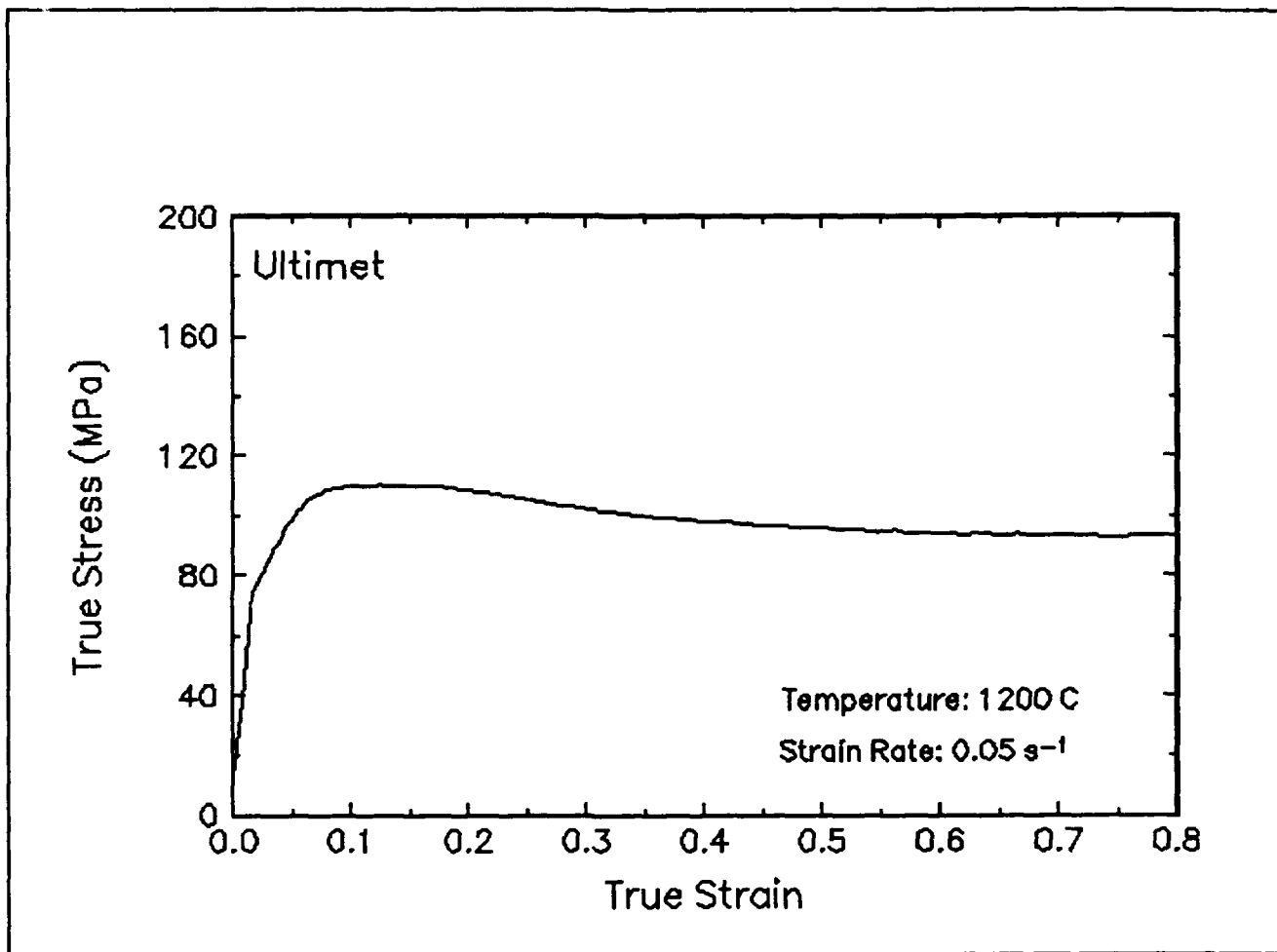


Figure 52. True stress-true strain curve, 1200 C and 0.05 s⁻¹.

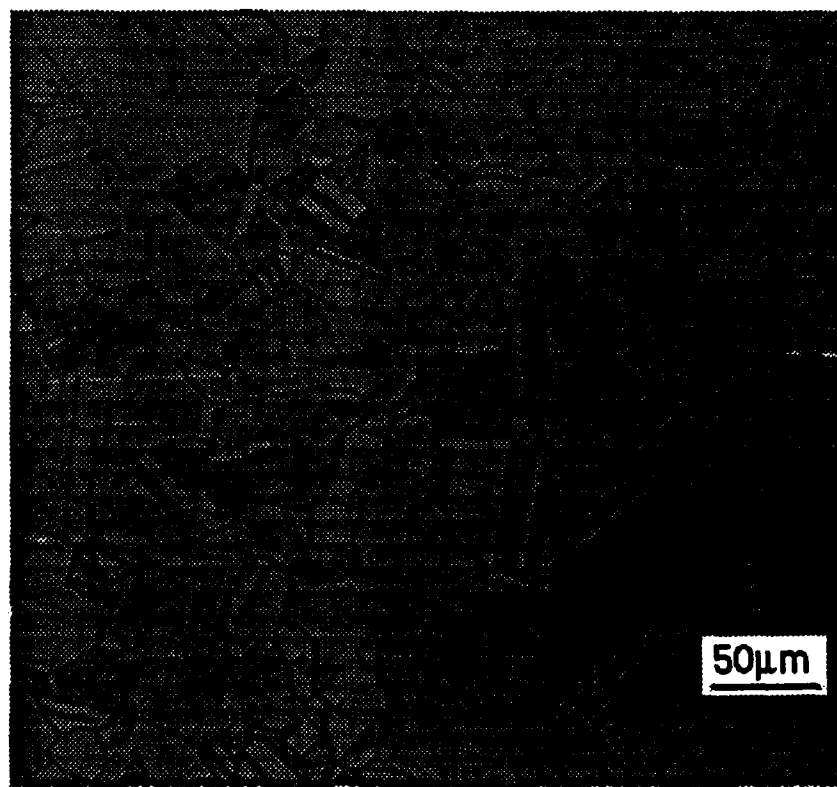
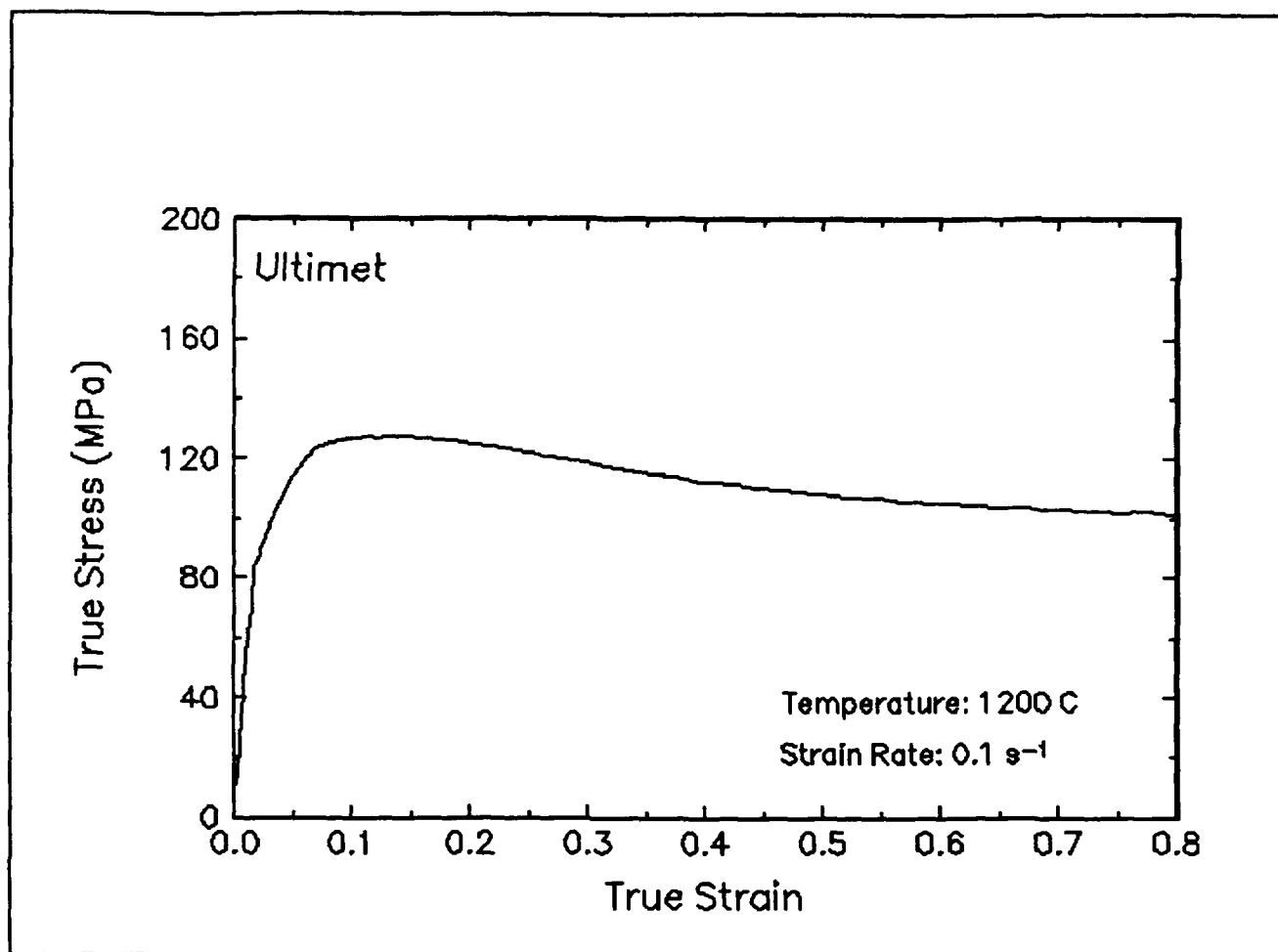


Figure 53. True stress-true strain curve and an optical micrograph from the center of the compressed sample cut through the compression axis, 1200 C and 0.1 s⁻¹.

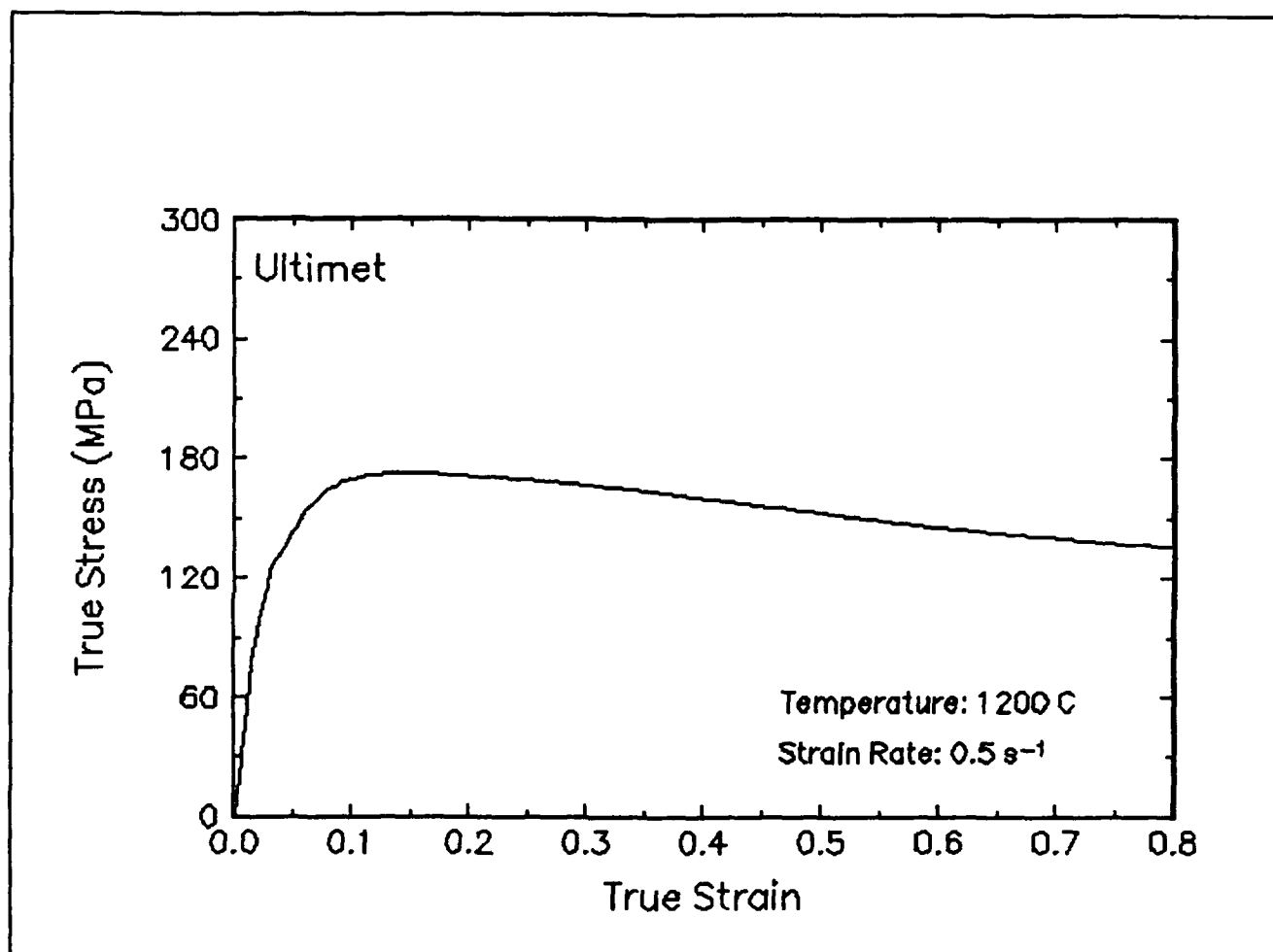


Figure 54. True stress-true strain curve, 1200 C and 0.5 s⁻¹.

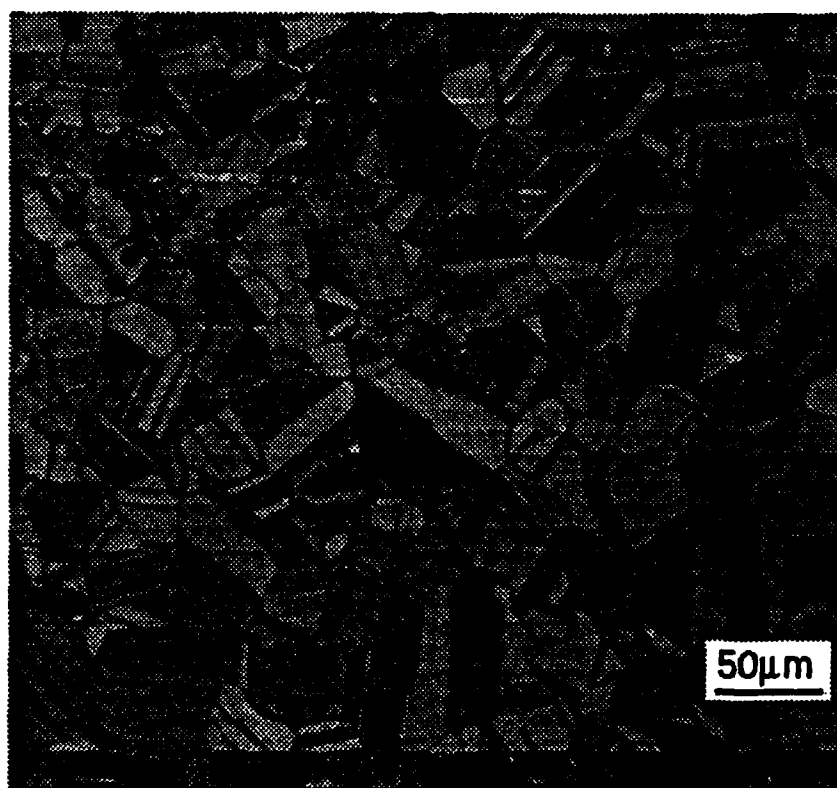
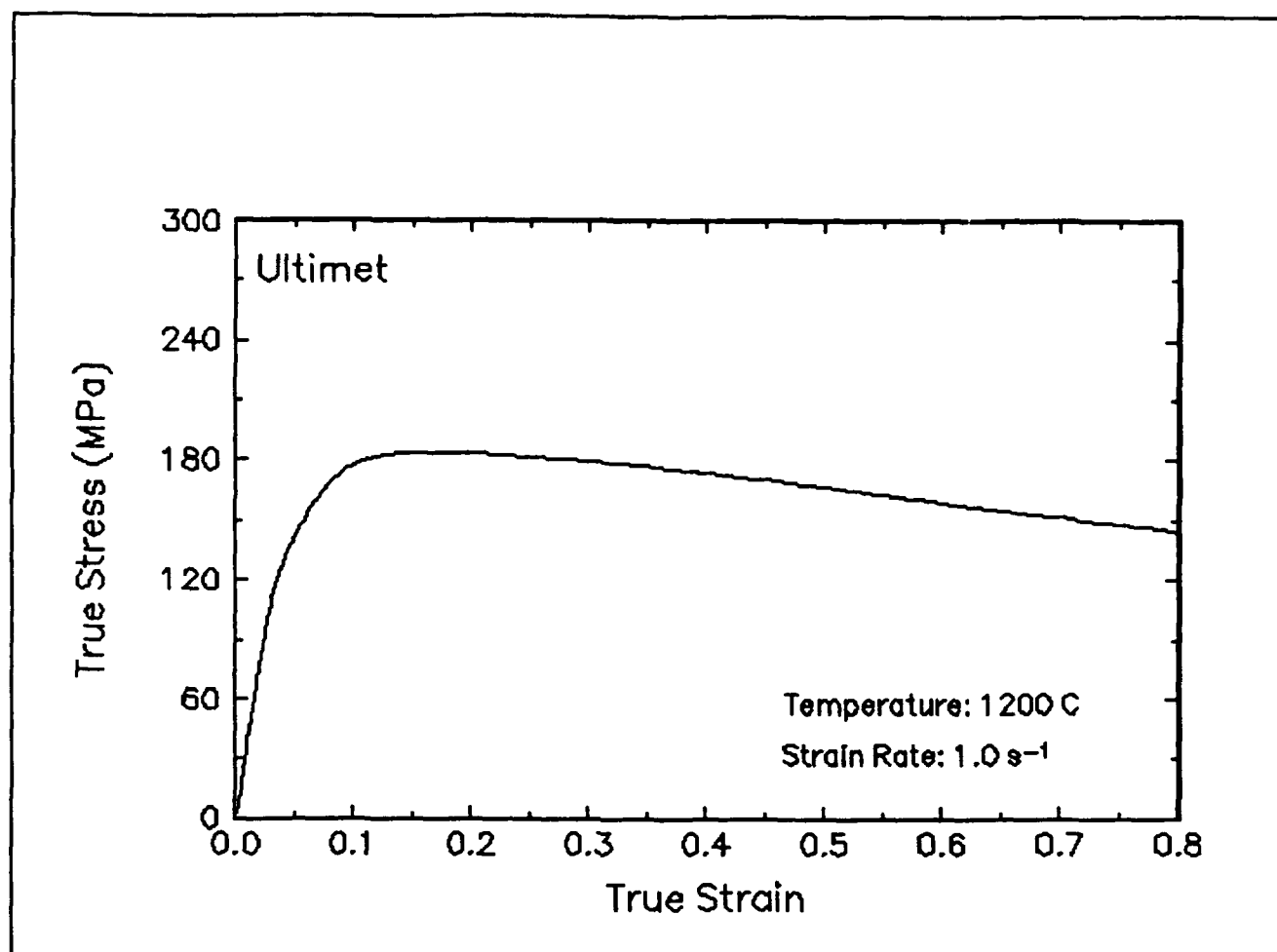


Figure 55. True stress-true strain curve and an optical micrograph from the center of the compressed sample cut through the compression axis, 1200 C and 1 s⁻¹.

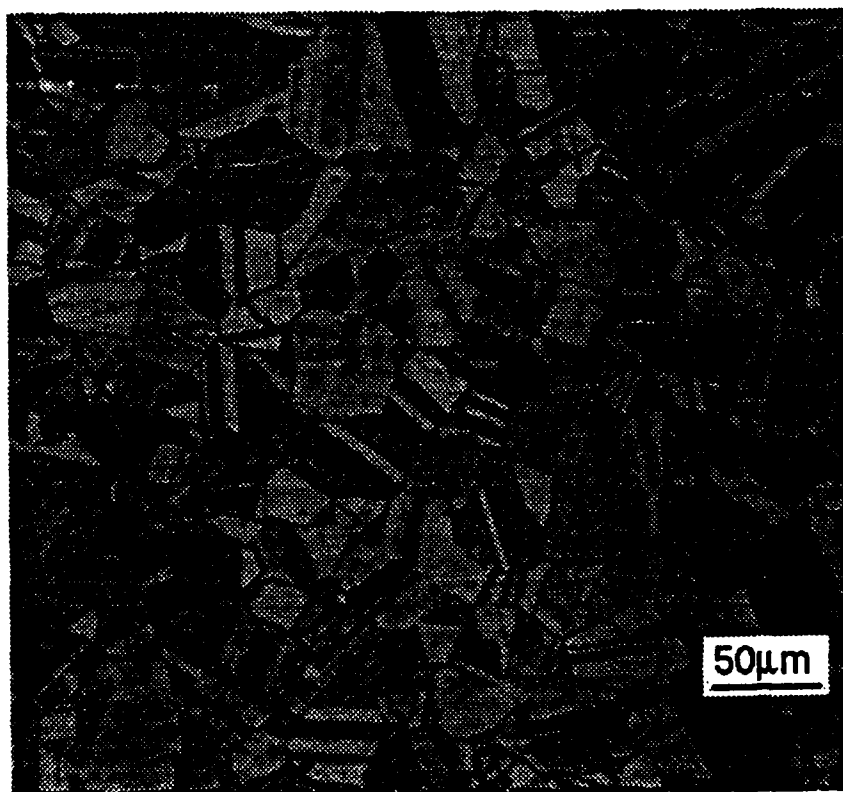
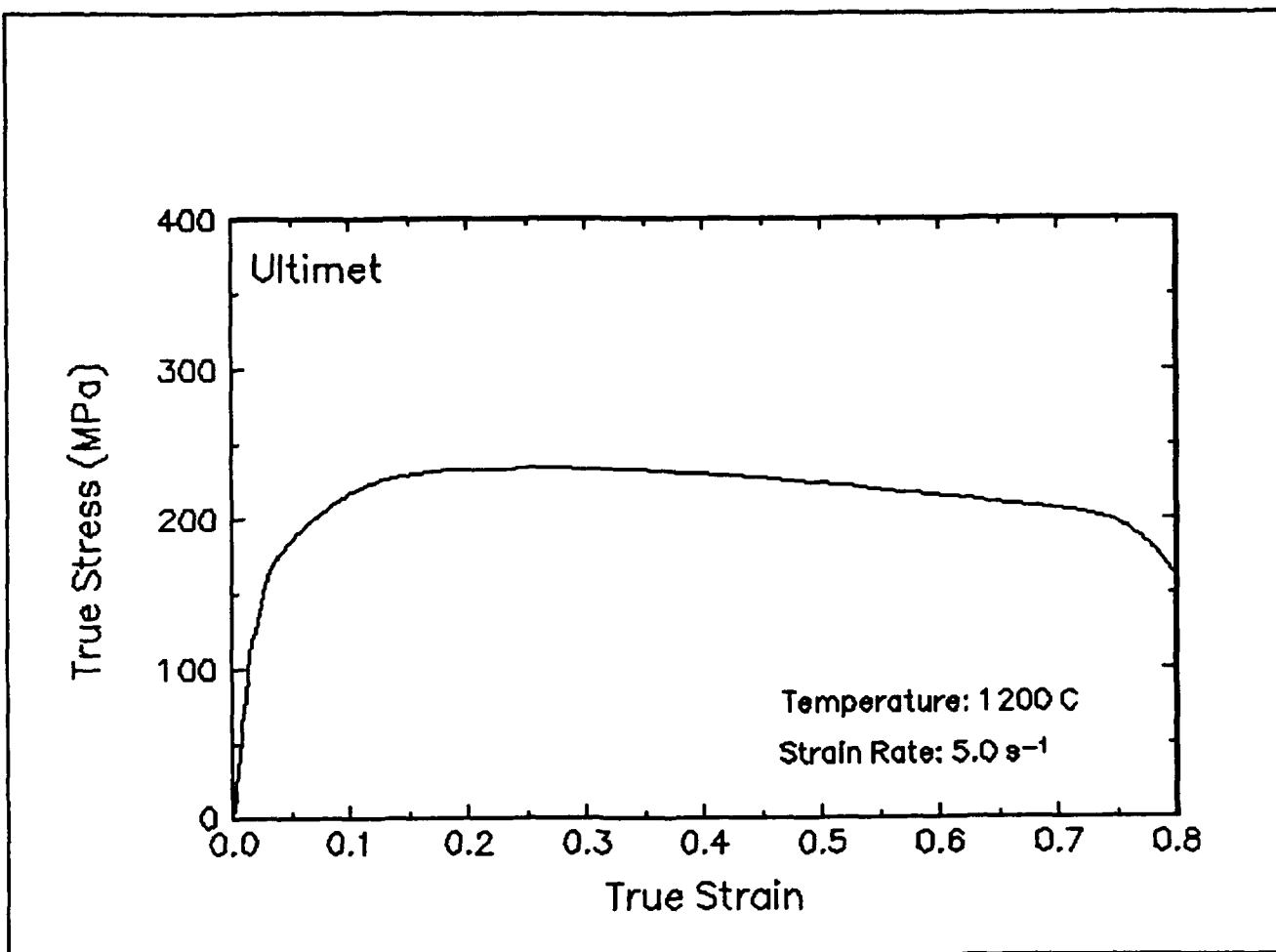


Figure 56. True stress-true strain curve and an optical micrograph from the center of the compressed sample cut through the compression axis, 1200 C and 5 s⁻¹.

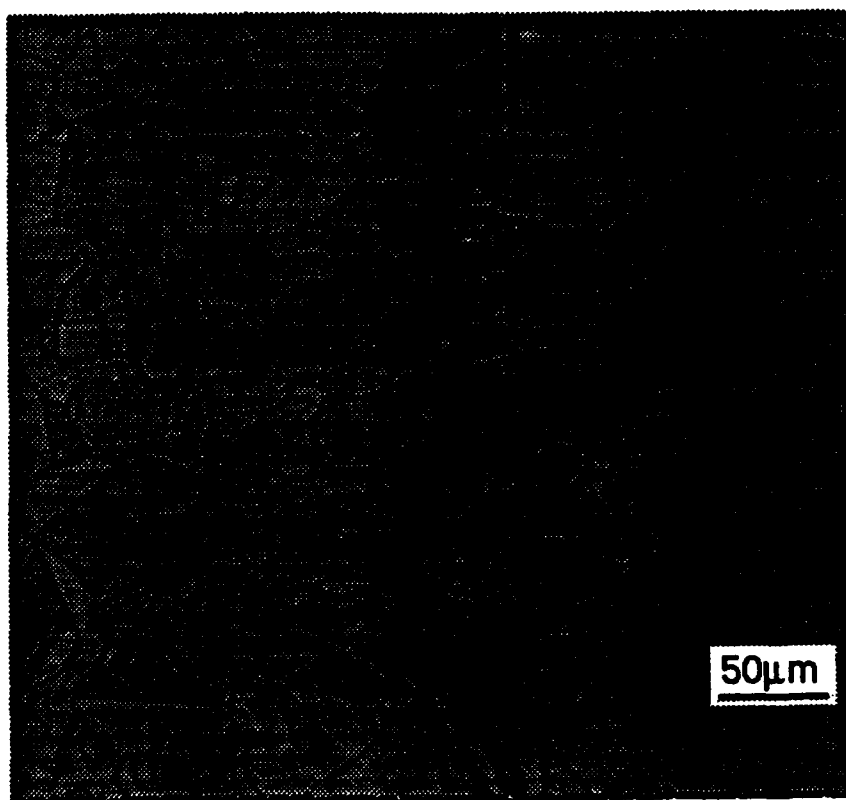
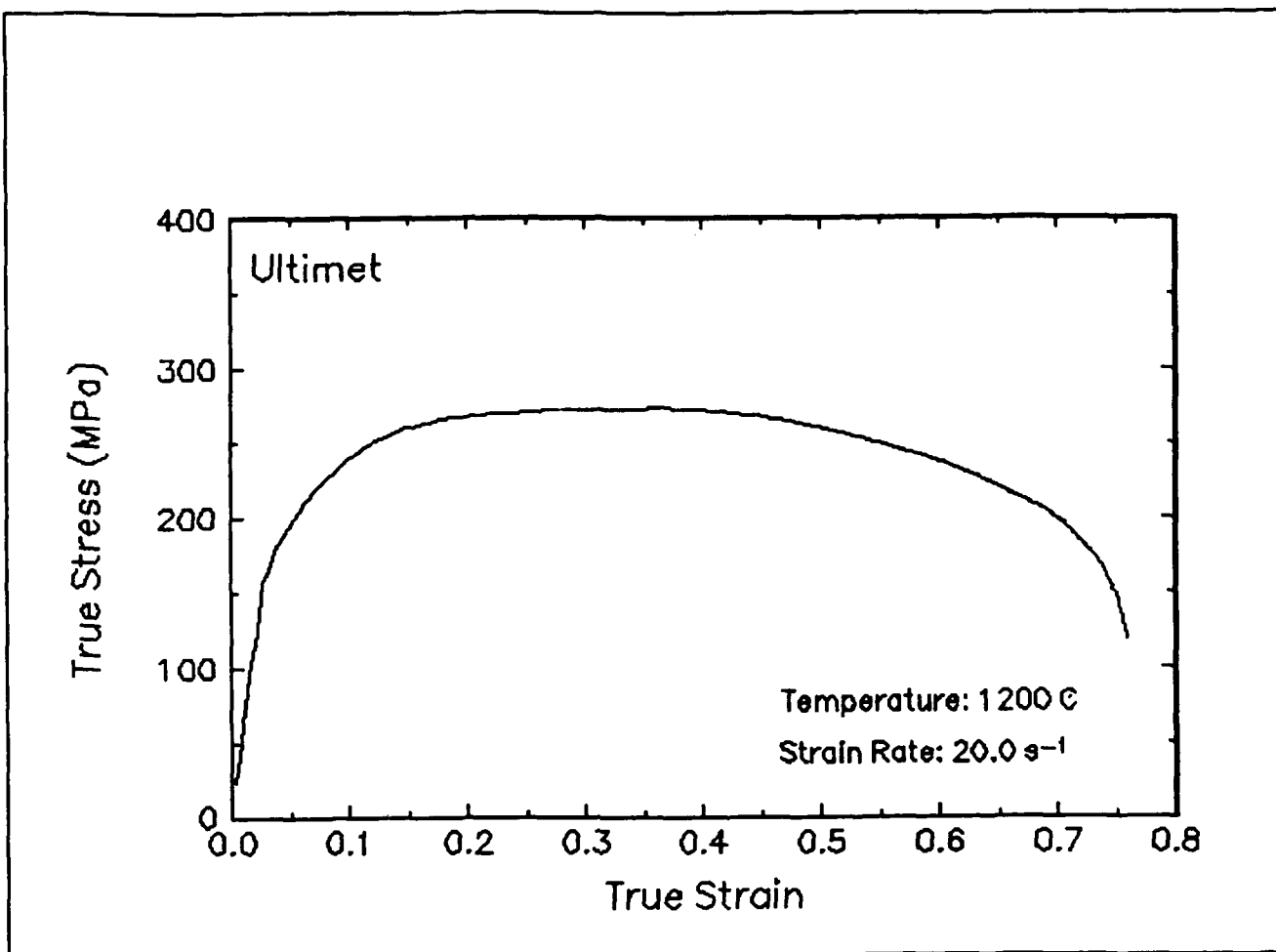


Figure 57. True stress-true strain curve and an optical micrograph from the center of the compressed sample cut through the compression axis, 1200 C and 20 s⁻¹.

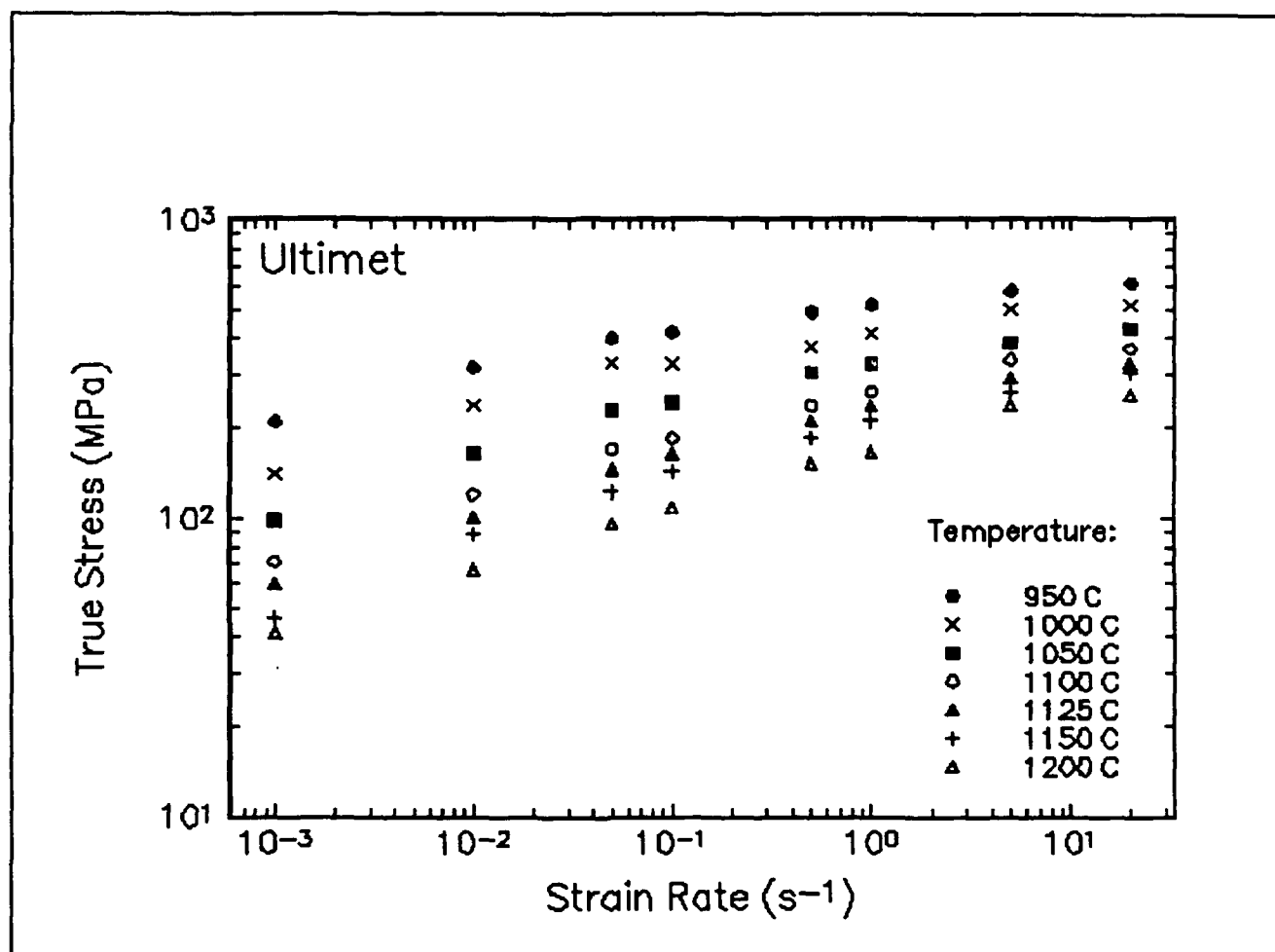


Figure 58. Effect of strain rate on stress in log-log scale at a true strain of 0.5 for Ultimet alloy.

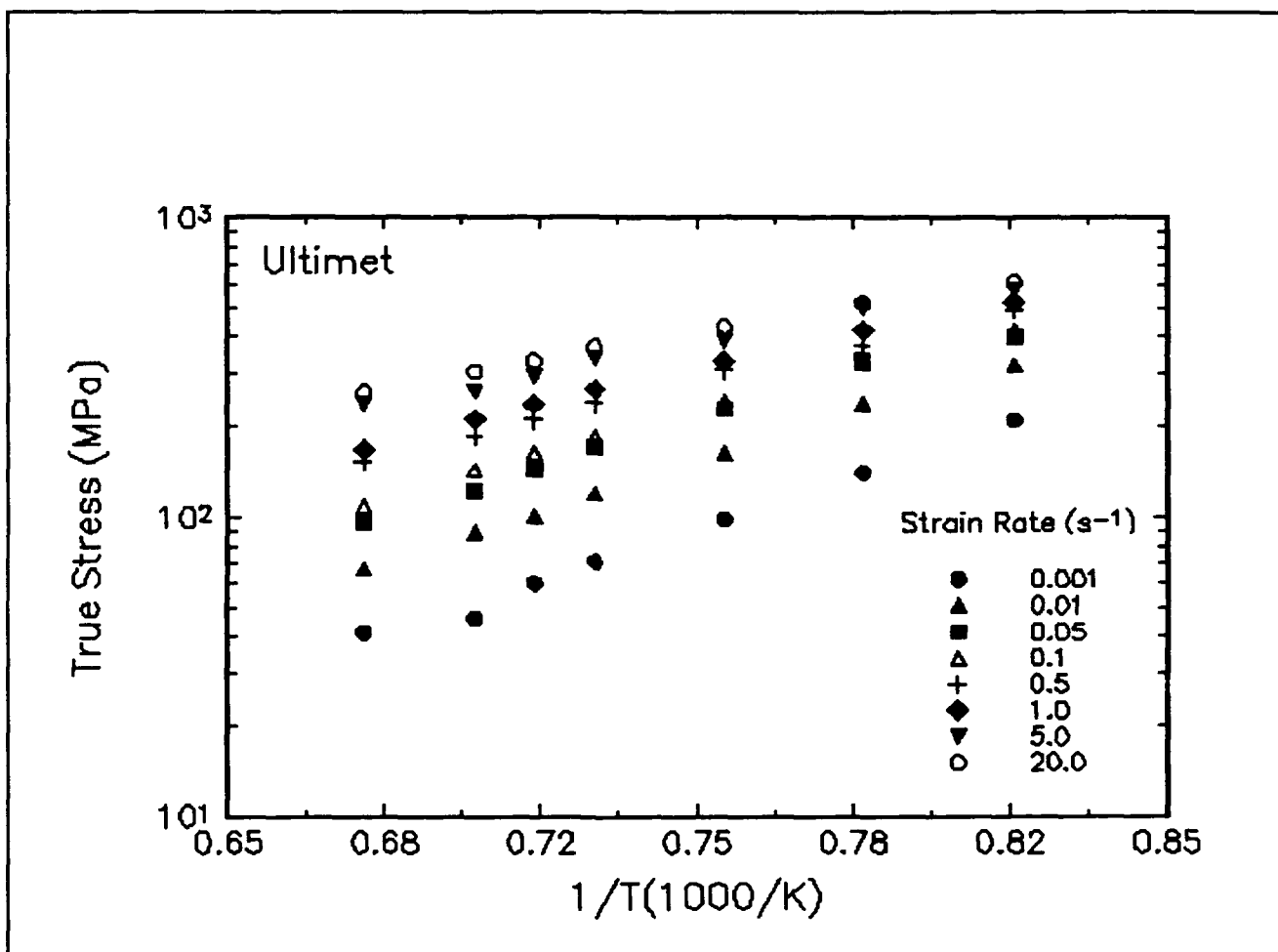


Figure 59. Effect of temperature on stress at a true strain of 0.5 for Ultimet alloy.

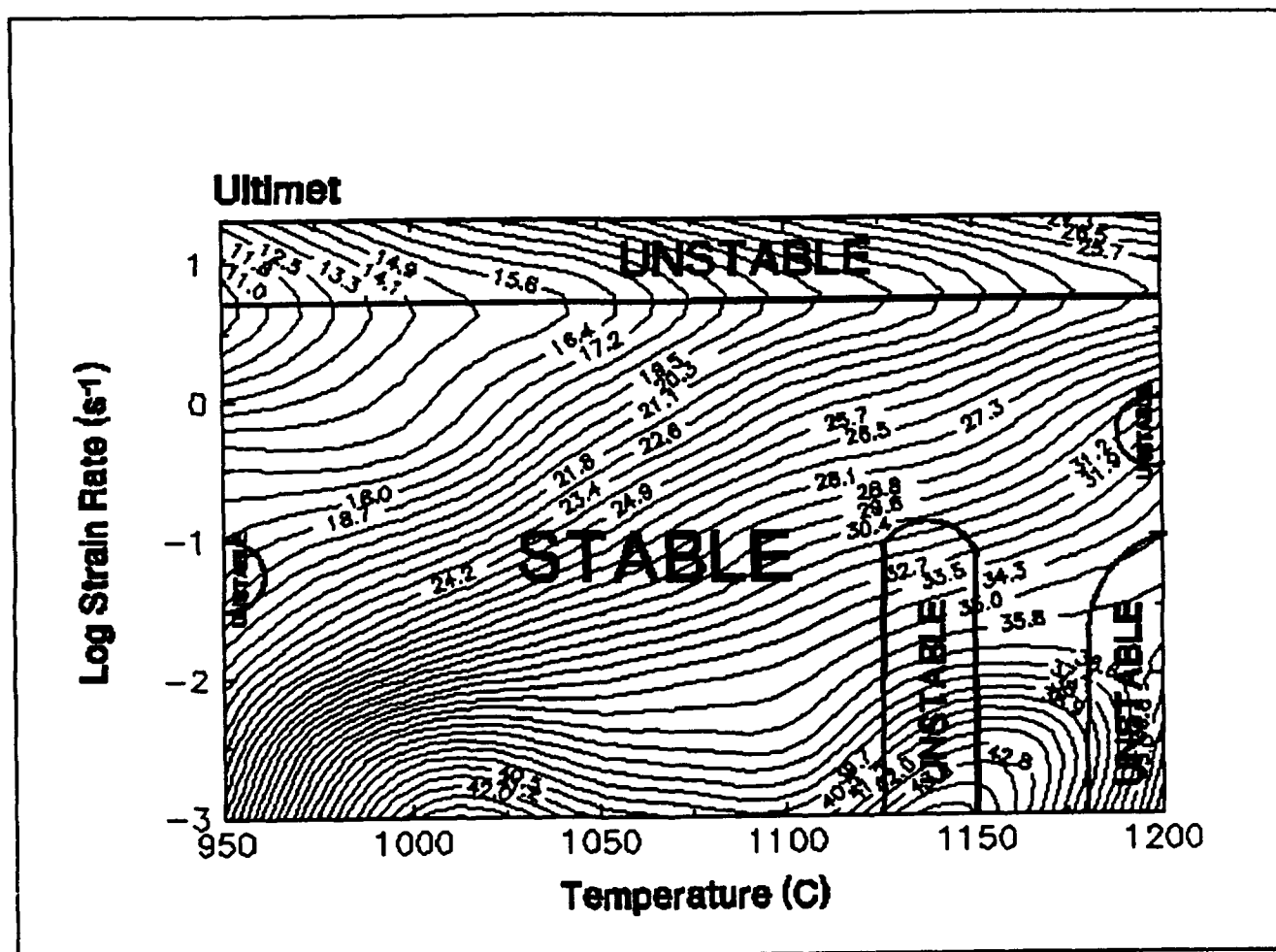


Figure 60. Processing map of Ultimet alloy at a true strain of 0.5.

Summary

Compression tests were performed on a commercially available Ultimet alloy over a wide range of temperatures and strain rates. The experimental conditions in this work were representative of those in metalforming practice. From the true stress-true strain curves, the flow behavior was characterized and a processing map, indicating the optimum processing condition, was generated. This condition is 1012 C and 10^{-3} s^{-1} .

The deformed microstructures were characterized from the quenched specimens by optical microscopy and were presented for selected test conditions together with stress-strain curves.

Implementation of Data Provided by the Atlas of Formability

The *Atlas of Formability* program characterizes the flow behavior of engineering materials in the temperature and strain rate regime commonly used by metalforming industry. The data are valuable in design and problem solving in metalforming processes. Microstructural changes during deformation are also provided in the Bulletin. This information helps the design engineer to select processing parameters leading to the desired microstructure.

The data can also be used to construct processing maps using the dynamic material modeling approach to determine stable and unstable regions in terms of temperature and strain rate. The temperature and strain rate combination at the highest efficiency in the stable region provides the optimum processing condition. In some metalforming processes, such as forging, the strain rate varies within the workpiece. Finite Element Analysis of the process can ensure that strain rates and processing temperatures throughout the workpiece fall into the stable regions in the processing map. Furthermore, FEM analysis based on the data from the *Atlas of Formability* can be coupled with fracture criteria to predict defect formation in metalforming processes.

Concurrent Technologies Corporation uses the *Atlas of Formability* data to design metalforming processes, including dynamic material modeling, FEM analysis, and defect prediction. CTC can apply its expertise to develop and optimize metalforming processes. For more information, please contact Dr. Prabir K. Chaudhury, Manager, Forming Department, by calling (814) 269-2594.